

LATE CENOZOIC BASIN EVOLUTION OF THE WESTERN CANADIAN ARCTIC
ARCHIPELAGO: THE BEAUFORT FORMATION AND IPERK SEQUENCE

by

Sydney A. Stashin

Submitted in partial fulfilment of the requirements
for the degree of Master of Science

at

Dalhousie University
Halifax, Nova Scotia
March 2021

© Copyright by Sydney A. Stashin, 2021

TABLE OF CONTENTS

<i>LIST OF TABLES</i>	<i>v</i>
<i>LIST OF FIGURES</i>	<i>vi</i>
<i>ABSTRACT</i>	<i>x</i>
<i>LIST OF ABBREVIATIONS AND SYMBOLS USED</i>	<i>xi</i>
<i>ACKNOWLEDGEMENTS</i>	<i>xii</i>
<i>Chapter 1. Introduction</i>	<i>1</i>
1.1 Previous Beaufort Formation and Equivalent Studies.....	4
1.2 Thesis Questions & Objectives	6
1.3 Result Highlights and Significance	7
1.4 Thesis Design	8
<i>Chapter 2. Beaufort Formation Chronostratigraphy, Prince Patrick Island, Northwest Territories</i>	<i>10</i>
2.1 Abstract.....	10
2.2 Introduction	11
2.3 Background.....	12
2.3.1 Previous Chronology	15
2.4 Methods	15
2.4.1 Interpretation of aerial photographs and remotely sensed images prior to field work.....	18
2.4.2 Sedimentology field methods	18
2.4.3 Geochronology field methods	19
2.4.4 Geochronology Lab Methods	24
2.4.5 Simple Burial and Isochron Dating Methodology.....	27
2.5 Results & Interpretation	29
2.5.1 Improvements to experimental design.....	29
2.5.2 Stratigraphy and Sedimentology	30
2.5.3 Simple Burial and Isochron Ages.....	37
2.6 Discussion.....	44
2.6.1 Sedimentology and Stratigraphy of the Beaufort Formation on Prince Patrick Island	47
2.6.2 What were the causes of deposition of the Beaufort Formation?.....	48
2.6.3 The Pliocene as an analogue for future warming?	50

2.6.4	Uncertainty in Isochron Age	51
2.7	Conclusions	51
2.8	Acknowledgments	52
<i>Chapter 3.</i>	<i>The Late Cenozoic Evolution of the Banks–Beaufort Basin, Arctic Canada.....</i>	<i>53</i>
3.1	Abstract.....	53
3.2	Introduction	54
3.3	Background.....	57
3.3.1	Tectonic History	59
3.3.2	Current stratigraphic framework	61
3.3.3	The Beaufort Formation	63
3.3.4	Relationship between the Iperk Sequence and Beaufort Formation	66
3.3.5	Post-Messinian Climate.....	67
3.3.6	Sedimentation and erosion rates.....	68
3.3.7	Glacial History and Trough Formation	68
3.4	Methods	69
3.5	Results and Interpretations	71
3.5.1	Seismic facies	71
3.5.2	Faulting.....	75
3.5.3	Interpretation of Late Cenozoic seismostratigraphy.....	79
3.5.4	Correlations with the Slope and Canada Basin	90
3.5.5	A late-stage inner shelf terrace: a possible expression of paleo-coastal systems.....	91
3.6	Discussion.....	94
3.6.1	Comparison of Beaufort–Mackenzie and Banks–Beaufort Basins Iperk Sequences	95
3.6.2	Late Cenozoic Chronostratigraphy in the Banks–Beaufort Basin.....	96
3.6.3	Sedimentation rate estimates	105
3.6.4	Pliocene Shorelines	107
3.6.5	Timing of Inter-Island Channels/Trough Formation	107
3.7	Conclusions	108
3.8	Acknowledgements	110
<i>Chapter 4.</i>	<i>Implications and Conclusions.....</i>	<i>111</i>
4.2	Implications and Future Work.....	113
<i>References.....</i>		<i>117</i>
<i>Appendix A.</i>	<i>Supplementary File to Chapter 2.....</i>	<i>131</i>

A.1 Isochron Samples.....	131
A2 Burial Age Dating Plots with Probability Distributions.....	133
Simple Burial Plot Sample PPI-17-103-006.....	133
Simple Burial Plot Sample PPI-17-105-017.....	133
<i>Appendix B. Data Tables and Chemical Worksheets.....</i>	<i>134</i>
B.1 AMS- Standard Corrected Output.....	135
B.2 ICP Results and Data Reduction.....	138
B.3 Chemical Worksheets for TCN Data.....	144
<i>Appendix C. Field Photos.....</i>	<i>147</i>

LIST OF TABLES

Table 2.1. List and description of samples collected during the 2017 field expedition to Prince Patrick Island.....	21
Table 2.2. TCN measurements for cobble and sand samples from Prince Patrick Island, NWT.....	38
Table 2.3. Simple burial ages (Ma) for the sand samples.	39
Table 2.4. Multiple isochron burial dating options for cobble and sand samples from Prince Patrick Island, NWT.....	43
Table 3.1. Illustrations of multiple seismic facies identified from 2D seismic profiles offshore Banks Island, NWT.....	74
Table 3.2. Physical attributes of the 8 offshore units interpreted within the extents of the ION seismic coverage in the Banks–Beaufort Basin.....	82
Table 3.3. Sedimentation rates calculated from the Iperk Sequence equivalent in the Banks–Beaufort Basin. Dual scenarios are presented here due to chronological uncertainty.....	106
Table B.1. Clast lithology of 97 clasts sampled within the gravel facies section above unconformity, section D8	134
Table B.2. Average ²⁷ Al current per sample during each run	134
Table B.3. Average ⁹ Be current per sample during each run	135
Table B.4. ²⁶ Al AMS data.	135
Table B.5. ¹⁰ Be AMS results.	136
Table B.6. ICP Results	138
Table B.7. ²⁶ Al data reduction.	141
Table B.8. ¹⁰ Be data reduction.....	143

LIST OF FIGURES

Figure 1.1. Map of the Canadian Arctic Archipelago (CAA) with locations of previous BFm and BFm equivalent studies.....	1
Figure 1.2. Geological time scale, Pacific $\delta_{18}\text{O}_{\text{Benthic}}$ and sea level curves through time, modified from Miller et al. (2020).	2
Figure 2.1. Map of the Canadian Arctic Archipelago with the locations of previous BFm and equivalent studies (sensu stricto and sensu lato), modified from Gosse et al. (2017).....	13
Figure 2.2. Landsat image of Prince Patrick Island, displaying previously visited field sites.....	17
Figure 2.3. Field photo of section D8, with locations and depths of samples indicated.	20
Figure 2.4. Photo of a section of D8 at 23.5 m depth (line drawn on Figure 2.3), showing cross stratified sand and a bed where multiple cobble samples were discovered.	20
Figure 2.5. A: Experimental elution curves for a range of elements (Be, Al, Ca, Fe, Mg, Mn, Na, Ti, and K), eluted within a 5 ml column	30
Figure 2.6. Two stratigraphic columns (left D8 and right S1) recorded from BFm exposures on Prince Patrick Island.	31
Figure 2.7. Distinctly different gravel facies observed above unconformity at 23 m up-section D8.	34
Figure 2.8. Potential sand wedge pseudomorphs observed at the top of section S1.	35
Figure 2.9. Simple burial plot of $^{26}\text{Al}/^{10}\text{Be}$ (atoms atoms ⁻¹) versus normalized ^{10}Be concentration (atoms g ⁻¹).....	39
Figure 2.10. Isochron burial dating plots for cobble and sand samples from Prince Patrick Island, from multiple sample combination options (Table 2.4).	44
Figure 3.1: A: GEBCO sea floor bathymetry map of the Canadian Beaufort Sea and surrounding features (400 m contours) and land topography (grey topographic shading).....	56
Figure 3.2. Paleoenvironmental reconstruction of Neogene Arctic Canada	58
Figure 3.3. Summary of four well logs of wells onshore Banks Island (locations shown in Figure 3.1B) (Miall 1979) from north to south.	59
Figure 3.4. M'Clure Strait and Amundsen Gulf, with the light blue shading showing zones where potential fault scarps would occur if these channels were fault bounded.....	78
Figure 3.5. Uninterpreted and interpreted 2D seismic profile data from offshore Banks Island (courtesy of ION) (line locations shown on Figure 3.1B).	81
Figure 3.6. Uppermost Plio-Pleistocene Units D-H showing the internal structure of Unit G.	86
Figure 3.7 A-H. Contoured elevation maps of multiple interpreted surfaces on Banks Island shelf, overlying GEBCO sea floor bathymetry (200 m contours).....	87

Figure 3.8 A-K: Contoured isopach maps of interpreted surfaces on Banks Island shelf, overlying GEBCO sea floor bathymetry (200 m contours)	88
Figure 3.9. A-H: Facies maps overlain on top of contoured elevation maps, displayed in Figure 3.7 and GEBCO sea floor bathymetry (200m contours)	89
Figure 3.10 Seismic images (courtesy of ION) indicating relations of units within deep water.	91
Figure 3.11. Inner Banks Island shelf and westernmost Banks Island topography and seismic imagery.....	92
Figure 3.12. Climatostratigraphy of the Iperk Sequence, built upon Figure 1.2, illustrates a geological time scale, Pacific $\delta_{18}O_{Benthic}$ through time, a proxy for temperature, and sea level (m) through time, modified from Miller et al. (2020).....	98
Figure 3.13: Lithostratigraphic and sequence nomenclature of Late Cenozoic strata on Banks Island and within the Banks–Beaufort Basin, and within Amundsen Gulf.....	104
Figure 4.1. Block diagram illustrating an interpretation of the depositional environment of the Bfm during the Late Miocene and Pliocene.	115
Figure A.1. Sample PPI-17-103-001	131
Figure A.2. Sample PPI-17-103-002	131
Figure A.3. Sample PPI-17-103-007	131
Figure A.4. Sample PPI-17-103-008	132
Figure A.5. Sample PPI-17-103-009	132
Figure A.6. Sample PPI-17-110-020	132
Figure C.1. Composite photos of Section D8.....	147
Figure C.2. Cobble Sample PPI-17-103-003 in place	147
Figure C.3. Cobble Sample PPI-17-103-004 in place	148
Figure C.4. Cobble Sample PPI-17-103-005 in place	148
Figure C.5. Modern river incising into the bank of section D8, allowing our team to take advantage of modern erosion and access deeper sediments like the Bfm.....	149
Figure C.6. Sample PPI-17-103-006, loose sand sample used for $^{26}Al/^{10}Be$ burial dating, and could be used in future for ^{14}C dating.....	150
Figure C.7. Cobble sample PPI-17-103-007 in place.....	151
Figure C.8. Cobble sample PPI-17-103-008 (left) and cobble sample PPI-17-103-009 (lower right) in place.....	151
Figure C.9. Cobble sample PPI-17-103-010 in place.....	152
Figure C.10. Expanded version of Figure 2.6, Photo D-1. Silt and peat layers within section D8, approximately 3m up section.....	152

Figure C.11. Silt with minor indistinct horizontal stratification and a discernable peat layer within section D8	153
Figure C.12. Cross bedded sand facies, section D8.	153
Figure C.13. Similar section to Figure 2.6 Photo D-4. Large scale cross bedded sand facies, section D8... ..	154
Figure C.14. Expanded photo of Figure 2.6 Photo D-5. Cross bedded sands, becoming more planar and rounded at the top.	154
Figure C.15. Expanded photo of Figure 2.6 Photo D-6, approximately 18 m up section of D8. Noticeable peat lens within coarse sand beds.	155
Figure C.16. Cobbles sampled from 18 m up section of D8 (Figure 2.6 Photo D-6). Cobble was ultimately too small for analyses.	155
Figure C.17. Expanded photo of Figure 2.6 Photo D-3. Continuous planar bedding with coarse sandy facies, some minor lens of peat.....	156
Figure C.18. Peat and fine woody detritus layer within section D8.....	156
Figure C.19. Expanded photo Figure 2.6 Photo S-3. Planar facies within bedding, section S1, approximately 11 m up section.....	157
Figure C.20. Composite photos of section S1, a newly discovered section on Prince Patrick Island.....	157
Figure C.21. Section S1 at a distance, showing the modern stream incising into the section.....	158
Figure C.22. Large log sticking out of sediment approximately half-way up section S1	158
Figure C.23. Expanded photo Figure 2.6 Photo S-4. Large log sample within section S1, above planar bedding facies.	159
Figure C.24. Expanded photo Figure 2.6 Photo S-1. Trough cross bedding observed at base of section S1, 2 m from base of section.....	160
Figure C.25. Expanded photo Figure 2.6 Photo S-3. Woody detritus layer sticking out of section S1 (left) and close up shot of these woody detritus layers (right).....	161
Figure C.26. Woody detritus layer, section S1.....	162
Figure C.27. Expanded photo of Figure 2.6 Photo S-2. Coarse cross bedding sandy facies	162
Figure C.28. Expanded photo Figure 2.6 6B. Approximately 16 m up section, sand distinct red colour, interesting white features vertically cutting bedding.....	163
Figure C.29. Large log sample discovered at section S1	164
Figure C.30. Preserved tree rings within a large tree sample, likely Pliocene age	165
Figure C.31. Trough cross bedding facies within section S1 and erosional boundary between the bottom of the trough and the parallel bedding below	166
Figure C.32. Peat layer within section S1. Similar facies to Figure 2.6 Photo S-5.....	167

Figure C.33. Expanded photo of Figure 2.6 Photo 5B. Large peat layer and silty finely bedded layer with minor ripples, section S1, approximately 14 m up section..... 168

Figure C.34. Fine grained silty rippled bedding, section S1 168

ABSTRACT

During the Late Miocene to Mid-Pliocene (Messinian to Zanclean), global mean annual surface temperatures (MAT) averaged $>1^{\circ}\text{C}$ warmer than present and transitioned to much cooler climates over the next million years. Today, the MAT is 19°C cooler than the Pliocene MAT for the same location in the Canadian Arctic Archipelago (CAA), indicating a disproportionate thermal change in the Arctic owing to a shallower Pliocene latitudinal temperature gradient. There are few sites in tectonically quiescent areas that record the response of both onshore and offshore environments during this time of dramatic climate change. Arguably, one of the best locations to capture this climatogenic landscape and basin evolution would be in a polar setting where ice-free Late Cenozoic landscapes evolved to glacial environments earlier and more intensely than lower latitude sites. The Late Miocene to Pliocene Beaufort Formation (BFm), currently extending along the western CAA, is a fluvial deposit which once formed a contiguous coastal plain. The BFm represents the eastern limit of a westward thickening clastic wedge that extends across the continental shelf and into the Canada Basin. The BFm is partially coeval with the Iperk Sequence (IpS) offshore, a thick, currently submarine package of Late Miocene-Pleistocene fluvial and marine sediment in the Banks–Beaufort Basin. The BFm and IpS appear to have captured the response to the Pliocene climate transition, independent of tectonic uplift, and provide a useful study area to evaluate climatogenic basin evolution in the High Arctic.

The research goals of this thesis are to interpret and correlate the offshore and onshore stratigraphy to establish the history of sedimentation and progradation, the timing of faulting, and the factors controlling the basin's response to climate change in the High Arctic. Using recently released 2D seismic reflection data from ION Geophysical, a detailed seismostratigraphic framework of the IpS offshore Banks Island is compared with the equivalent seismostratigraphy in the Beaufort–Mackenzie Basin, previously an analogue for the Banks–Beaufort Basin. Eight sub-sequences were defined, and seismic facies analyses were conducted to correlate units across the shelf and upper slope to formulate a climatostratigraphy and interpret the depositional environments present, including the transition from onshore to offshore facies. A preliminary fault analysis within and at the mouth of M'Clure Strait reveals that at least this portion of the Northwest Passage does not appear to have been a graben system. Instead, the apparent absence of inter-island channel-parallel faults cutting Pliocene or younger deposits and the clear indication of deep erosion through the IpS and BFm supports the hypothesis that M'Clure Strait and Amundsen Gulf were likely formed by fluvial then glacial erosion. We present the first TCN cobble isochron burial age ($6.20 \pm 0.20(1\sigma)$ Ma) of the BFm on Prince Patrick Island, NWT, near the type locality. This age is the oldest numerical date for any BFm or equivalent unit in the CAA and supports previous biostratigraphic results inferring Late-Miocene environments on the island. The interpreted seismostratigraphy and new chronology contribute to our understanding of Late Cenozoic basin evolution in the CAA. This can be used to inform other ongoing Arctic investigations, such as the observed disparity between paleoenvironment and paleoclimate records among sites in the BFm, or the causes and consequences of deposition of such a large sediment volume during a climate transition, and spatio-temporal differences in the deposition of the BFm.

LIST OF ABBREVIATIONS AND SYMBOLS USED

AAR	Amino acid racemization
²⁶ Al	Aluminum-26
AMS	Accelerator mass spectrometry
asl	Above sea level
¹⁰ Be	Beryllium-10
BFm	Beaufort Formation
CAA	Canadian Arctic Archipelago
CRISDal	Cosmic Ray Isotope Sciences at Dalhousie Lab
DEM	Digital elevation model
ICP-OES	Inductive-coupled plasma-optical emission spectroscopy
ION	ION Geophysical Technologies
IpS	Iperk Sequence
LGM	Last Glacial Maximum
MAT	Mean annual temperature
ML	Marine limit
μA	microAmpere
TCN	Terrestrial cosmogenic nuclide

ACKNOWLEDGEMENTS

I want to thank the following people without whom, this research would not have been possible.

First, I owe a special thank you to my supervisor John Gosse. Your support and guidance, and comprehensive insights have made this an inspiring experience for me. Your encouragement has helped me become a better academic, writer, chemist, geologist, student, the list could go on. Thank you for pushing me when I needed it, for the hours of editing, and for helping this research be what it could be. I am sincerely going to miss your stories, inspiring anecdotes, and the best backyard barbecues around.

I want to thank my thesis committee, consisting of Adam Csank, Owen Sherwood, and Rod Smith, who provided invaluable contributions to my work. I greatly valued our discussions during our meetings; they challenged me to think deeper and more critically. Thank you for all your time and input towards advancing this manuscript at every stage of the process. Thank you also to my external examiner Neil Davies for your helpful comments on this manuscript's final version.

I owe a big thank you to our laboratory supervisor Guang Yang. Guang spent many hours in the lab with me, showing me how to perform a procedure, providing crucial advice when I didn't think a sample could get much cleaner, and constantly keeping track of where my darn bags of samples went. She is an all-knowing guru of the TCN lab, and I owe her my gratitude and thanks. Also, a big thank you to Sean De Roches who was a massive support in the final push of my samples in the lab and was constantly willing to extend a helping hand.

A special thank you to the folks at the Geologic Survey of Canada – Calgary, the Bedford Institute of Oceanography, and especially Ned King for all his helpful guidance on Chapter 2 of this thesis. The times spent following a seismic tie back and forth while we debated moving it up or down a centimeter ended up being some of my favorite days at the BIO and lead to some cool breakthroughs.

Additionally, I would like to acknowledge ION Geophysical for access to the BeaufortSpan seismic coverage in the Banks–Beaufort Basin, and Suncor for access to the historical Panarctic seismic data in M’Clure Strait.

To my lab mates over the years: Maya, Nora, Cody, Winson, Laura, Maureen, Sophie, and all the others involved with the lab in some way. You made lab meetings (virtually and non-virtually) fun and engaging and contributed towards a wholesome and supportive atmosphere.

To Seven Bays, where I wrote a LOT of my thesis, for providing me many late-night coffees, for the friendships fostered there, and for the many procrastination climbing sessions.

Finally, to my extensive support network of family and friends, without whom I would undoubtedly not be where I am today.

Chapter 1. Introduction

The Beaufort Formation (BFm) is a lithostratigraphic sequence of unconsolidated, mostly braided stream deposits that form a subaerially exposed and heavily dissected coastal plain, which stretches over 1200 km along the western Canadian Arctic Archipelago (CAA) (Figure 1.1; Fyles 1990). It represents the easternmost and uppermost component of a westward thickening marine clastic wedge across the continental shelf and into the Canada Basin. Some or all of the offshore Iperk Sequence (IpS), interpreted from offshore seismostratigraphy in the Canada Basin, has been proposed to contain the presently submarine extension of the BFm fluvial equivalent (Fyles 1990). The depositional and ecological paleoenvironments are captured in the large sediment volume and exceptionally well-preserved sedimentary and subfossil archives of the BFm and IpS. This record makes the BFm and IpS optimal to study basin evolution during the significant climate change occurring during the Pliocene-Pleistocene transition (Figure 1.2).

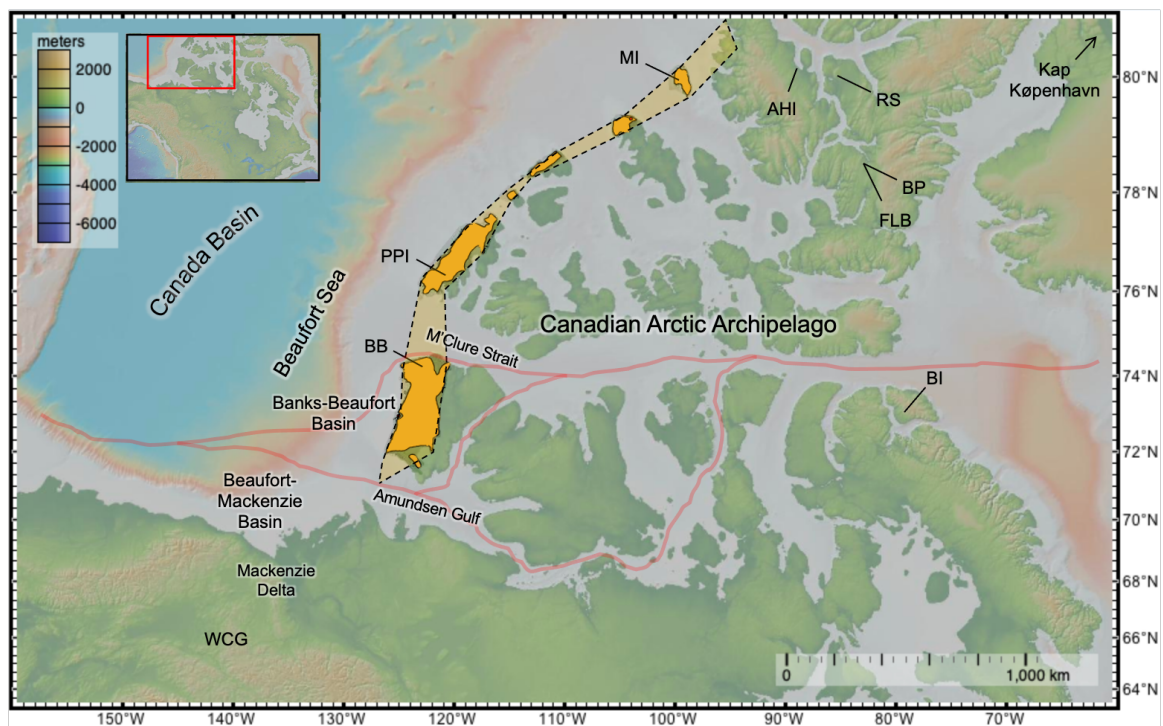


Figure 1.1. Map of the Canadian Arctic Archipelago (CAA) with locations of previous BFm and BFm equivalent studies. PPI- Prince Patrick Island (study site, Chapter 2), WCG-White Channel

Gravels, Yukon, BB-Ballast Brook, MI-Meighen Island, AHI-Axel Heiberg Island, RS-Remus Section, BP-Beaver Pond, FLB-Fyles Leaf Bed, and BI-Bylot Island. Kap København is located further northeast on northern Greenland and is younger than the BFm (Csank et al. 2013). Modern dissected subaerial exposures of the BFm (modified from Fyles (1990) are outlined in orange along the western edge of the CAA, displaying the ribbon-like distribution (transparent orange polygon, dashed lines). The location of both the Beaufort–Mackenzie Basin and Banks–Beaufort Basin (study area of Chapter 3) are shown as well as M’Clure Strait and Amundsen Gulf. The semi-opaque red line indicates the Parry Channel Northwest Passage and other variations, proposed sea routes between the Atlantic and Pacific oceans through the CAA.

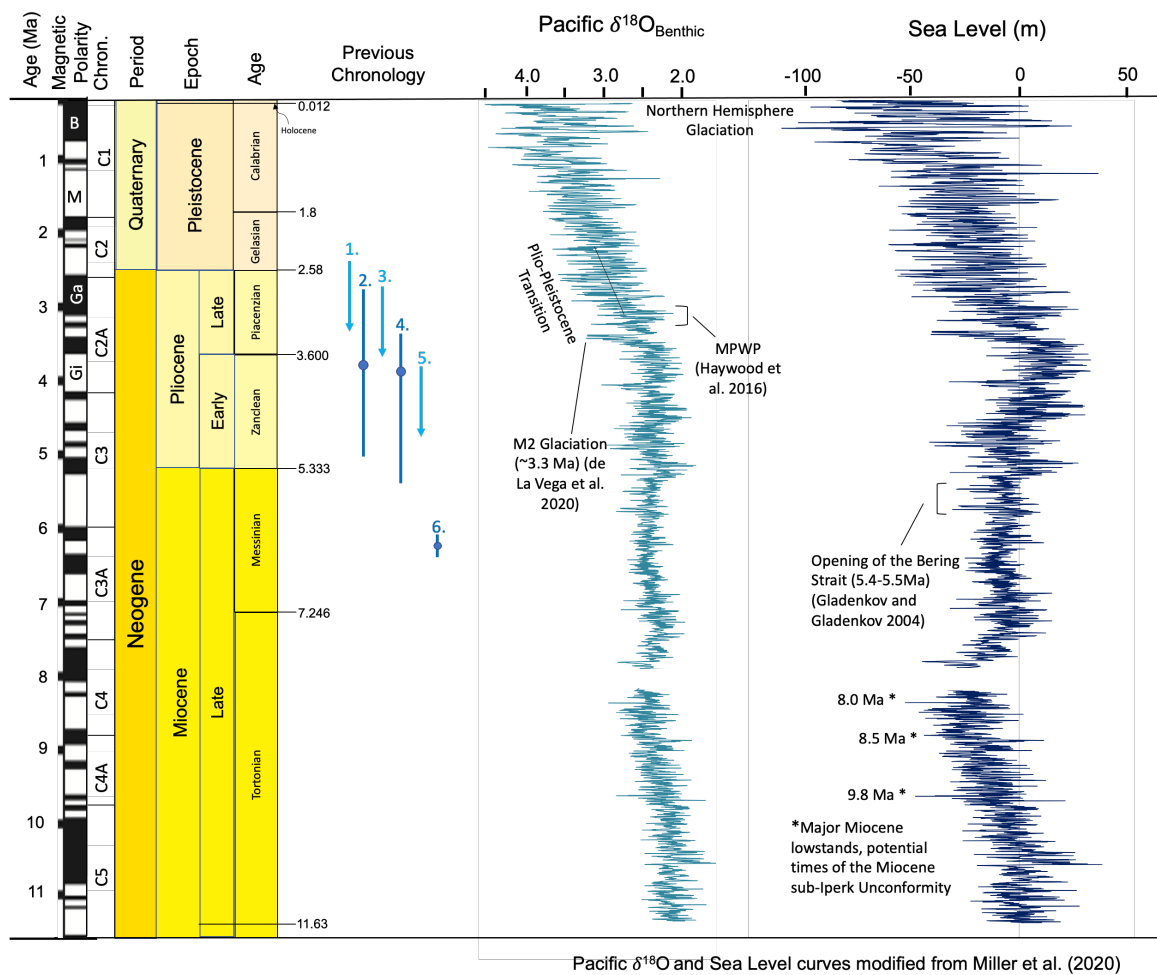


Figure 1.2. Geological time scale, Pacific $\delta^{18}\text{O}_{\text{Benthic}}$ and sea level curves through time, modified from Miller et al. (2020). Sea level at 0 m is present day. The previous chronology of the BFm is also illustrated. Major chronological events such as the opening of the Bering Strait (5.4-5.5 Ma) (Gladenkov and Gladenkov 2004) and the M2 glaciation (~3.3 Ma) (de la Vega et al. 2020) are

shown on the curves. The zone referred to as the Plio-Pleistocene transition and the Mid-Pliocene Warm Period are shown (MPWP)(Dowsett et al. 2010). Symbols for the magnetic polarity chrons are as follows: B: Brunhes (<0.78 Ma); M: Matuyama (0.78-2.59 Ma); Ga: Gauss (2.59-3.59 Ma); and Gi: Gilbert (3.59-5.25 Ma). Previous chronologies (at the left of $\delta_{18}\text{O}_{\text{Benthic}}$ curve) of the BFM across the CAA, including the new TCN isochron burial age from Prince Patrick Island, reported in Chapter 2 (number 6.). Other reported ages are as follows: 1: AAR ages (Brigham-Grette and Carter 1992); 2: Sr isotope dating (Kaufman et al. 1993) 3: TCN ‘simple’ burial age Banks Island (Braschi 2015); 4: TCN ‘simple’ burial age Beaver Pond Site (Fletcher et al. 2018) 5: TCN ‘simple’ burial age Fyles Leaf Bed (Rybczynski et al. 2013).

There are significant paleoenvironmental and paleoclimate disparities among different BFM and BFM equivalent sites across the CAA. These have triggered hypotheses regarding the role of latitude, continentality, and age in influencing paleoenvironmental conditions during the Pliocene (Fyles 1990, Matthews and Ovenden 1990, Ballantyne et al. 2010). It is unclear if these differences are simply due to variations in continentality between otherwise contemporaneous sites, or significant age differences between multiple locations (Matthews and Ovenden 1990). A chronostratigraphic framework of the BFM is essential to provide a context for these paleoclimate and paleoenvironmental proxies, compare and contrast with existing chronologies, and provide context with other significant landscape changes in the Arctic. However, there remains a significant lack of chronological control of the BFM.

The IpS contains fluvial, glacial, and marine sediments, parts of which are thought to be coeval with the BFM. However, this correlation has not been well established, and as such, is a crucial, underexplored component in the current understanding of arctic basin evolution. Despite its considerable thickness (> 3km) and shallow position, the IpS has yet to be subdivided into its Pliocene and Pleistocene components (necessary to analyze basin evolution through time) primarily due to the lack of petroleum well control and marine seismic coverage and resolution needed to correlate its multiple phases on a basin-wide scale (Dixon et al. 1992). The southern Beaufort–Mackenzie Basin has largely been used as an analogue for the nearshore stratigraphy of the IpS in the Banks–Beaufort Basin (Blasco et al. 1990, Dixon et al. 1992). This is despite facies trends, paleoflow measurements, and sediment provenance suggesting the two basins have

fundamentally different sediment sources and should not be equated. This first attempt to subdivide and analyze the Pliocene and Quaternary stratigraphy within the IpS in the Banks–Beaufort Basin is timely and essential to increase our understanding of the Late Miocene to Pleistocene basin evolution in the Banks–Beaufort Basin. Additionally, an analysis of the relationship between the origin and deposition of the IpS and its relationship to the formation of the inter-island channels is crucial. This will contribute to our understanding of the mechanism and timing of incision of these channels and what may have been an important erosional event and change in ocean circulation that significantly altered the CAA from a continental climate to an archipelago with more maritime influences.

1.1 Previous Beaufort Formation and Equivalent Studies

The presence of distinct fluvial sediment units that make up the BFm were recognized by explorers as far back as the 19th century (Mecham 1855, Heer 1868). It was described and named a century later (Tozer, 1956), and a type locality was designated on Prince Patrick Island. In the subsequent decades, BFm sediments would be recognized and described on all the western CAA islands facing the Beaufort Sea in both outcrops and petroleum exploration wells (Miall 1979). They were distinguished from other unconsolidated fluvial deposits in the western CAA by the presence of subfossilized wood and from underlying Middle Miocene strata (Ballast Brook Formation) whose subfossil wood was characterized as being more coalified and compressed (Fyles et al. 1994, Williams et al. 2008). The BFm was described in detail at multiple sections across the CAA. These includes ‘the Gap’ on Meighen Island, which is the only known locality of the BFm with marine (estuarine) strata and is the northernmost mapped exposure of the BFm, *sensu stricto* (Fyles et al. 1991, Davies et al. 2014) (Figure 1.1- MI). Other sections include the Ballast Brook site on northwestern Banks Island, one of the southernmost, and most laterally extensive exposure of the BFm (Fyles et al. 1994, Braschi 2015) (Figure 1.1 - BB). The type locality of the BFm is located on Prince Patrick Island (Tozer 1956, Fyles 1990, Devaney 1991) and is also the study area for Chapter 2 of this thesis (Figure 1.1- PPI).

Other sites *sensu lato* (otherwise described as BFm equivalent) include the Fyles Leaf Bed (Figure 1.1 - FLB), Remus Section (Figure 1.1 - RS), and Beaver Pond sites on Ellesmere Island (Figure 1.1 - BP) (Rybczynski et al. 2013, Fletcher et al. 2018). These localities are not coastal plain deposits, however, they may be distal sources of contemporaneous sediments coeval with the deposition of the BFm. As described by (Fyles 1989), these ‘high terrace sediments’ on Ellesmere Island comprise sediment from a range of terrestrial depositional environments, including lacustrine, fluvial, paludal, and alluvial fans (Fyles 1989, Rybczynski et al. 2013, Fletcher et al. 2018). Samples from the Klondike district of Yukon (Figure 1.1 - WCG) are also considered contemporaneous, although not a part of the BFm itself (Hidy et al. 2013).

The defining characteristic of the BFm is the presence of well-preserved botanical and fauna subfossil remains, in particular, an abundance of wood fragments, which inform Late Miocene to Pliocene paleoecology and paleoclimatology in the western and high CAA (Matthews 1989, Matthews and Ovenden 1990, Devaney 1991, Csank et al. 2011, Rybczynski et al. 2013). These subfossils include mosses, pollen, plant macrofossils, and arthropods (e.g., Hills and Ogilvie 1970, Hills et al. 1974, Fyles et al. 1994), and species now found only south of the CAA, such as cedar, larch, and birch (Matthews and Ovenden 1990). Deerlet, rabbit, beaver, and camel fossils (Tedford and Harington 2003, Rybczynski et al. 2013) are just some of the vertebrate fossils that have been uncovered from BFm and contemporaneous sediments in the CAA. Few other known sedimentary units of this age have comparable fauna, making this fossil record unique globally (Tedford and Harington 2003). Additionally, the mummification of plant and animal remains within what has become a cold, polar-desert environment may have allowed the preservation of organic molecules and could be used for DNA extraction studies in the future (cf. Valk et al. 2021).

Proxies extracted from the BFm and BFm equivalent sediments have been used to establish numerous paleoclimate records (Csank et al. 2011, 2013, Fletcher et al. 2017, 2019). Mean annual temperature (MAT) has been estimated by several methods, including fossil beetles (Elias and Matthews 2002), oxygen isotopes in tree cellulose, tree ring widths (Csank et al. 2011), and bacterial tetraether composition in paleosols (Ballantyne et al. 2010). During the Pliocene, global MATs were approximately 2°C

warmer than present. However, due to a shallower latitudinal temperature gradient, Pliocene CAA local MATs were up to 19°C warmer than today (Ballantyne et al. 2010). These records hold important documentation of Arctic climate during a period when global warmth is comparable to predicted temperature projections within the next century (Masson-Delmotte et al. 2013).

Previous dating attempts of the BFm have included biostratigraphy (Hills and Ogilvie 1970, Hills et al. 1974, Matthews 1989, Matthews and Ovenden 1990, Fyles et al. 1994), magnetostratigraphy (Fyles et al. 1994, Barendregt et al. 1998, *in prep*), and numerical methods such as cosmogenic $^{26}\text{Al}/^{10}\text{Be}$ burial on quartz sand (Hidy et al. 2013, Rybczynski et al. 2013, Braschi 2015, Fletcher et al. 2018), amino acid racemization (AAR) (Brigham-Grette and Carter 1992), and $^{87}\text{Sr}/^{86}\text{Sr}$ isotope correlation dating of marine shells (Fyles et al. 1991, Kaufman et al. 1993). These previous numerical dating attempts have narrowed the deposition of the BFm to the Pliocene (5.33 – 2.60 Ma; Figure 1.2), however, the biostratigraphy suggests the BFm could be as old as the Late Miocene (Hills and Ogilvie 1970, Matthews and Ovenden 1990). Significant limitations associated with the dating methods used, and variability in acquired results (Figure 1.2), suggest that further chronological control is necessary to increase our understanding of the deposition of the BFm.

1.2 Thesis Questions & Objectives

This thesis's overarching goal and primary objective is to improve our knowledge of the composition and evolution of the BFm and the contemporaneous IpS offshore sediments with the Banks–Beaufort Basin. Short term objectives include:

Chronostratigraphy:

1. Establish the depositional age of the BFm near its type locality on Prince Patrick Island, NWT, within the context of previously described and new sedimentological investigations:
 - 1.1 Use terrestrial cosmogenic nuclides (TCNs) to establish the burial age of sediment in thick sections
 - 1.2 Use the cobble isochron burial dating method to acquire a more precise age on the BFm relative to previous TCN approaches to date contemporaneous sediments

- 1.3 Determine if the new numerical chronology is consistent with the interpreted range of biostratigraphic ages (Late Miocene to Pleistocene) and with existing chronology
2. Measure paleoflow within the BFM sedimentology on Prince Patrick Island to help constrain the timing of formation of the adjacent M'Clure Strait

Marine Seismostratigraphy:

3. Interpret the recent marine seismic reflection data from ION in the Banks–Beaufort Basin to define stratigraphy within the IpS:
 - 3.1 Distinguish and interpret Miocene, Pliocene, and Pleistocene stratigraphy and their internal facies
 - 3.2 Identify transgressions and unconformities to link with the Ballast Brook/BFM unconformity
 - 3.3 Identify potential paleoshorelines
 - 3.4 Determine volumetrically the sediment flux and its general change with time.
 - 3.5 Test for the presence of fault systems within or at the mouth of M'Clure Strait and Amundsen Gulf that can support the hypothesis that they formed as grabens

Several questions have motivated the research of this thesis. These include:

1. What is the age and duration of the BFM, and how does this relate to other BFM sites from which paleoecological and paleoenvironmental records have been extracted?
2. Did the inter-island channels, including M'Clure Strait, form tectonically (i.e., faulting) or by erosion, or a combination of both?
3. What aspects of the onshore BFM and offshore IpS sediments represent a response to a significant climate change during the Plio-Pleistocene transition?

1.3 Result Highlights and Significance

Result highlights include the first $^{26}\text{Al}/^{10}\text{Be}$ TCN cobble isochron burial age of the BFM from Prince Patrick Island (6.20 ± 0.20 (1σ) Ma) and the first successful application of the $^{26}\text{Al}/^{10}\text{Be}$ cobble isochron technique in Canada. The stratigraphy and sedimentology of the BFM on Prince Patrick Island was revisited and multiple sections were compared. The 6.20 ± 0.20 Ma age provide a framework and context to the multiple paleoclimate and paleoenvironmental records that are present within the BFM. Paleoflow measurements of the BFM on Prince Patrick Island were measured with a dominant flow towards the WSW. This result suggests there was not a major depression in the area of present-day M'Clure Strait, even above contemporaneous sea level, that was diverting paleoflow towards it. This has implications towards the formation/incision of the inter-

island channels, the opening of which may have been caused a significant change to ocean circulation in the High Arctic.

Seismic stratigraphy of the IpS in the Banks–Beaufort Basin revealed a thick package (>3 km) of sediments ranging in age from the Late Miocene to the Pleistocene. Eight distinct stratigraphic units were identified within the IpS, and from this, a climatostratigraphy was established. The volume of sediment deposited in the Banks–Beaufort Basin shelf and slope from the Late Miocene through Pleistocene was estimated, allowing inferences about how climate may have impacted the basin evolution. A preliminary fault analysis of the Banks–Beaufort Basin shelf and slope and adjacent inter-island channels was conducted. This result has implications for how they were formed and provides an estimated age of incision. Previous work by Batchelor et al. (2013a, 2013b, 2014) is expanded upon, and an additional glacial unit below their basal surface was identified, extending the history of shelf-crossing glaciations on the Banks–Beaufort Basin shelf. Although shorelines and other lowstand features are not readily resolvable on the ION data, a facies depositional model within the IpS units allowed for inferences of their location, 40-50 km off the Banks Island modern-day shoreline. These conclusions may contribute towards a global database from which sea level and ice sheet models are constrained.

Overall, this thesis’s results will contribute knowledge of the late Cenozoic evolution of the western CAA and broaden understanding of how these northern landscapes responded to large-scale climate change.

1.4 Thesis Design

This thesis has four chapters.

Chapter 1 provides a brief background for the study, the research problems, objectives, and an overview of the results and their implications.

In Chapter 2, the first TCN cobble isochron age of the BFM on Prince Patrick Island is presented, along with an updated sedimentology and stratigraphy of two sections proximal to the type locality (gathered during a 2017 field expedition to Prince Patrick Island). The geochronology will improve our ability to correlate the isolated paleoclimate

records on different islands, test hypotheses regarding paleoenvironmental changes, and link them to global and regional paleoclimate and paleoceanographic changes.

The main focus of Chapter 3 is interpreting the IpS in the Banks–Beaufort Basin offshore. Here, recently acquired marine seismic reflection data from ION and sequence stratigraphic methods are used to subdivide the IpS into six Late Miocene to Pleistocene units and two Late Pleistocene units. Several depositional environments, including transitions from onshore to offshore facies, are identified using seismic facies attributes. Using these depositional environment models, verified with higher resolution acoustic data (sub-meter sub-bottom profiler transects and GEBCO generated profiles), a suggested location of paleoshorelines has been proposed 40-50 km offshore. Several units with glacial sedimentary facies within the IpS have been identified, and the potential onset of grounded ice on the Banks Island shelf has expanded the glacial sedimentological history offshore Banks Island. A fault analysis within the inter-island channels and paleoflow in the Bfm on Prince Patrick Island has implications for the opening of the inter-island channels such as M’Clure Strait. We discuss the implications of these data in relation to major transgressive sequences and Arctic basin evolution during a period of significant climate change.

Chapter 4 summarizes the key findings of both chapters 2 and 3 and identifies the implications of this research. It also outlines future work for which the previous chapters form a basis.

Chapter 2. Beaufort Formation Chronostratigraphy, Prince Patrick Island, Northwest Territories

Manuscript in preparation for submission to *Geology* or *Quaternary Geochronology*. My contributions include (i) writing the manuscript and making modifications based on suggested edits from co-authors; (ii) creating all the figures and tables within this manuscript; (iii) completing all laboratory, data reduction, and calculations of the burial ages; (iv) conducting the sedimentology and stratigraphic descriptions of the two sections; (v) assisting with the collection of subfossilized wood in the field; (vi) conducting the required field work and sample collection; and (vii) contributing to the planning for the field season

Sydney A. Stashin (1), John C. Gosse (1), Adam Csank (2), Natalia Rybczynski (3)

(1) Department of Earth Sciences, Dalhousie University, Halifax, Nova Scotia B3H 4R2

(2) Department of Geography, University of Nevada, Reno, Nevada 89557

(3) Department of Paleobiology, Canadian Museum of Nature, Ottawa, Ontario, K1P 6P4

2.1 Abstract

The Beaufort Formation (BFm) represents a coastal plain remnant of a westward thickening clastic wedge deposited almost entirely across what is now the western Canadian Arctic Archipelago (CAA). Unconsolidated quartz-rich sandy braided stream beds locally include gravel channel lag facies and thin peat layers. The BFm was deposited during the Late Miocene and Pliocene. Thus, the BFm captures one of the world's best records of a rapidly accumulated then truncated basin-fill during the Pliocene-Pleistocene climate transition. While its thickness in exposed sections on Prince Patrick Island is <40 m, the formation is interpreted to have been >3 km thick offshore. There is evidence for significant (200-400 m) erosion of the formation before the deposition of Quaternary glaciofluvial deposits above. The BFm is also known for its abundance of subfossils (isotopically and biochemically intact forest, faunal, and other organic remains) that provide important paleoenvironmental insights. However, the BFm remains poorly dated, leaving evolutionary and climate hypotheses untested and the rates

and timing of the basin evolution unresolved. Here, we report the first numerical age for the BFm on Prince Patrick Island (near the type locality) and the first cobble isochron age in Canada ($6.20 \pm 0.20(1\sigma)$ Ma). This age broadly supports previous biostratigraphic age estimates and extends the BFm into the Late Miocene (Messinian).

2.2 Introduction

The Beaufort Formation (BFm), initially defined by Tozer (1956) and most recently by Fyles et al. (1994), is a sequence of braided stream sediments deposited across a contiguous arctic coastal plain that subsequently has been dissected to form the inter-island channels that make up the CAA (Figure 2.1). It thickens offshore from >1 km immediately off the west coast of Prince Patrick Island to >3 km in the Banks–Beaufort Basin (part of the Canada Basin) (Miall 1979, Fyles et al. 1994). The name BFm was applied to generally similar fluvial strata on all the islands facing the Arctic Ocean (Figure 2.1) from Meighen Island to Banks Island (Tozer 1956, Fyles 1990). Other sites including the Remus Section and the ‘high terrace sediments’ on Axel Heiberg and Ellesmere Islands (Figure 2.1) are not coastal plain deposits, however, they may be distal sources of contemporaneous sediments coeval with the BFm (Bustin 1982, Fyles 1989). Samples from the Klondike district of Yukon (Figure 2.1) are also considered contemporaneous, although not a part of the BFm itself (Hidy et al. 2013). Previous chronologies have suggested that the BFm was deposited during the Pliocene, an epoch directly followed by a period of intense climate reorganization during the Plio-Pleistocene transition (Rybczynski et al. 2013, Braschi 2015, Fletcher et al. 2018, Miller et al. 2020). Previous paleoflow and sediment provenance measurements have suggested the provenance of BFm sediment on Prince Patrick Island is due east, including proximal sources from a region currently occupied by Eglinton and Melville Islands and surrounding water bodies, or distal sources as far as the Canadian Shield (Miall 1979, Bustin 1982, Fyles 1990, Fyles et al. 1994). Tectonically induced vertical changes in the late Neogene and Quaternary have never been reported for the paleo-catchment of Prince Patrick Island, so it seems probable that the high volume of sediment deposited in the BFm is a response to a significant climate change, independent of tectonic uplift. As

such, the BFm could provide a robust record of large-scale landscape changes that occurred in the Arctic during a period of intense climate reorganization.

The existing chronology of the BFm is based on biostratigraphy, amino acid racemization (AAR), $^{87}\text{Sr}/^{86}\text{Sr}$ isotope dating, and terrestrial cosmogenic isotope (TCN) ‘simple’ burial dating. These tentatively place the BFm in the Messinian to Piacenzian range. Large uncertainties in the dating methods and the stratigraphic context for the interpreted ages limit the precision and accuracy at any one location.

After seven decades of stratigraphic, basin evolution, biostratigraphic, paleoenvironmental, and paleoclimate studies, this study provides a numerical age of the BFm near its type locality, $6.20 \pm 0.20(1\sigma)$ Ma. This age is attributed to the middle part of a >35 m thick section near the type locality for the BFm sandy braided stream deposits, below an erosional unconformity and a gravel facies likely from Quaternary glaciofluvial outwash deposits. This date is supported by and therefore confirms previously published biostratigraphic age estimates of Late Miocene floral and faunal remains (Matthews and Oviden 1990). It is the oldest of any previously reported numerical age estimates for the BFm on Meighen, Banks, or Ellesmere Islands. It suggests that a strictly Pliocene age, often cited for the BFm, is not accurate. It also provides a minimum limiting age for the offshore lithostratigraphically-correlated Iperk Sequence (IpS) (Dixon et al. 1992, McNeil et al. 2001). The date triggers a caveat when assuming approximate synchronicity when interpreting similarities and differences in paleoclimate and biogeographic information at BFm sites spaced over 1200 km along the western CAA.

2.3 Background

The BFm is a sequence of braided fluvial deposits and currently outcrops on the western edge of the CAA (Figure 2.1, solid yellow). It extends westward to form a thick clastic wedge in the offshore Canada Basin and comprises part of the IpS (Tozer and Thorsteinsson 1964, Fyles et al. 1994). The presence of these distinct organic-rich sediments was recognized by explorers as far back as the 19th century (Mecham 1855, Heer 1868); however, Tozer (1956) was the first to formally name the BFm deposits as

well as designate a type locality near Mould Bay, Prince Patrick Island. The BFm sediments were eventually recognized and described on all the western islands of the CAA. ‘High terrace sediments’, described at multiple sites on Axel Heiberg and Ellesmere Island (Bustin 1982, Fyles 1989, Rybczynski et al. 2013) and the White Channel Gravels in the Klondike district of the Yukon (Hidy et al. 2013, 2018), while not entirely composed of braided stream sediments, have also been interpreted as contemporaneous deposits, and are sometimes referred to as BFm equivalents, or BFm *sensu lato*. The former total thickness of the BFm onshore is unclear, but Manion (2017) suggests that based on lithosphere flexure modeling, up to 400 m of BFm sediments may have been eroded from the CAA since the Pliocene.

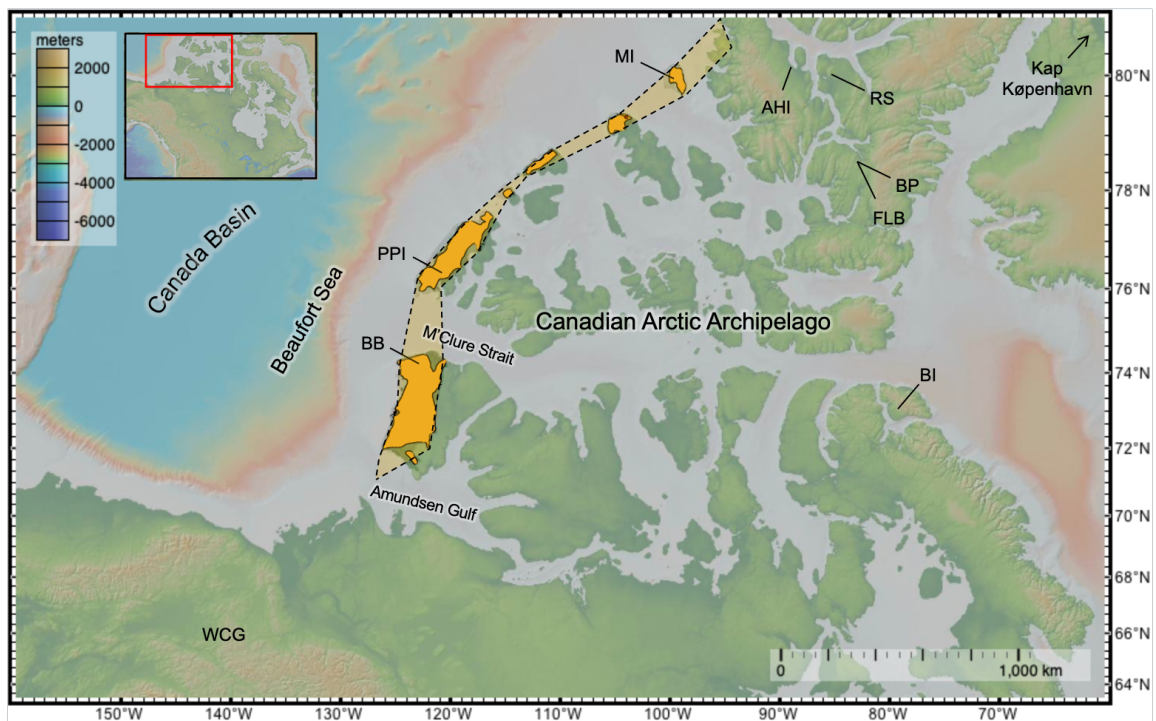


Figure 2.1. Map of the Canadian Arctic Archipelago with the locations of previous BFm and equivalent studies (*sensu stricto* and *sensu lato*), modified from Gosse et al. (2017). The modern dissected subaerial exposure of the BFm deposits is outlined in orange along the western edge of the CAA (modified from Fyles (1990), displaying the ribbon-like distribution (transparent orange polygon, dashed lines). Previous studies sites include PPI – Prince Patrick Island (study site of this chapter), WCG – White Channel Gravels, Yukon, BB – Ballast Brook, MI – Meighen Island (also known as ‘the Gap site’, AHI – Axel Heiberg Island, RS – Remus Section, BP – Beaver Pond Site, FLB – Fyles Leaf Bed, and BI – Bylot Island.

The defining characteristic of the BFM is the presence of remarkably unaltered, subfossilized woody detritus. This includes water-worn sticks and fragments, small detrital trees with branches, roots, and preserved bark, in-situ stumps and logs (up to 40 cm in diameter, and several metres long, Fyles 1990), and bedding plane mats of fine plant material and woody detritus up to 0.5 m thick (Matthews 1989, Matthews and Ovenden 1990, Devaney 1991). The BFM sediments also include subfossil mosses, pollen, plant macrofossils, and arthropods (e.g., Hills et al. 1974), and locally extinct species now found only in Eurasia or south of the CAA, such as cedar, larch, birch (Matthews and Ovenden 1990), and camel (Rybczynski et al. 2013).

The presence of this subfossil record has enabled estimations of MAT by several methods, including the coexistence of fossil beetles (Elias and Matthews 2002, Ballantyne et al. 2010), oxygen isotopes in tree cellulose, annual ring width (Csank et al. 2011), and bacterial tetraether composition in paleosols (Ballantyne et al. 2010). Estimates show that the MAT in the CAA was approximately -0.5°C (19°C warmer than present day, Ballantyne et al. 2010, Csank et al. 2011). This is the last period in Earth's history where sustained global temperatures exceeded those of today (Ballantyne et al. 2010) and coincided with CO_2 concentrations that were 365 to 415 ppm, similar to current levels (Pagani et al. 2010). In the Late Pliocene, the climate in the CAA began to deteriorate, as the climate system was reorganized from a state of restricted local glaciers to a state of extensive hemispheric ice sheet cycles (Haywood et al. 2009) (Plio-Pleistocene transition, Figure 1.2). Changes in lithospheric flexure (Manion 2017), glacial isostasy (Raymo et al. 2011), global sea level changes (Mudelsee and Raymo 2005), paleoceanography changes (temperatures, sea ice, and circulation, (Matthiessen et al. 2009), loss of Pliocene forests (Csank et al. 2011), and increased permafrost activity (Rybczynski et al. 2013) all accompanied the climate transition in what is now the CAA.

Interestingly, the Pliocene MAT and paleoenvironmental reconstructions interpreted at different CAA sites have significant differences and are a current source of study and debate (Gosse et al. 2017). For instance, the Prince Patrick Island BFM floras contain taxa (e.g., *Epipremnum crissum*, *Microdiptera/Mneme*, *Cleome*, and *Metasequoia*) which have not been found on Meighen Island (despite investigation of several deposits and

large collections of plant macrofossils; Matthews and Ovensen 1990). The cause of these paleoclimate and paleoenvironment disparities among the different sites has not yet been resolved.

2.3.1 Previous Chronology

Previous chronologies on the BFM were either imprecise (biostratigraphy, $^{87}\text{Sr}/^{86}\text{Sr}$, or AAR) or, in the case of magnetic polarity, needed a single depositional age to pin hanging polarity records for many of the islands (Fyles et al. 1994, Barendregt et al. 1998). Although the ‘simple’ cosmogenic nuclide burial dating approach had been previously employed in contemporaneous sections of ‘high terrace sediments’ on Ellesmere Island (yielding ages of 3.8 ± 0.2 and 3.9 ± 0.2 Ma; Rybczynski et al. 2013, Fletcher et al. 2019), the uncertainties were too high to allow correlation (or exclusion of correlation) to numerous paleoenvironmental indicators also discovered within the sections. Cosmogenic nuclide isochron burial dating with the depth profile method was attempted at Meighen Island and Banks Island (Braschi 2015, Gosse et al. *in prep*). However, difficulties related to possible post-burial muonic production needed to be resolved before final interpretations could be made. Additionally, the high uncertainties from attempts made on Meighen Island and Banks Island were likely because of a probable high erosion rate in the paleo-catchment, which results in low ^{10}Be and ^{26}Al concentrations in the quartz sand, and short exposure times in the rare paleosols. This resulted in the inability to create sufficient differences in concentrations of samples at different depths in and below the possible soils (Braschi 2015). The cobble-based isochron approach was not possible at those locations because sufficiently large quartz-rich cobbles could not be found in suitable positions at deep enough depths.

2.4 Methods

The principal objective of the 2017 field season on Prince Patrick Island was to date the BFM near its type locality, using the cobble-based isochron cosmogenic nuclide approach. If the cobble isochron method can be applied at Prince Patrick Island, it would provide a potentially robust and precise age for at least one location of the BFM. It would also support future attempts to date the BFM with the isochron method.

Secondary objectives for the Prince Patrick Island field season included: (i) collection of dozens of disks sawed through subfossilized trees for dendrochronology and isotopic analyses, which is ongoing at University Nevada Reno by A. Csank; (ii) collection of various paleoenvironmental specimens (under a NWT paleontology permit) which are currently being studied at the Canadian Museum of Nature by N. Rybczynski and colleagues; and (iii) mapping of BFM beyond the limits mapped by Fyles (1990) and Devaney (1991); and (iv) mapping and interpretation of the dynamics and offsets of fault lines and scarps that were identified with remotely sensed images, aerial photographs, and the ArcticDEM (Release 4, v2.0, Polar Geospatial Center), that have spatially been related to earthquake locations (USGS Search Earthquake Catalog). This last objective was not achieved. While we made it to several of the targeted fault line locations (based on GPS), no site had any morphometric indication of a fault line. It appears that the periglacial reworking of surface materials in this region has effectively obliterated any scarps that could be associated with the presumed faults in the field area (Figure 2.2). Fuel limitations and long distances that could not be effectively traversed via 250 cc all-terrain vehicles over muddy saturated terrain were also factors. Helicopter reconnaissance is highly recommended for future paleoseismology work performed on Prince Patrick Island.

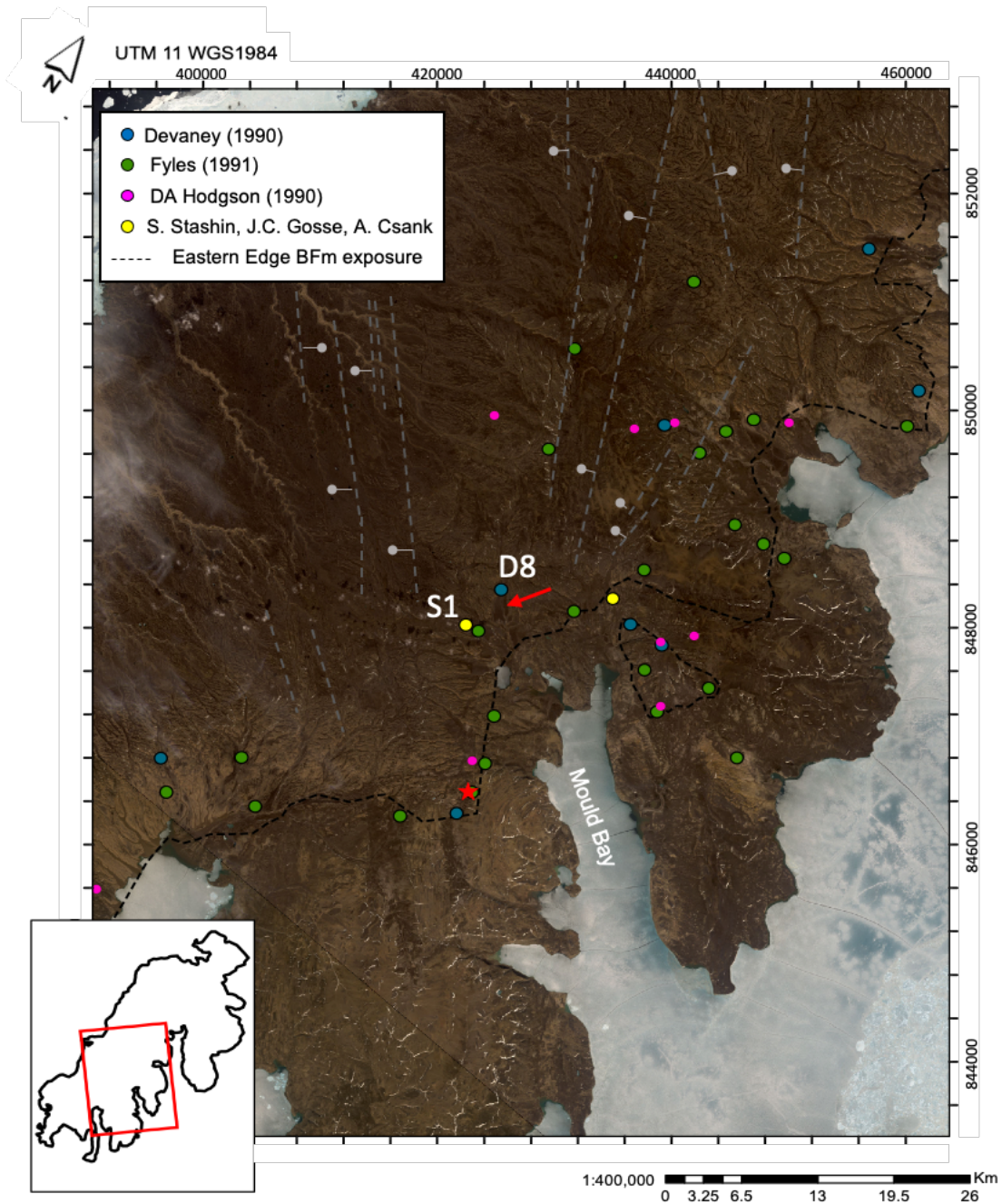


Figure 2.2. Landsat image of Prince Patrick Island, displaying previously visited field sites. Green dots are from Fyles (1990), blue dots are from Devaney (1991), pink dots are from Hodgson (1990, pers. comms 2017), and yellow dots (this study) are from additional sites of interest that were recognized with fresh stream cuts from air photos and 5m ArcticDEM data (Release 4, v2.0, Polar Geospatial Center). The red star is the location of the type locality of the BFm (Tozer, 1956), while the red arrow indicates our landing area and campsite ($76^{\circ}24.068'N$, $119^{\circ}51.197'W$). The grey dashed lines illustrate multiple large-scale faults on Prince Patrick

Island (Harrison et al. 1988) and were the target of a secondary objective of the 2017 field season. The black dashed line is the eastern mapped extent of the BFm, based on Fyles (1990).

2.4.1 Interpretation of aerial photographs and remotely sensed images prior to field work

Challenges of field work that required pre-field season planning included: (i) difficulty in accessing multiple sites in highly incised terrain, requiring either helicopter (too expensive) or ATVs (difficult to maneuver over long distances in muddy saturated terrain); (ii) locating high (>20 m), steep sections in the BFm that were not buried under frozen colluvium; (iii) identifying a centrally located field camp near the type locality and where previous field notes and reports indicated the presence of subfossil organic materials or wood, fault line targets (Figure 2.2); and (iv) a suitable surface that could serve as a runway near the field camp where a Twin Otter aircraft could land and depart with field party, equipment, and samples.

Multiple sites of interest were identified from Fyles' (1990), Devaney's (1991), and D.A. Hodgson's field notes (Hodgson 1990, Taylor and Hodgson 1991, Hodgson et al. 1994). Other novel sites were identified at fresh stream cut exposures visible on 5m ArcticDEM imagery (Release 4, v2.0, Polar Geospatial Center). We chose fault line targets to visit based on scarps with the most recent seismicity (a 1998 magnitude 4.1 earthquake at 18 km depth, which had occurred on a fault north of our landing site) to increase our chances of observing potential offset.

Ultimately, in the field, we could access two river-cut >30 m sections (Figure 2.2). Devaney (1991) had previously documented one section (D8) (Figure 2.2, Figure 2.3, D8)(76°24'41.52"N; 119°51'34.56"W); the second site was not previously documented (Figure 2.2, Figure 2.3, S1) (76°23'8.99"N, 119°57'9.97"W). Composite photos of both sites are illustrated in Appendix C.

2.4.2 Sedimentology field methods

While previous sedimentology by Devaney (1991) provided a generalized overview of the BFm on Prince Patrick Island, including section D8, we outline a detailed sedimentological description to provide context for the cosmogenic nuclide burial dating.

This included observations such as soils, peat layers, unconformities, evidence of glaciotectonism, or other indicators such as striated clasts, subfossils, and unique lithologies to establish that the section was indeed BFM braided stream sediments and suitable for sampling for geochronology. Section D8 was excavated with spades, picks, and folding shovels from top to bottom in a horizontal step-wise manner that permitted examining the entire section face laterally and vertically, following key layers such as peat or gravel. A similar approach was taken at section S1. The sections were surveyed with a laser rangefinder for precise heights using prominent features on the cliffside as references. Sedimentological field observations including structures, grain size, clast lithology and roundness, architectural units (e.g., braid bars, peat layers, unconformities), and paleoflow were recorded.

2.4.3 Geochronology field methods

The objective for collecting the TCN samples was to collect multiple high-quality cobble samples for the isochron TCN burial dating method and produce an accurate age of the BFM. Loose sand samples were also collected to use the 'simple' burial dating TCN method. Samples were collected with the objective to calculate basin-wide average erosion rates during the deposition of the BFM from the measured ^{10}Be . Modern stream sand samples were collected to calculate modern basin-wide average erosion rates to compare to paleo-erosion rates in the catchment.

A total of 21 samples were collected (18 cobbles and 3 sand samples, Table 2.1), with 10 samples ultimately prepared for cosmogenic nuclide burial dating. Samples were collected at depths >20 m to reduce uncertainty related to post-burial nuclide production (from deeply penetrating muons; c.f. Gosse and Philips 2001). For isochron burial dating, cobble samples were collected in place from undisturbed beds. Figure 2.3 illustrates the depths the samples were collected on section D8, and Figure 2.4 shows three of the quartz arenite cobble samples collected at 23.5 m depth from within a cross-bedded sand facies. Only cobble samples above a particular size (>64 mm diameter) and quality (preferably quartz-rich lithologies) were collected. Quartz arenite samples were favoured for the highest percentage of quartz, and size limits reflect minimum required abundances

of quartz grains for TCN burial dating. Appendix A includes photos of each cobble sample that was processed.

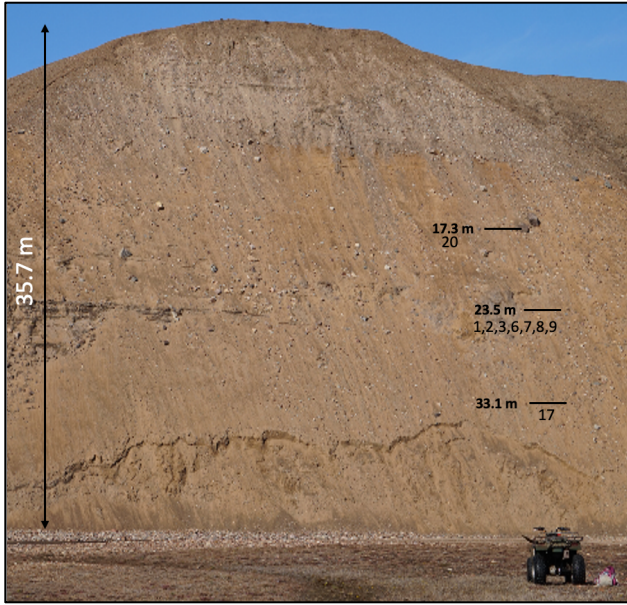


Figure 2.3. Field photo of section D8, with locations and depths of samples indicated. One modern stream sample was collected from an alternate location near base camp. While 21 samples were collected from this site, only those processed for TCN isochron and burial dating are illustrated. Sample field IDs are abbreviated from PPI-17-10Y-00X where 00X corresponds with the sample number on the figure.

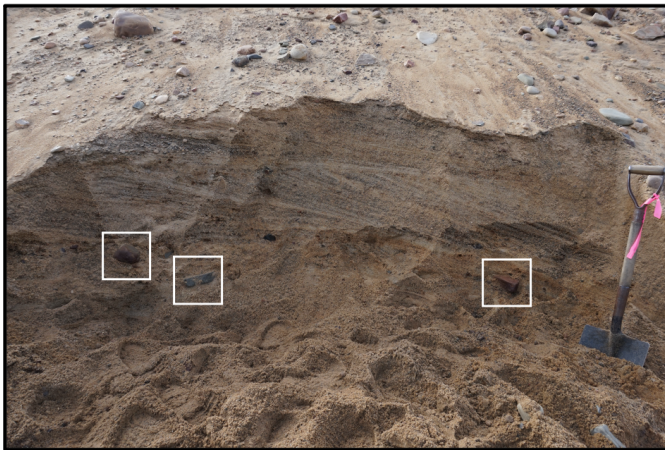


Figure 2.4. Photo of a section of D8 at 23.5 m depth (line drawn on Figure 2.3), showing cross stratified sand and a bed where multiple cobble samples were discovered. The shovel for scale is approximately 1 m tall. Samples were collected approximately 30-90 cm horizontally into the colluvium (Table 2.1).

Table 2.1. List and description of samples collected during the 2017 field expedition to Prince Patrick Island, including lab ID, collection depth, and additional information about the sample. Bolded samples indicate they were cleaned and sent for cosmogenic nuclide measurements by the AMS at Lawrence Livermore National Lab. All samples listed were collected from section D8, with the exception of two modern stream samples (022,023), which were collected in proximity to base camp.

Field ID	Lab ID	Sample Type	Clast Lithology	Sedimentology of enclosing bed	Depth Collected below datum (m)	Depth collected below colluvial surface of section (cm)	Additional Notes
001	3531	Cobble	Meta arenite (fs-ms)	Tabular cross bedded sand	23.5	45	8 cm diameter
002	3532	Cobble	Meta arenite (fs)	Tabular cross bedded sand	23.5	45	20 cm diameter
003	3533	Cobble	Meta arenite (fs)	Tabular cross bedded sand	23.7	50	10 cm diameter, some calcite cement (weak, vesicles)
004	3534	Cobble	Meta arenite (fs)	Tabular cross bedded sand	24.1	50	8 cm diameter
005	3535	Cobble	Meta arenite	Tabular cross bedded sand	24.5	50	Shallow depth below scarp surface
006	3536	Sand	Quartz rich sand	Tabular cross bedded sand	23.5	7.5	
007	3537	Cobble	Meta arenite	Tabular cross bedded sand	23.5	50	
008	3914	Cobble	Meta arenite (vfs)	Tabular cross bedded sand	23.5	90	Poor lithology

Field ID	Lab ID	Sample Type	Clast Lithology	Sedimentology of enclosing bed	Depth Collected below datum (m)	Depth collected below colluvial surface of section (cm)	Additional Notes
009	3538	Cobble	Quartz arenite	Tabular cross bedded sand	23.5	90	
110	3539	Cobble	Quartz arenite	Tabular cross bedded sand	23.5	90	
011	3540	Cobble	Quartz arenite (fs)	Tabular cross bedded sand	23.5	70	Small mass (<50g)
012	3541	Cobble	Quartz arenite (fs-ms)	Tabular cross bedded sand	23.5	70	Small mass (<50g)
013	3542	Cobble	Arkose (ms)	Tabular cross bedded sand	23.5	70	Small mass (<50g)
014	3543	Cobble	Quartz arenite (Fs-ms)	Planar cross bedded sand	33.1	30	May not be in place
015	3544	Cobble	Quartz arenite (ms)	Planar cross bedded sand	33.1	55	Very recrystallized
016	3545	Sand	Sand (m-c)	Massive woody detritus layer	35.2	<30	Permafrost only 30 cm horizontal distance
017	3546	Sand	Sand (m-c)	Massive woody detritus layer	33.1	<30	
018	3547	Sand	Sand (f-m)	Tabular cross bedded sand	24	20	Sampled below middle of 25 cm peat

Field ID	Lab ID	Sample Type	Clast Lithology	Sedimentology of enclosing bed	Depth Collected below datum (m)	Depth collected below colluvial surface of section (cm)	Additional Notes
019	3548	Sand	Sand (m-c)	Tabular cross bedded sand	13	20	Sampled in red beds
020	3549	Cobble	Quartz arenite	Tabular cross bedded sand	17.3	40	
022	3550	Sand (Modern)	Sand (m-c)	Modern Stream	0	0	15 m asl
023	3551	Sand (Modern)	Sand (m-c)	Modern Stream	0	0	16 m asl

2.4.4 Geochronology Lab Methods

2.4.4.1 Quartz Purification

A series of purification procedures is necessary to reduce a sample collected in the field (cobble or amalgamated sand) to a pure quartz fraction and significantly reduce, as much as possible (<30 ppm), the amount of other minerals containing unwanted ^{27}Al .

Physical and chemical preparation of samples was performed at the Cosmic Ray Isotope Sciences at Dalhousie (CRISDaI) Lab. The sand samples were sieved to grain size fractions between 150 and 500 μm . The cobble samples were brushed and, if necessary, rinsed in water or dilute HCl to remove any mud or carbonate cement. They were broken with a cleaned sledgehammer before crushing in a Braun Chipmunk Jaw Crusher. A small fragment was kept for archival purposes unless the quartz content in the cobble was very small. The crushed material was then cycled through a BICO disc pulverizer and sieved until everything passed through a 500 μm screen. Quartz was concentrated in weighed 150-250 μm and 250-355 μm fractions of the sand and crushed cobbles. After the crushing and sieving process, the subsequent cleaning procedure begins with a rare earth magnetic removal of ferromagnetic grains, acid pretreatment in boiling aqua regia (HNO_3+HCl) for 2 hours, froth floatation after a short HF etching, and Frantz magnetic separation, and partial acid digestions by HF/ HNO_3 in an ultrasonic tank at sub-boiling temperatures. Optical tests were conducted throughout the process. Samples that did not appear to be pure quartz, mainly owing to the presence of feldspars, were subject to at least three weeks in a hexafluorosilicic acid bath chamber, rotated continuously on hotdog rollers or at rest in a fumehood with daily shaking. As the samples became optically pure, they were analyzed by ICP-OES for major element contents of Al, Be, Fe, Ti, Na, K, Mg, and Ca, as these need to be removed during target preparation. Using the ICP-OES results as a guide, additional mineral and chemical separations were conducted until the sample had plateaued at its native ^{27}Al concentration (as determined by consecutive ICP-OES tests). This enabled the $^{26}\text{Al}/^{27}\text{Al}$ to be as high as possible, closer in magnitude to the $^{26}\text{Al}/^{27}\text{Al}$ of the AMS standard. Ideal sample targets would have <30 $\mu\text{g/g}$ Al, but final quartz Al concentrations ranged from 43.3 to 112.7 $\mu\text{g/g}$. The high Al sample only had 25.2 g of quartz remaining and therefore could not

undergo further pretreatments and still preserve sufficient mass of ^{26}Al needed in the target. Next, meteoric ^{10}Be was removed from samples in a triplicate sequence of partial HF digestions similar to Merchel et al. (2019) after Kohl and Nishiizumi (1992). Samples were dried, placed in a desiccator, massed into a Teflon digestion vessel, and 222 μg of Be was added with Be carrier “PRIME Lab 2020 Carrier Bottle 5-1046 $\mu\text{g}/\text{ml}$ Be” purchased from PRIME Lab in August 2020. The quartz samples were digested with a cocktail of HF, HClO_4 , HNO_3 , and HCl; amounts were adjusted according to quartz mass and major element chemistry. The final dry-down precipitate was dissolved, transferred, and brought up to 100 ml, and then a 5 g aliquot was collected for verification of Al content by ICP-OES to determine the amount of Al carrier needed to be added, if any. After the addition of Al carrier (Alfa Aesar 1000 $\mu\text{g}/\text{ml}$ Al ICP-MS standard), a second 5 g aliquot was collected for verification of the quartz plus carrier total Al mass by ICP-OES.

2.4.4.2 Column Chemistry Improvements

A significant challenge was extracting Be and Al with high efficiency (>98% recovery) and removing unwanted elements that may cause difficulties during the target chemistry, isobaric interferences, or reduction of Cs-sputtering in the source during AMS. Therefore, in 2019, multiple elution experiments were conducted using varying column heights (5ml versus 10 ml) to isolate exactly when Be and Al were eluted during the ion exchange chromatography stage, compared to other undesirable elements such as K, Ca, and Mg. Samples were collected at 1 ml intervals and measured independently using ICP-OES. These experiments were run to improve the amount of Al and Be collected from the column chemistry and ensure high atom counts during the AMS run.

2.4.4.3 Column Chemistry and Target Prep

Samples were subjected to anion column chemistry over 5 ml resin, then a pH-controlled precipitation as modified by this study to improve the reduction of Ca and Mg from the Al target. Following the cation column chemistry over 5 ml resins, the solutions were precipitated with ultrapure ammonia gas, and the hydroxides were converted to oxides by heating in boron-free quartz vials with a Bunsen burner at $>1000^\circ\text{C}$ for three minutes for BeO and five minutes for Al_2O_3 .

To measure the $^{10}\text{Be}/^{26}\text{Al}$ in the quartz samples, targets of BeO and Al_2O_3 were prepared for analysis of $^{10}\text{Be}/^9\text{Be}$ and $^{26}\text{Al}/^{27}\text{Al}$. The dried BeO and Al_2O_3 were crushed, mixed 1:1 [by volume] with niobium powder, and packed into stainless steel cathodes for AMS measurement at the Center for Accelerator Mass Spectrometry, Lawrence Livermore National Lab (CAMS-LLNL). The AMS signal is measured on an ion current in units of microAmps (μA). Paired ^{10}Be and ^{26}Al concentrations were measured for 7 of the 21 samples. Measurements of $^{10}\text{Be}/^9\text{Be}$ and $^{26}\text{Al}/^{27}\text{Al}$ were made against standards of known ratios (07KNSTD3110, $^{10}\text{Be}/^9\text{Be} = 2.850 \times 10^{-12}$ (Nishiizumi et al. 2007); KNSTD30960, $^{26}\text{Al}/^{27}\text{Al} = 3.096 \times 10^{-11}$), and separate process blanks were analyzed to subtract background concentrations for each isotope. The 1σ AMS precision (maximum of either Poisson counting statistics or the variation about the mean ratios obtained over at least three measurement intervals) on the ^{10}Be and ^{26}Al sample targets averaged $3.1 \pm 1.1\%$ for Be and $29 \pm 18\%$ for Al. The Al measurements were less precise than the Be measurements, partly because of the low abundance of ^{26}Al ($^{26}\text{Al}/^{27}\text{Al}$ averaged 1.1×10^{-15} on the buried samples). The ^{10}Be and ^{26}Al blank subtractions averaged 4.4% and 21% of the measured samples, respectively. The relatively imprecise AMS analysis of ^{26}Al therefore, contributes significant uncertainty to the final age. We also measured the $^{10}\text{Be}/^9\text{Be}$ in the ^{26}Al process blank (with ^{10}Be carrier added) to make sure the Al carrier did not contribute ^{10}Be . The ^{10}Be in the Al process blank was less than the ^{10}Be in the Be process blank (Be carrier was added to both), indicating no significant additional ^{10}Be was added in samples with Al carrier.

2.4.4.4 Data Reduction

The ^{10}Be and ^{26}Al concentrations are calculated from the $^{10}\text{Be}/^9\text{Be}$ and $^{26}\text{Al}/^{27}\text{Al}$ ratios measured by the AMS. Process blanks analyzed by the AMS are used to subtract any background concentration in ^{10}Be and ^{26}Al . The site-specific production rate is calculated by the addition of different production mechanism pathways for each nuclide (e.g., production from neutrons, muons) and scaled based on the latitude, longitude, elevation, topographic shielding, surface coverage, and sample thickness (Lifton et al. 2014) (for additional details, see Gosse and Philips 2001). Simple burial ages are then calculated as the $^{26}\text{Al}/^{10}\text{Be}$ ratio over time is known, using equations by Nishiizumi et al. (1991). Isochron burial ages are calculated based on the slope of the isochron (Balco and

Rovey 2008). The slope is calculated based on the $^{26}\text{Al}/^{10}\text{Be}$ ratio; because ^{26}Al decays faster than ^{10}Be with time, the slope is proportional to burial duration. We use the production rate calculations by Balco et al. (2009) for a surface rate (at ~400 m) but assume a longer-term average rate scaled from sea level using Lal (1991) as modified by Stone (2000).

2.4.5 Simple Burial and Isochron Dating Methodology

The time that a sample was buried after a prolonged exposure period is referred to as a burial duration. If the sample remained buried until it was sampled, then that duration can be interpreted as a burial age. In the case of sediment in thick stratigraphy, the burial age reflects the time of deposition, unless burial was delayed.

A simple burial age is interpreted in $^{26}\text{Al}/^{10}\text{Be}$ vs. log normalized ^{10}Be space, which tracks how the isotopic ratio of two cosmogenic nuclides with different production rates and decay rates changes over time, using the concentration of ^{10}Be as a surrogate for time. To obtain a simple burial age in a stratigraphic section, we sample about >0.5 kg of quartz-rich coarse to medium sand (1-0.25 mm) to eventually obtain >25 g of pure quartz. The method requires that the ^{10}Be and ^{26}Al in quartz were produced in the catchment before or during transportation to the final depositional site (where it is sampled). The ratio of $^{26}\text{Al}/^{10}\text{Be}$ produced through spallation in the upper few meters of Earth's surface was until recently considered to be 6.75 (atom/atom) based on empirical measurements and modeling. However, this value is being challenged with a better understanding of the altitudinal and latitudinal controls on the spallation interactions, and a growing number of measurements indicate that the ratios are higher (up to 7.3 atom/atom; Corbett et al. 2017). This thesis uses the previously accepted value of 6.75, however, a complete sensitivity analysis is required to evaluate the systematic error in age (which is non-linear). This approach is referred to as 'simple' burial dating because it requires an assumption that the quartz has never previously been buried so that the initial depositional ratio was 6.75, and that ratio will decrease with time because ^{26}Al ($t_{1/2} = 0.70$ Ma, Nishiizumi 2004) decays faster than ^{10}Be ($t_{1/2} = 1.387$ Ma, Korschinek et al. 2010). A simple burial age can be computed from $^{26}\text{Al}/^{10}\text{Be}$ in a single sample, but usually, multiple samples are used to improve precision. However, if multiple burial histories

occurred prior to the final deposition, the measured ratio would reflect the total burial history, and significantly overestimate the last burial event's duration. Additionally, if the buried quartz was exposed after burial, the low ratio representing the burial duration would increase toward the production ratio, usually causing an underestimate of the age. In instances where the TCN concentrations in the transported quartz were low owing to a high paleo-catchment erosion rate, and where the burial duration was sufficiently long to reduce the concentration to kilatoms/g further, then production by muonic interactions may be a factor. Because it appears that ^{26}Al may be produced at a faster rate by muons than ^{10}Be compared to fast nucleons, this would cause the ratio of $^{26}\text{Al}/^{10}\text{Be}$ to increase during burial time, causing an underestimate of the burial duration.

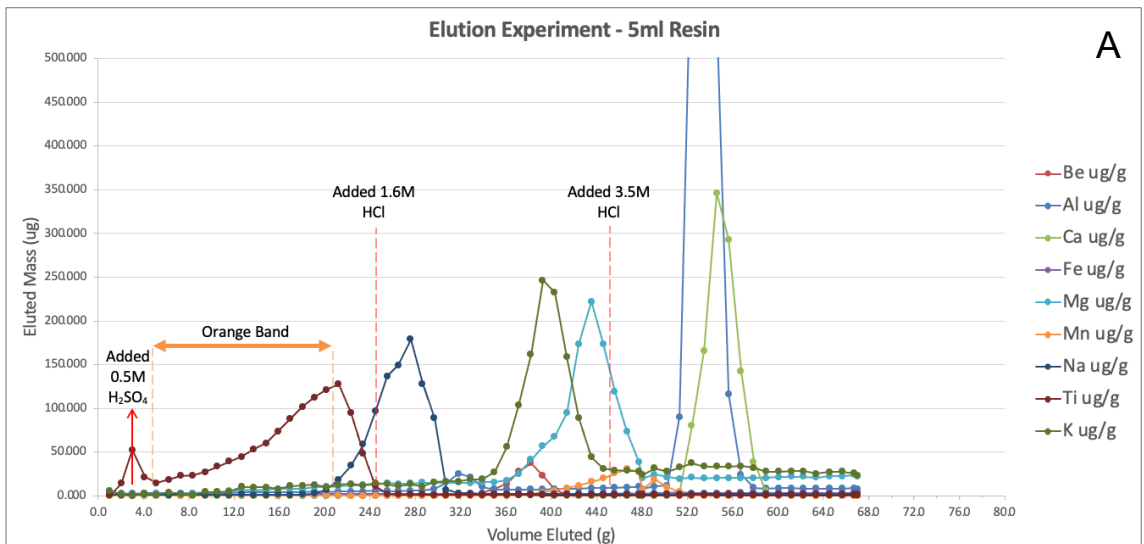
To prevent these issues with the 'simple' burial dating approach, one can use the isochron burial dating approach using the same isotopes. Unlike with simple burial dating, samples can undergo varied multi-stage exposure histories resulting in quartz grains with varying initial concentrations, as the clasts likely originated from different parts of the catchment area before being buried simultaneously. Since all the clasts came from the same catchment, they should have the same initial $^{26}\text{Al}/^{10}\text{Be}$ ratio of 6.75, and it is assumed that they were all buried for the same amount of time and experienced the same amount of decay (Balco and Rovey 2008). These samples are then plotted on an isochron plot of ^{26}Al vs. ^{10}Be concentrations (atoms g^{-1}). The ^{26}Al and ^{10}Be concentrations range between the cobble samples due to their varied exposure history in the catchment, and therefore, this range in concentrations will define a line on the isochron plot (Granger and Muzikar 2001). The premise is that the slope (~ 6.75) on an ^{26}Al vs ^{10}Be isochron plot will decrease after the exposure is interrupted by a shielding event. As time after burial progresses, the slope of the line will become less steep and tilt downward due to preferential nuclide decay (^{26}Al decays faster than ^{10}Be), producing the final isochron. By measuring the slope of the line, we may define an age of burial. The uniqueness of the isochron burial dating method, and the benefit of this approach versus the 'simple' burial dating method, is that one may test for post-depositional production. If there is no spallogenic production post-burial, the isochron passes through the origin. In the presence of post-burial production and accumulation, the isochron will shift upwards and no longer crosses the origin. The y-intercept represents the excess of ^{26}Al due to post-

burial production (Balco and Rovey 2008), and can alert to the presence of this within a sample.

2.5 Results & Interpretation

2.5.1 Improvements to experimental design

Due to the previous challenges of extracting Be and Al with high (>98%) efficiency, multiple experiments were conducted to improve Be and Al recovery. These experiments resulted in a better understanding of when these elements were expelled from the column when a range of elemental analytes was present in a sample. These experiments allowed improved isolation and extraction of Be and Al, providing higher efficiencies of each element in the final AMS target, more effective removal of isobars ^{26}Mg and ^{10}B , and stronger currents during AMS. Figure 2.5 illustrates the final and most successful elution experiment, which was achieved using a 5 ml column and isolates Be from Mn, Ti, Na, and Al.



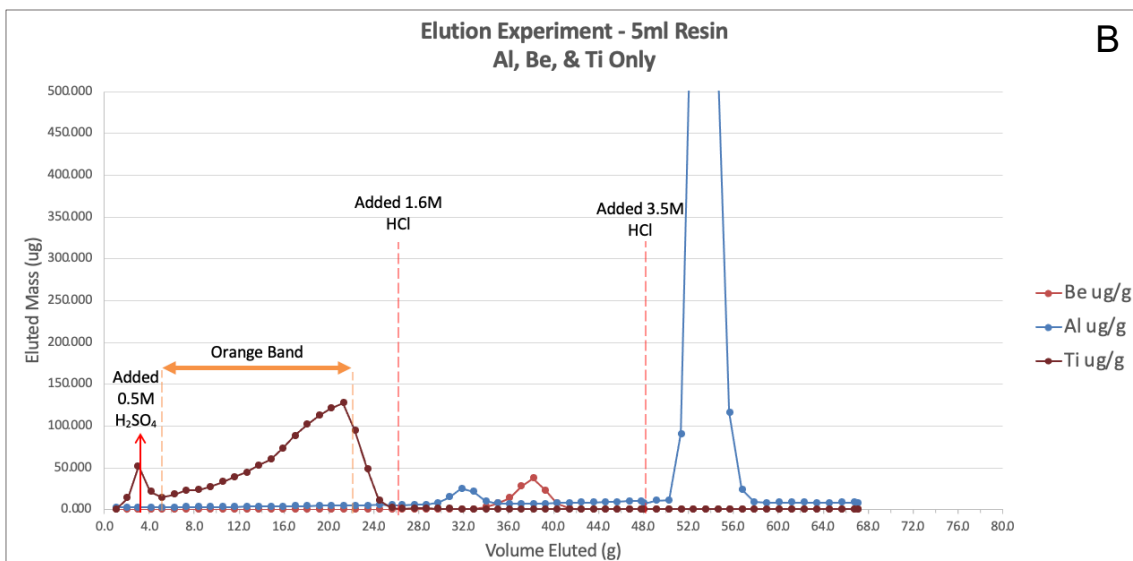


Figure 2.5. A: Experimental elution curves for a range of elements (Be, Al, Ca, Fe, Mg, Mn, Na, Ti, and K), eluted within a 5 ml column, ultimately used for the final column chemistry. Different HCl and H₂SO₄ concentrations were added at different intervals, as indicated by the dashed lines and red arrow. The ‘orange band’ illustrates the time span when Fe and Ti are being eluted from the column, which can be observed via an orange band moving down the column. B: Enlarged version of Figure 2.5A, showing just Be, Al and Ti, to emphasize the key elements of interest better.

A secondary improvement to the former standard operating procedure was raising the calcining time of BeO and Al₂O₃ to three minutes and five minutes, respectively, which resulted in increased AMS currents. The samples averaged 1.01 μA (the pure AMS standards yielded 1.3 μA), exceeding the 0.8 μA average obtained for other samples analyzed during the same AMS run that were only calcined for a little more than three minutes, which was the previous protocol. This improvement may be related to water molecules that affect the sputtering process in the source and has motivated the CRISDal Lab to calcine all future Al₂O₃ targets in a 950°C furnace for at least 4 hrs as had been standard operating procedure until 2012 when it was switched to the Bunsen burner method.

2.5.2 Stratigraphy and Sedimentology

The objective of the sedimentology analysis in the field was to provide context for the TCN burial chronology during sample collection and provide additional paleoflow

and provenance constraints for sediment in the BFM near the type locality. Detailed stratigraphic logs describing sections D8 and S1 (Figure 2.6) are based on field measurements after removing colluvial cover, which averaged 20-30 cm (permafrost was typically encountered at 30 cm depth horizontal into the face, but depths up to 90 cm were also observed).

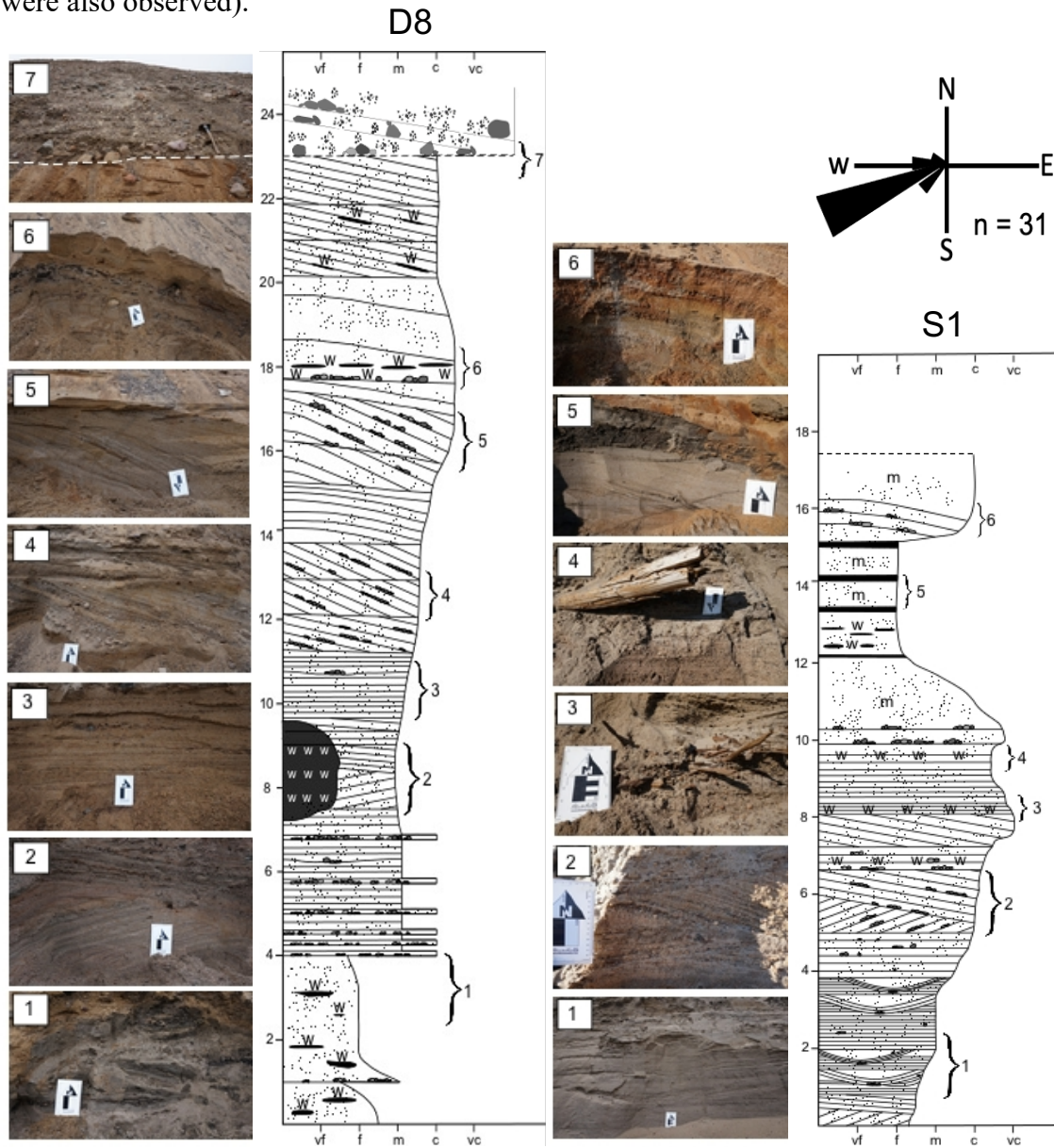


Figure 2.6. Two stratigraphic columns (left D8 and right S1) recorded from BFM exposures on Prince Patrick Island. The left column was previously identified by Devaney (1991) as “Section 8”. Images of key features (planer beds, tabular cross-beds, trough cross-beds, woody debris (‘w’ symbol), and contacts) are shown to the left of their respective columns with numbers corresponding to their location. The prominent black feature illustrated from 7 m to 9.5 m on

section D8 illustrates an extensive peat present within the section. The white ruler card used in photographs is 15 cm in length. A rose diagram of paleoflow directions is illustrated in figure's top right, displaying major trends in flow towards the WSW. Thirty-one individual values were measured from imbrication, trough cross-beds, and planar cross-beds.

2.5.2.1 Section D8

The orientation perpendicular from the face of section D8 was 350-355° with a base elevation of 52 m asl. The section's total height, measured with the laser range finder, was 35.7 m, measured to the base of a large boulder at the top of the section. Section D8 had a general coarsening upwards sequence. The base of section D8 is composed of white silt and fine to medium-grained sand layers interbedded with multiple 150 cm thick, laterally extensive lenses of peat that were finely stratified and interbedded with 5-10 cm long twigs (Figure 2.6, Photo D8-1). At approximately 4 m, the sequence changed to beds of very coarse to medium, horizontal parallel laminated sand, with 10-20 mm bed thicknesses. Pebble clasts were infrequently intercalated at the base of beds (Figure 2.6, Photo D8-3). Approximately 7-10 m up section, the sequence fined into medium to coarse-grained cross-bedded sand. This is the dominant facies for much of the BFM sections inspected. Most of the cross-sets were large, 30-50 cm thick, well-sorted, and internally fining upwards. The steepest dipping cross bed was 26°. Co-sets were upwards of 1 m thick (Figure 2.6, Photo D8-4). Additionally, at approximately 7-9 m up section, we observed a large peat bed, which was laterally extensive over the left half the section. The peat layer included black and brown mud beds 1-10 cm thick, with crudely layered wood fragments. Larger logs (none observed rooted in growth position) were present within this peat layer and abundant finer detritus. This peat section was scoured for bone fragments, but none were found. Above this section, large sets of cross-bedded sand were observed, with large pebbles at the base fining upwards to medium sand. This pattern continued up section, with gradually coarser beds and larger intercalated pebbles at the base of beds. Many woody detritus lenses and black-green mud could also be observed intermittently between cross-beds (Figure 2.6, Photo D8-6). At 19 m up-section, the sand changed in colour from gold to red.

At approximately 23 m up section, a sharp unconformity was observed, highlighted by the distinct difference between the dominant medium to coarse sandy facies below and a grey gravel facies above (Figure 2.6, Photo D8-7 and enlarged in Figure 2.7). The contact was distinct, flat over >10 m, and there was no discoloration of the beds below the unconformity. There was no evidence of shearing, thrusting, or dewatering structures through the contact, which one might expect if the section had been overrun by ice. The facies above the unconformity was a poorly sorted, polymictic gravel with crude trough cross-bedding (Figure 2.7). Despite having several boulder-sized clasts in the colluvium on the hillslope (about 12, largest ~70 cm diameter) and one boulder at the top of the ridge, the colluvium contained many cobbles that averaged around ~25 cm diameter and not many large boulders. A pebble lithology count is recorded in Appendix B, Table B.1. No striations were observed on the clasts directly above the unconformity, however, they were observed approximately 1 m above the contact and increased in frequency further from the contact. At 35 m from the base of D8, >5% of the clasts were striated.





Figure 2.7. Distinctly different gravel facies observed above unconformity at 23 m up-section D8. The upper photo shows an enlarged version of Figure 2.6 Photo D8-7, which depicts the unconformity between the lower sandy facies of the Bfm and the upper Quaternary glaciofluvial outwash. The lower photo shows the coarse fluvial facies up close, illustrating its poorly sorted nature. The shovel is approximately 80 cm, while the white scale card is 15 cm.

2.5.2.2 Section S1

Section S1 (Figure 2.6, right) did not have as clean a face as D8 and had more slumping. There was a more considerable amount of woody detrital beds present in this section. The face's orientation was $\sim 330^\circ$, and the elevation at the base of the section was 51 m asl. The section's total height measured with the laser range finder, was approximately 16.6, measured to a boulder at the top of the section. The section also exhibited a general coarsening upwards trend. The base of the section was very fine to fine silt, with trough cross-bedding and planar cross-bedding. These were the only trough cross-bedding facies observed within section S1 or D8. The trough cross-beds were large, with cosets about 70-90 cm across and 30 cm in height (Figure 2.6, Photo S1-1). Coarser-grained lag deposits were observed at the base of the troughs. Above this section, planar cross-bedding (beds were 5-10 mm thick) was observed with small pebbles occurring at the base of beds and internally fining upwards. Approximately 5-8 m up section, several large cross stratified beds were observed, with multiple coarse pebble layers and muddy lenses interbedded within the cross-sets. Cross-set height was 0.5-1 m and dipping approximately 30° (Figure 2.6, Photo S1-2.) At 8-10 m up section, the beds become

coarser, with some having large woody debris and 3-6 cm pebbles intercalated within them. The woody debris ranged in size from small 1-5 cm long twigs (Figure 2.6, Photo S1-3) up to logs greater than 2 m long (an example is shown protruding from a layer in Figure 2.6, Photo S1-4). These heavy detritus layers had little to no matrix of sand or silt and were more indurated, forming dark, slightly protruding beds. A finer grained section was observed at 12-15 m up section, with 5-10 cm green-black mud and white silt layers. Fine laminations and ripples (<15 mm) were observed within these beds. Above this section, the sand beds had a distinct red mottled colouring, similar to beds observed near the top of section D8. White vertical features that cut bedding are observed, which could be interpreted as ice wedge or sand wedge pseudomorphs (Figure 2.8). The top of section S1 was capped by woody debris and detritus. The distinct gravel facies capping the top of section D8 was not observed capping section S1.



Figure 2.8. Potential sand wedge pseudomorphs observed at the top of section S1. The white scale bar is 15cm tall.

2.5.2.3 Paleoflow Analysis

Thirty-one paleoflow indicators were analyzed at sections D8 and S1 which included the axes of channel troughs, trough cross beds, and the imbrication of small clasts. To correct for polar magnetic issues with the compass, a GPS was used, and we walked along a bearing to determine the orientation of the face. These measurements did not include the section above the unconformity at D8. The paleoflow measurements were highly congruent, indicating a dominant flow towards the WSW (220° - 240° , Figure 2.6). The paleoflow evidence suggests the braided fluvial streams, from which the BFM was deposited, were not flowing towards a contemporaneous valley to the North and

suggests there may not have been a large depression at the location of M'Clure Strait that would divert paleoflow towards it.

For the upper grey gravel section above the unconformity (Figure 2.7), the flow is less well constrained. At the base of the gravels, in proximity to the unconformity, in situ cobble imbrication directions measured 040-220°. However, a few meters above these measurements, crude cross-bedding indicated directions were 210-30°. The upper gravels may have, on average, a dominant paleoflow direction towards the NE.

2.5.2.4 Depositional Environment Interpretation

The dominant medium to very coarse sandy cross-bedded facies (Figure 2.6, Photo D8-5 and Photo S1-2) observed within the BFm have been interpreted as facies code Sp (Miall 1977) and are attributed to linguoid, transverse bars. The less dominant silty trough cross-bedded facies observed within section B (Figure 2.6, Photo S1-1) have been interpreted as facies code St (Miall 1977), lower flow regime dunes. The coarse sandy horizontal bedding observed has been interpreted as facies code Sh attributed to planar bed flow. The minor occurrences of organic-rich silt and mud facies have been interpreted as facies code Fl and Fm, which are attributed to overbank deposits. The collection of facies codes St, Sp, Sh, Fl, and Fm observed within the two sections of the BFm can be interpreted as a sandy braided river paleoenvironment, with proximal forests that could be the source of large logs and woody debris. This paleoenvironment interpretation is consistent with previous interpretations of the BFm by Fyles (1990) and Devaney (1991). The extensive peat layer observed in D8 could be a lower energy environment such as an overflow deposit or an oxbow lake that lies adjacent to a high energy portion of the river forming the transverse bars. There is an overall coarsening upward trend within the sequences, with minor 1-2 m fining upward trends. The coarsening upward trend may indicate that the 23 m of exposed sediment represents a fluvial depositional environment that increases in energy with time, allowing for the transportation of larger sediment loads and grain sizes. The total time represented in a 24 m channel sequence like this is on the order of 10^4 - 10^5 years (Miall 1992) and may represent one or more precession cycles (Berger 1988). However, the absence of disconformities within the main sections indicates a continuous aggrading profile,

unaltered by base level changes brought about by uplift or faulting or the formation of regional troughs (i.e., M'Clure Strait). This conclusion is supported by no major deflection in paleoflow towards M'Clure Strait during this period of deposition of the BFm.

The facies above the unconformity at section D8 corresponds to the Gms facies code (Miall 1977). Observations of striae or faceting on the gravels were observed 1 m above the unconformity and above, but while till at the very top (upper 40 cm) cannot be ruled out, it is more likely that the massive gravel is simply cryoturbated. This lack of a convincing till suggests that if the site had been glaciated, then it was most likely covered by cold-based ice, or associated sediments deposited atop this section have since been eroded. The top of the section (at the summit) is a narrow ridge, formed as an interfluvium, and therefore, significant erosion is likely.

We have interpreted this section as glaciofluvial outwash, which proximal glaciers may have deposited during the Quaternary. There are a few observations that support this conclusion. The deep reddening of the beds near the top of the section could suggest oxidization, potentially from a paleosol, which indicates a significant period of time may have occurred at the boundary between the lower sandy facies and the colluvium above. Most cobbles below the unconformity are quartz arenite samples, whilst above the cobble lithologies are much more varied (Table B.1). This contrast in pebble lithology between the two units also supports a significant time difference may have occurred. Finally, a significant difference in paleoflow ($040\text{-}220^\circ$ in the upper gravel facies versus $220\text{-}240^\circ$ in the lower section) supports the hypothesis that these units were deposited at different times.

2.5.3 Simple Burial and Isochron Ages

Although the general purpose of the geochronology investigations is to provide a numerical age with uncertainty for sediments proximal to the BFm type locality, the specific objective in using the TCN burial method is to calculate the duration of time the analyzed quartz has been buried, and by making assumptions about the burial history, interpret that age as the time of deposition. Burial potentially records additional sediment, glacial ice, lake water, vegetation, ash, or snow that may have covered the sediment. It is

challenging to know the depth of burial over time. Therefore, samples were collected deep (>30 cm) in the sediments so that it can be assumed that the samples were not affected by post-burial production by muons. The cobble-isochron method compensates for post-burial production by interpreting any positive intercept on the y-axis (^{26}Al concentration) caused by an offset of similar post-burial exposure to all samples. When samples are derived from different depths, or have low depositional abundances, the isochron compensation for post-burial exposure is difficult to validate.

Seven samples were analyzed for ^{26}Al and ^{10}Be concentrations, which included five cobble samples and two sand samples. A complete record of the geochemical and AMS data is provided in Appendix B. The sample ID, ^{10}Be and ^{26}Al concentrations, and the $^{10}\text{Be}/^{26}\text{Al}$ ratios are presented in Table 2.2. A Matlab code (Hidy et al. 2010) is used to compute a simple burial age. Spallogenic production, muon production, and scaling are based on Lifton et al. (2014), both during the buildup and the burial periods.

Table 2.2. TCN measurements for cobble and sand samples from Prince Patrick Island, NWT. Depths are measured from the top of the section, 35.7 m tall (Figure 2.6, D8). For details on the location, clast thicknesses, and chemistry/AMS data, see Appendix A, C. Sample numbers are abbreviations of sample ID PPI-17-10X-00X, where 00X is the sample number in the table. Uncertainty is the total analytical error (1σ) based on all internal error sources added in quadrature. All samples and the two process blanks were normalized with AMS standard KNSTD3110, and $^{10}\text{Be}/^9\text{Be}$ ratios were calculated using a ^{10}Be half-life of 1.387 Ma.

Sample ID	^{10}Be Concentration.		^{26}Al Concentration		$^{26}\text{Al}/^{10}\text{Be}$	
	Measurement	Uncertainty (1σ)	Measurement	Uncertainty (1σ)	Measurement	Uncertainty (1σ)
	$\times 10^4 \text{ atoms g}^{-1}$	$\times 10^2 \text{ atoms g}^{-1}$	atoms g^{-1}	atoms g^{-1}	atoms/atoms	atoms/atoms
001	2.942	8.180	15880	3404	0.540	0.22
003	0.8185	5.814	16256	3305	1.986	0.22
006	4.059	13.14	18843	3217	0.464	0.17
007	1.042	4.547	5916	2184	0.568	0.37
008	0.6672	3.713	9217	2645	1.381	0.29
017	2.184	7.803	28423	4781	1.301	0.17
020	0.5845	3.235	15342	4292	2.625	0.29

2.5.3.1 $^{26}\text{Al}/^{10}\text{Be}$ vs ^{10}Be simple burial age results

Two sand samples were used to calculate a simple burial age and yielded a weighted mean of 3.43 Ma ($+0.477/-0.300$) [PPI-17-105-017] and 5.63 Ma ($+0.467/-0.303$) [PPI-17-103-006] (Table 2.3, Figure 2.9). However, counterintuitively, the shallower sample [PPI-17-103-006] (buried at 23.5 m) has a lower $^{26}\text{Al}/^{10}\text{Be}$ ratio (Table 2.2) and an older burial age than the deeper sample [PPI-17-105-017] (buried at 33m, 9.5 m below the shallower sample), violating the law of superposition.

Table 2.3. Simple burial ages (Ma) for the sand samples. Sample number, type, and sample depth, along with the positive and negative 1σ errors, are provided.

Sample	Sample Type	Depth m	Simple Burial Age Ma	Age Pos. Error (1σ) Ma	Age Neg. Error (1σ) Ma
PPI-17-103-006	Sand	23.5	5.63	0.467	0.303
PPI-17-105-017	Sand	33.1	3.43	0.477	0.300

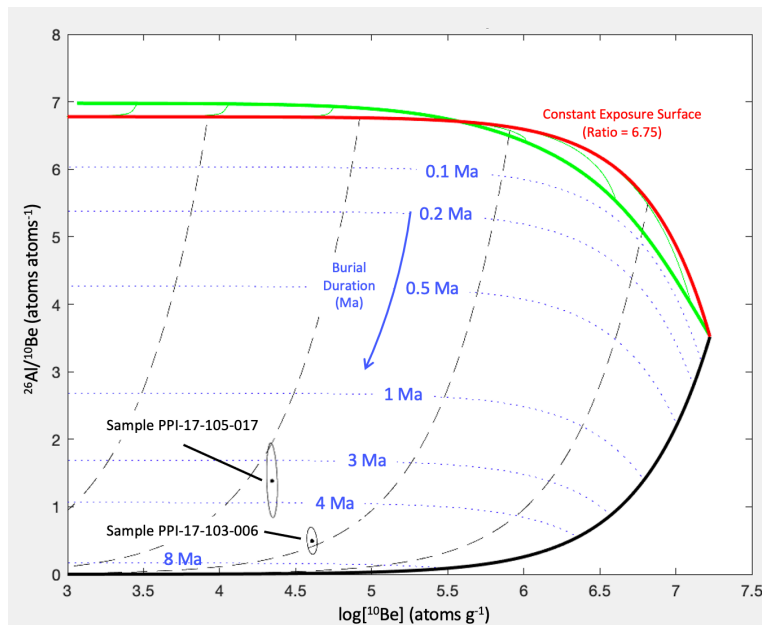


Figure 2.9. Simple burial plot of $^{26}\text{Al}/^{10}\text{Be}$ (atoms atoms $^{-1}$) versus normalized ^{10}Be concentration (atoms g $^{-1}$) showing the burial ages of sand samples PPI-17-105-017 and PPI-17-103-006. The

error is illustrated by 1σ ellipses. The solid red line represents the continuous exposure surface with no surface erosion; the solid green line represents contours of the continuous exposure curve at successively increasing surface erosion rates. Samples will plot somewhere between these two lines prior to burial. Once buried, samples follow a path parallel to the dashed black lines. Dashed blue lines represent burial ages. Sample depths are assumed to be constant (i.e., not multiple exhumations and reburial events) with time and assuming post-depositional muon production based on modern sample depths. The measured ratios could represent a simple burial event, multiple events, or a single event with long exposure. Simple burial dating cannot distinguish between these scenarios.

The interpretation of ^{26}Al and ^{10}Be concentrations in a given sample is tied to the assumptions of exposure and burial history of that sample. These assumptions dictate the duration of decay of the deposited TCN concentration and the amount of in-situ TCN production after burial. Therefore, several scenarios regarding the timing of TCN production and the exposure and burial histories are presented and examined. Scenario 1 assumes that rapid transport, deposition, and an instantaneous and complete burial period, all occurred and the simple burial ages (Table 2.3) are the depositional ages of the sediment. However, assuming no error in chemistry, ICP-OES, or AMS measurement, a stratigraphic reversal in the ages still exists (a sample with a burial duration of 5.63 Myr lies stratigraphically above sediment with a burial duration of 3.43 Myr). This implies a violation in the exposure or burial history of one or both of the samples. One possibility is that the inverted ages are caused by a glacitectonic process that placed older sediment on younger, sometime after they were deposited. There is ample evidence of glacitectonic deformation on Banks Island (Evans et al. 2014, Vaughan et al. 2014). However, unlike at the Duck Hawk Bluffs or Worth Point sections, there was no deformation observed in D8 on Prince Patrick Island, nor that has been recognized by previous researchers (Devaney 1991, Fyles et al. 1994) and no apparent disconformity between the two samples (Figure 2.6).

Scenario 2 is that the age disparity is caused by differences in the $^{26}\text{Al}/^{10}\text{Be}$ between the two samples at the time of deposition. This scenario would violate the simple burial dating assumption of constant inherited concentrations and a $^{26}\text{Al}/^{10}\text{Be}$ ratio of 6.75 before burial (Granger and Muzikar 2001, Gosse and Phillips 2001). If the initial

$^{26}\text{Al}/^{10}\text{Be}$ ratio was lower than 6.75, perhaps due to millions of years of burial prior to final deposition, the simple burial age would be overestimated. Alternatively, the lower concentrations could be caused by an increase in the catchment's erosion rate, for example, which would not allow quartz grains to be exposed for a long enough duration to reach an initial 6.75 ratio. However, this scenario is also unlikely. While short periods of burial on the order of 10^3 to 10^4 years can be expected on broad coastal plains (e.g., the Gulf of Mexico coast; Hidy et al. 2013), the burial is often shallow and ineffective at substantially reducing the $^{26}\text{Al}/^{10}\text{Be}$ by the magnitude observed. Burial for >0.6 Myr before final deposition would be required, which is more likely in tectonic basins with substantial relief for accommodation but a short lifetime (e.g., in an accretionary prism or foreland wedgetop basin). While we cannot preclude the combinations of short-term sedimentary burial combined with periods of glacier ice cover during the Miocene and Pliocene, such as the 3.3 Ma M2 glaciation, it seems difficult to explain why the upper sample would have experienced these events whereas the lower sample did not, in the same stratigraphic section separated only by 9.5 m. On the other hand, one piece of evidence that supports this scenario is that the burial age of the lower sample is 3.43 Ma ($+0.477/-0.300$) which coincides with the M2 glaciation.

Scenario 3 considers that there was incomplete shielding at the site after burial, which could affect the post burial ratio of the TCN within quartz. This scenario could occur due to syn-burial production (production of TCN's during slow aggradation of the Bfm stream beds), erosion of the river-cut section somehow exposing the deeper of the two samples more, or post-burial production from muons favoring a higher $^{26}\text{Al}/^{10}\text{Be}$ in the deeper sample (Balco and Rovey 2008, Granger et al. 2013). Although it is possible that a significant fraction of the ^{10}Be and ^{26}Al measured in the samples were produced after burial, this is unlikely. While the post-burial history of exposure is unknown, we purposely selected the sample site because the section is being undercut and eroded by the modern unnamed stream (Figure 2.3), resulting in a very low probability for the deeper sample having a significantly greater exposure history.

A final explanation is that there was some inconsistency in the sample preparation or measurement by AMS or ICP-OES that has not been realized. Their AMS precisions are equivalent at 16.6% 1σ , and while sample PPI-17-105-17 had a slightly lower current, the

target lasted through five 5-minute runs. They also had comparable concentrations of native Al (58.2 and 70 $\mu\text{g/g}$).

In summary, the calculated simple burial durations for the two sand samples are significantly different and stratigraphically reversed. Until measurement of in-situ ^{14}C in both samples reveals significant (and proportionate differences in) post-burial production, it is not possible to determine which of the two samples, if either, are recording the correct burial duration. Additional analyses are necessary.

2.5.3.2 $^{26}\text{Al}/^{10}\text{Be}$ Cobble Isochron Ages

The ^{26}Al and ^{10}Be concentrations in all five cobble and two sand samples (Table 2.2) can be used to define a best fit curve for an isochron (uncertainty-weighted York approximation). The ^{10}Be concentrations ranged from 5.8 to 40.6 katoms/g and ^{26}Al from 5.9 to 28.4 katoms which is sufficient spread to define an isochron. The distribution was skewed toward lower concentrations (Table 2.2). Using a Matlab code provided by D. Granger for interpreting cobble isochron data, the TCN cobble isochron burial age of the sediment in D8 is 6.20 ± 0.20 Ma.

Multiple options are presented in Table 2.4, where different samples are used to define the isochron. The first option considers all seven cobble and sand samples to define the isochron, yielding an age of 6.20 ± 0.20 Ma. The second and third options remove ‘outliers’ with relatively high Al (Table 2.4, option 2) or high Be (Table 2.4, option 3). Note, these are not statistical outliers or outliers based on anything different observed in the chemistry procedure. The purpose of this comparison exercise is to provide a sensitivity test for the robustness of the isochron age. In comparison with option 1, the resulting isochron ages are older for option 2 (6.49 ± 0.21 Ma) and younger for option 3 (5.74 ± 0.29 Ma). Option 4 considers only the cobble samples and not the sand samples if one or both of those sand samples had problematic chemistry or measurement, yielding an isochron age of 7.07 ± 0.40 Ma, the oldest isochron age reported between the four options considered. As previously mentioned, there are no obvious disparities in the stratigraphy above or around these samples (such as a paleosol) and no obvious issues with the chemistry or during data reduction. All four scenarios of isochron ages fall within the Late Miocene Messinian Age. Because none of the samples

can be discounted, the isochron burial age based on all samples (option 1, 6.20 ± 0.20 Ma) is the recommended age for the deposition of the sediment at section D8.

There is a slight positive y-intercept on all four ^{26}Al vs ^{10}Be isochron plots, suggesting there may have been post-burial production. However, further testing would be needed (e.g., in situ ^{14}C) to prove that this intercept is not simply an artifact of the best fit through the data.

Table 2.4. Multiple isochron burial dating options for cobble and sand samples from Prince Patrick Island, NWT. The corresponding isochron plots for each scenario below are exhibited in Figure 2.10. All uncertainties are 1σ .

Options	Isochron Burial Age (Ma)
1) All samples included (cobble & sand)	6.20 ± 0.20
2) All samples included (except PPI-17-105-017) <i>Outlier removed due to high Al concentration (28423 atoms g^{-1}) in comparison to other samples</i>	6.49 ± 0.21
3) All samples included (except PPI-17-103-006) <i>Outlier removed due to high Be concentration (1.314E03 atoms g^{-1}) in comparison to other samples</i>	5.74 ± 0.29
4) Only cobble samples included	7.07 ± 0.40

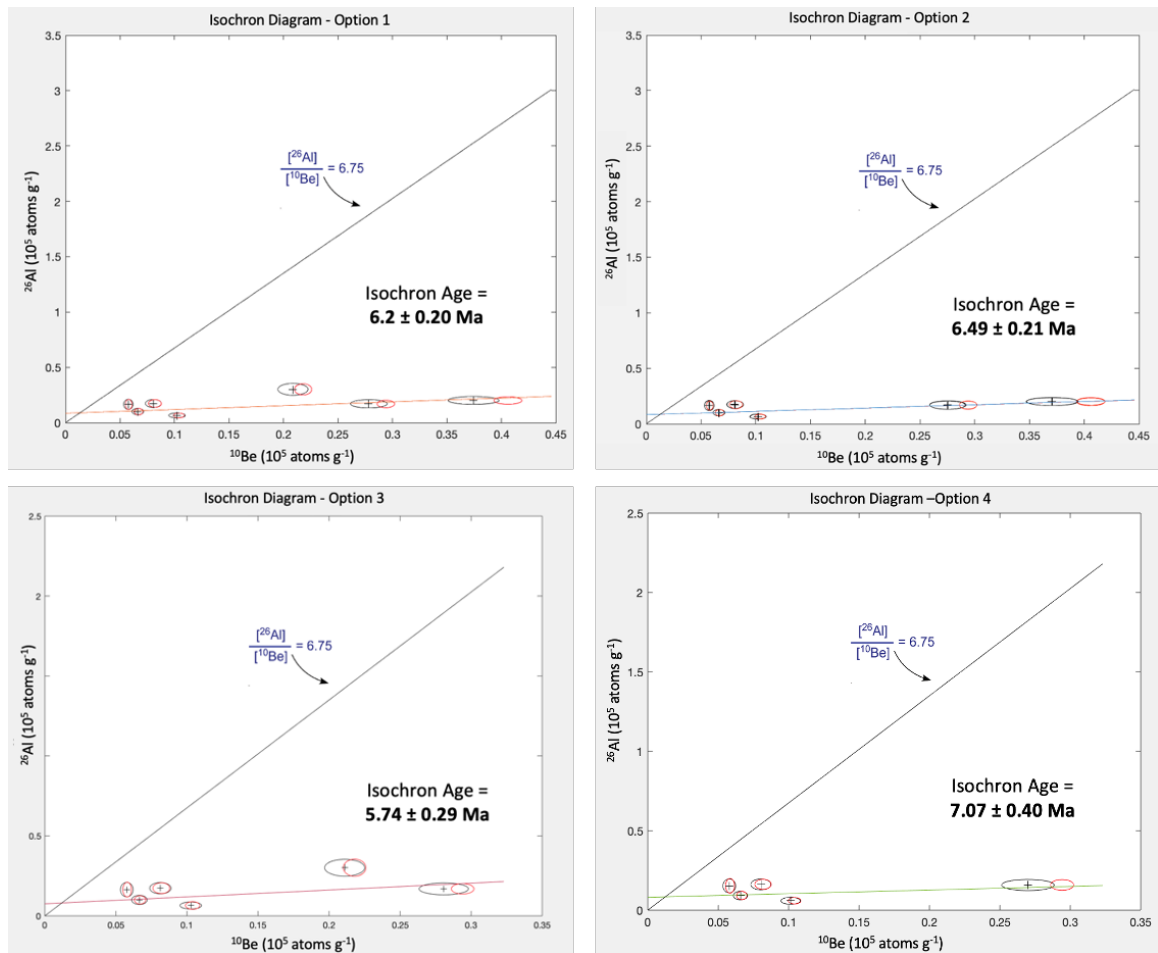


Figure 2.10. Isochron burial dating plots for cobble and sand samples from Prince Patrick Island, from multiple sample combination options (Table 2.4). Data are illustrated with different color error ellipses (1σ). The line intersecting the data is the isochron that best fits the data, from which we infer the burial age of the sediments. The solid black line has a slope of 6.75, given by the production ratio of $^{26}\text{Al}/^{10}\text{Be}$ at the surface. Option 1 (top left) illustrates the isochron with all cobble and sand samples included. Option 2 (top right) illustrates the resulting isochron plot, if sample PPI-17-105-017 is considered an outlier (high Al) and removed. Option 3 (bottom left) illustrates the isochron with sample PPI-17-103-006 removed as an outlier due to high Be. Option 4 (bottom right) illustrates the isochron with both sand samples/outliers removed.

2.6 Discussion

The age provided here (6.20 ± 0.20 (1σ) Ma) is the first TCN isochron burial age successfully applied in Canada, and the first radiometric age for the BFM on Prince

Patrick Island, near the type locality (Fyles 1990, Devaney 1991). The $^{26}\text{Al}/^{10}\text{Be}$ isochron and simple burial ages indicate that at least a portion of the BFM was deposited 6.20 ± 0.20 Ma during the Messinian. This TCN isochron age is supported by one of the simple burial ages (5.63 Ma ($^{+0.467}/_{-0.303}$), PPI-17-103-006). This age is also consistent with biostratigraphic age estimates on Prince Patrick Island, which placed the BFM *sensu stricto* during the Homeric to Clangulchian stages (~ 8 Ma)(Wolfe 1981), or Late Miocene to Early Pliocene (Hills and Ogilvie 1970, Matthews 1989, Matthews and Oviden 1990). It is not clear where the D8 section lies within the thin onshore stratigraphy of the BFM, and it is also unknown how far the BFM extends below the section or how much was eroded above. However, this age estimate extends the known range of the BFM by at least a million years and suggests that the often-quoted Pliocene age of the BFM may not be accurate.

Previous age estimates from other sites in the CAA have constrained the age of the BFM from the Zanclean to Piacenzian (5.3 to 2.6 Ma). Rybczynski et al. (2013) and Fletcher et al. (2018) used ^{26}Al and ^{10}Be TCN burial dating to show that the contemporaneous ‘high terrace sediments’ on Ellesmere Island were deposited 3.9 ($^{+1.5}/_{-0.5}$) Ma (Beaver Pond site) and 3.8 ($^{+1}/_{-0.7}$) Ma (Fyles Leaf Bed site). Additionally, simple burial dating from BFM sediments exposed along Ballast Brook on northwest Banks Island yielded a minimum age of >2.7 Ma (Braschi 2015). TCN burial dating of the contemporaneous White Channel Gravels in the Yukon yielded an age of 2.64 $^{+0.20}/_{-0.18}$ Ma (Hidy et al. 2013). There have been significant uncertainties and challenges associated with many of these dating techniques (Fyles et al. 1991, Brigham-Grette and Carter 1992, Kaufman et al. 1993). For example, at the Fyles Leaf Bed site, the effect of muons was challenging to quantify because the burial depth had certainly varied after the time of deposition (Rybczynski et al. 2013). On Banks Island, there were low TCN concentrations within the quartz at the time of deposition, and as such, an isochron could not be defined and an age could not be generated (Braschi 2015). Due to these challenges, the previously published BFM ages using TCN methodologies are considered minimum estimates, and therefore are consistent with the TCN isochron age of 6.20 ± 0.20 Ma on Prince Patrick Island reported here.

The age estimates for the BFM Meighen Island are significantly younger than the isochron age of the BFM on Prince Patrick Island. The BFM age on Meighen Island was considered to be ~3.1-3.2 Ma based on the discovery of mixed Atlantic Ocean (*Arctica* cf. *A. islandica*, *Arctinula greenlandica* and *Astarte*) and Pacific Ocean (*Clinocardium ciliatum*, *Hiatella arctica* and *Mya truncata*) molluscan fauna and the presence of both reversed and normally magnetized marine sediments from the Bjaere Bay region of the island (Fyles et al. 1991, Barendregt et al. *in prep*). Additionally, AAR and $^{87}\text{Sr}/^{86}\text{Sr}$ isotope dating of these marine shells in combination with climatic and eustatic correlations also support this age (Fyles et al. 1991, Brigham-Grette and Carter 1992, Kaufman et al. 1993, Barendregt et al. *in prep*). However, the opening of the Bering Strait and the ages of mixing of the Atlantic and Pacific molluscan fauna have been re-evaluated (Gladenkov et al. 2002, Gladenkov and Gladenkov 2004). Marincovich (2000) has suggested that there were multiple mixing events, with the first following the opening of the Bering Strait (4.8-5.5 Ma) and a second shorter event at ~3.6 Ma. The thickness of the marine beds (<100m) on Meighen Island is indicative of a short period of deposition (Fyles et al. 1991), which better fits the second, shorter mixing event at ~3.6 Ma. Despite the large uncertainty in the Meighen Island age, the biostratigraphy on Meighen Island supports a Pliocene age estimate (Matthews and Ovenden 1990, Matthews et al. 2019).

The biostratigraphy on Prince Patrick Island is quite different from that on Meighen Island, suggesting there may well be significant age differences between them. Matthews and Ovenden (1990) report the Prince Patrick Island floras contain taxa that were not observed on Meighen Island. They postulated that these floristic differences could be due to (1) geographically induced climatic differences, such as continentality, amongst otherwise contemporaneous site records, or (2) significant age differences between the deposits themselves. The Messinian age of the BFM on Prince Patrick Island presented here supports the second hypothesis by Matthews and Ovenden (1990), who suggested that the BFM on Prince Patrick Island is Clamgulchian in age (8-2.5 Ma in terms of the Cook Inlet biostratigraphic stages, Wolfe 1981). The Messinian age of the BFM on Prince Patrick Island is also supported in the literature by Hills and Ogilvie (1970), who, based on biostratigraphic evidence, suggested the BFM on Prince Patrick Island is likely Late Miocene or Early Pliocene in age (Homerian to Clamgulchian stages, Wolfe 1981).

Additionally, Fyles et al. (1994) suggested that the BFm exposed along Ballast Brook on Banks Island could be Clamgulchian in age as well, perhaps similar or slightly younger than the BFm on Prince Patrick Island. Fyles et al. (1994) hypothesized that the BFm was deposited synchronously across its geographic extent (within 10s of thousands of years). However, the varying ages reported for the BFm and the suggestive floristic differences between sites (Matthews and Ovenden 1990) suggest that instead, the BFm was likely deposited diachronously (hundreds of thousands of years to millions of years) across multiple sites. However, it is difficult to subdivide the BFm into multiple units due to the lack of unconformities within the section.

The Messinian age of the BFm on Prince Patrick Island is older than previous estimates. There are a variety of potential reasons for this incongruity. The section sampled on Prince Patrick Island could be an older part of the stratigraphy compared to samples from alternative sites on Banks Island or Meighen Island. It could be postulated that the exposure of a deeper section is due to a significant glaciotectonic event or events that thrust a much deeper and older 30 m section upward. However, there is no supporting evidence for an event like this within the stratigraphy on Prince Patrick Island, suggesting that this is unlikely the cause of the older age. Alternatively, perhaps a significant amount of erosion may have occurred on Prince Patrick Island (in comparison to other sites), which exposed a deeper section of the BFm stratigraphy. Models by Manion (2017) have suggested that upwards of 200 to 400 m of sediment could have been removed from the arctic islands due to incision; perhaps there was significant erosion occurring on Prince Patrick Island.

2.6.1 Sedimentology and Stratigraphy of the Beaufort Formation on Prince Patrick Island

The stratigraphy and sedimentology of the BFm near the type locality on Prince Patrick Island have been revisited. The facies composition at sites D8 and S1 suggest a braided stream depositional environment was present on Prince Patrick Island, consistent with previous observations (Fyles 1990, Devaney 1991). The >2 m thick peat layer at section D8 and the numerous woody detritus layers at section S1 suggest overbank deposits, or lower energy sections of the BFm. This interpretation is supported by beetle

fossils previously identified within the BFm on Prince Patrick Island that were interpreted to have lived in proximal wetland biotopes or active floodplain sites near the river (Matthews and Ovenden 1990, Elias and Matthews 2002). The D8 and S1 sections described in this paper were approximately similar in height to the BFm type locality on Prince Patrick Island. However, at the type locality, trough cross-bedding recurred approximately every 2-4 m (Fyles 1990), whereas, at section D8, no trough cross-bedding was observed, and at section S1, only one portion of the bottom of the section recorded such facies. The type locality is capped with a section of fluvial gravel and erratic boulders, similar to the D8 section, which has been interpreted as Quaternary glacialfluvial outwash. However, this facies was not observed at the top of section S1. This could suggest that sections D8 and S1 occur at different time periods within the overall BFm, however, since section S1 was not dated, it is unclear which section is older. Cretaceous shale is exposed at an unconformity near the base of sections at the type locality. That no basal shale was recognized at either the D8 or S1 sections, suggest they may be shallower sections of the BFm and/or that varying amounts of erosion occurred between the three sites to expose different sections of the BFm.

Paleoflow measurements in section D8 (Figure 2.6) indicate that during the BFm deposition, flow was towards the WSW, consistent with measurements from BFm deposits along Ballast Brook on Banks Island (Braschi 2015) and at the type locality (Fyles 1990). These paleoflow records confirm that the inter-island channels, including M'Clure Strait, were not major fluvial networks or significant enough depressions to deflect paleoflow towards them during the Messinian. Instead, the BFm was likely a continuous coastal plain flowing towards the Canada Basin to the west. This interpretation supports the hypothesis by Manion (2017) and seismic observations (Chapter 3) that the inter-island channels were only extensively incised during the Pleistocene, probably first by fluvial and then later by glacial incision.

2.6.2 What were the causes of deposition of the Beaufort Formation?

With little to no substantial uplift within the region during the Late Miocene and Pliocene (Miall 1979), the climate changes during the deposition of the BFm (i.e., $\delta^{18}\text{O}_{\text{benthic}}$ record, Figure 1.2) must have significantly influenced the mobilization,

transportation, and deposition of the sediment from large distal expanses of the Arctic. For example, sediment availability and mobility are controlled by temperature (MAT, range, freeze-thaw cycles) and precipitation (amount, style, intensity) effects on weathering and erosion, or indirectly through changes in ice cover, permafrost activity, and vegetation. Understanding the preconditions necessary to mobilize >3 km worth of sands and gravels deposited over 1200 km transect of the western CAA could provide crucial information about the role of climate in an area that was not particularly tectonically active.

The Messinian coincides with a climate maximum, and biostratigraphic evidence, $\delta^{18}\text{O}_{\text{benthic}}$ records, and sea level records suggest above average temperatures (Figure 1.2) (Matthews 1989, Matthews and Ovenden 1990, Matthews et al. 2019). The BFM sediments contain abundant subfossilized remains of plants, arthropods, and vertebrates which have been used to estimate the paleoenvironment and MAT at the time of deposition and are suggestive of a much warmer paleoclimate (up to 19°C, Ballantyne et al. 2010, Csank et al. 2013). The Messinian age reported here suggests that at least a portion of the BFM on Prince Patrick Island was deposited during the relatively stable (low-amplitude orbital forcing) warm period of the Late Miocene (Figure 1.2).

The Messinian climate maxima was followed by a period of significant cooling, a eustatic sea level drop, and a large-scale microfauna turnover, and the introduction of cool-water assemblages to the region (McNeil et al. 2001, Miller et al. 2020, Figure 2). The cooling of climate may have provided suitable conditions to trigger an increased deposition of sediment through the first occurrence of glaciations in this region. Portions of section D8 and S1 may have recorded some of this cooling period, as their coarsening upward trend indicates higher energy systems in the catchment.

While only thin (<100m) sections of the BFM are exposed onshore, petroleum exploration wells and multi-channel seismic surveys (Miall 1979, Kumar et al. 2009) demonstrate that Late Miocene to Pleistocene clastic strata thicken to >1 km at 50 km from the modern Prince Patrick Island coast (Fyles 1990, their Fig. 5). Lithospheric flexure modeling has demonstrated that upwards of 200-400 m of sediment must have eroded from the present-day CAA after the Pliocene (Manion 2017). Sections D8 and S1

likely only record a portion of the BFM's depositional history and erosion has removed perhaps a majority of the onshore record. Parts of the offshore Pliocene-Pleistocene IpS, which has upwards of >3km of sediment, could be correlative with the BFM and may contain a much more complete record than the onshore sedimentation. Therefore, correlations between the onshore BFM and offshore IpS stratigraphy could increase our understanding and knowledge of the BFM sedimentation through time. The base of IpS is a regional unconformity interpreted to be Late Miocene in age (McNeil et al. 2001). The Messinian age of the BFM on Prince Patrick Island provides a minimum limiting age for the base of the offshore IpS in the Late Miocene.

2.6.3 The Pliocene as an analogue for future warming?

A barrier to the reconstruction of the BFM paleoenvironmental record is identifying whether these deposits record interglacial periods or average conditions because many of the paleoclimate proxies are spatially and temporally isolated from each other. For example, Csank et al. (2013) suggested that since the Bylot Island forest and Kap København deposit in Greenland represent warm interglacial periods within the overall cool Plio-Pleistocene, and other Arctic forest records may also only capture a snapshot of interglacial conditions rather than an "average" climate. Therefore, they may not be suitable to study long-term Pliocene cooling. A drawback of the TCN isochron burial age is that the uncertainty is not small enough to narrow the age interpretation to just a singular interglacial or glacial period. Additional isochron ages from the BFM will be required to better constrain this chronological uncertainty, and future work should focus on reducing the uncertainty in TCN isochron ages themselves. Until then, it is difficult to use various proxies to establish past climates in the High Arctic without a numerical age upon which to base them off and may hinder the use of these records for future warming predictions.

The opening of the inter-island channels may have had significant effects on the continentality of the interior CAA, on ocean circulation before and after the opening of the channels, and on the climate evolution of the Quaternary, including the steepening of the latitudinal temperature gradient (Ballantyne et al. 2010). The paleoflow records presented here suggest these channels may not have been incised during the deposition of

the BFm in the Messinian, and as such, are a significant feature that was not present in the Canadian Arctic during the Late Miocene or Pliocene. Certainly, this would inhibit using the Pliocene as a suitable analogue for future warming, despite similar average global temperatures during the period.

2.6.4 Uncertainty in Isochron Age

The successful use of the TCN cobble isochron dating method on Prince Patrick Island suggests that it is a viable tool for future chronological investigations in order to constrain the age of the BFm. The Messinian age of the BFm on Prince Patrick Island has expanded the age range of the deposition of the BFm through time, however, the error within this age still records many glacial and interglacial cycles. Additional testing is recommended (i.e., re-running the ^{26}Al samples and testing in situ ^{14}C) to investigate if the y-intercept of the isochron age reported here is the result of post-burial production or an artifact of the best fit through the data and to investigate the discrepancy in the simple burial dating ages. The TCN isochron burial age did not significantly reduce the uncertainty in the burial ages compared to the simple burial age method, however, it is proven as a valuable tool to determine if there has been post-burial production in the samples. Continued efforts to reduce the uncertainty associated with this method are encouraged and would allow further constraint of the chronology to a specific interglacial or glacial cycle.

2.7 Conclusions

The TCN isochron dating method has provided an absolute age of the BFm (6.20 ± 0.20 (1σ) Ma), attributed to the middle part of a 35.7 m thick section near the type locality of the BFm, below an unconformity covered by Quaternary glaciofluvial outwash. This date expands the previous age range of the BFm into the Messinian and suggests that a strictly Pliocene age, often cited in the literature for the BFm, is not appropriate. The date is supported by previously published biostratigraphic age estimates of the Late Miocene floral and faunal records. This age suggests that previous observable differences in the subfossil record between CAA sites (such as between Meighen and Prince Patrick Island) are due to actual variations in the age and not due to an effect of

continentality. This conclusion suggests that care must be taken in equating paleoclimate and biogeographic information across multiple sites. The sedimentology suggests there were braided stream sediments deposited in the BFm on Prince Patrick Island during the Messinian. However, sections D8 and S1 of the BFm on Prince Patrick Island are almost certainly significantly eroded and therefore represent an incomplete stratigraphy in comparison to what exists offshore. It is unknown where the D8 and S1 sections lie within the onshore stratigraphy of the BFm, how far the BFm extends below, or how much was eroded above. Future work should continue to garner new numerical ages of the BFm, to further constrain the synchronicity, duration, and timing of the BFm, a crucial step towards understanding the preconditions and climate triggers involved in the deposition of the BFm. The 6.20 ± 0.20 Ma date produced by this study will place important paleoenvironmental records within a more robust chronostratigraphic framework and context, allowing hypotheses regarding temporal and spatial climatic variability to be further investigated.

Future work includes using the newly acquired Be concentrations to calculate basin-wide average erosion rates of the BFm and can be used to estimate deposition rates and sediment flux to the Banks Island shelf during the Messinian through Pliocene. This, in combination with the expanded age range of the BFm *sensu stricto* (Messinian to Piacenzian), can be used to test hypotheses regarding the diachronous deposition of the BFm. Continuing to acquire further chronological constraints will advance our understanding of the exact timing and cause of deposition of the BFm and our understanding of the Arctic landscape evolution during this period of significant climate transition.

2.8 Acknowledgments

G. Yang prepared the ^{10}Be and ^{26}Al targets from quartz at the Dalhousie University CrisDal Lab. A. Hidy at Lawrence Livermore National Laboratory-CAMS ran the accelerator mass spectrometry. Logistic support was provided by the Polar Continental Shelf Program (XXXX). This research was also supported by NSERC Discovery Grants to JCG (XXXX). We acknowledge the PGC for access and use of the 5m ArcticDEM.

Chapter 3. The Late Cenozoic Evolution of the Banks–Beaufort Basin, Arctic Canada

Manuscript in preparation for submission to *Marine Geology*. My contributions include (i) writing the manuscript and making modifications based on suggested edits from co-authors, (ii) creating all the figures and tables within this manuscript sans Figure 3.10 and Figure 3.11 which were prepared by Ned King (iii) conducting all the seismic interpretation at the GSC-Calgary and Bedford Institute of Oceanography (iv) completing all facies interpretations of the seismic (v) performing all the volumetric calculations (vi) creating all the surface, isopach, and facies maps within ArcGIS

Sydney A. Stashin (1), John C. Gosse (1), Edward L. King (2), I. Rod Smith (3)

(1) Department of Earth and Environmental Sciences, Dalhousie University, Halifax, NS B3H 4R2 Canada

(2) Geological Survey of Canada, Dartmouth, NS B2Y 4A2 Canada

(3) Geological Survey of Canada, Calgary, AB T2L 2A7 Canada

3.1 Abstract

The Iperk Sequence (IpS), in the Beaufort Sea and Canada Basin, is a thick (>4 km) package of fluvial and marine sediment. Offshore Banks Island, the IpS uniquely preserves an almost complete section of Late Miocene-Pleistocene stratigraphy and may document significant basin evolutionary changes during these time periods, including the Canadian Arctic's transition from a contiguous landmass to a divided archipelago. Due to previous data limitations, owing in part to the inaccessibility of the region, the IpS has not been subdivided into its Late Miocene through Pleistocene components. Newly acquired, high-resolution 2D marine seismic reflection data from ION were used to develop a complete basin model of the Late Miocene through Pleistocene deposition within the Bank-Beaufort Basin, including shelf and trough stratigraphy and sediment volume estimates. For the first time, the sequence is subdivided and lithostratigraphically correlated to onshore remnants of the detrital wood-bearing Beaufort Formation (BFm). Eight sequences lying on a regional unconformity have been interpreted based on six

widely observed seismic facies and reveal a much more complete record, relative to the onshore BFM, of an immense Arctic landscape response to a polar-amplified global climate transition. An older shelf crossing glaciation was identified from these sequences, extending the glacial history of the Banks Island shelf. Near-shore facies deposits may provide the first evidence for the position of Pliocene shorelines, ~50 km offshore on the Banks Island shelf. Hypotheses regarding the formation of inter-island channels, including M'Clure Strait and Amundsen Gulf were tested and indicated that the channels were likely formed via Pleistocene fluvial and glacial incision, not faulting.

3.2 Introduction

There are few locations globally that record the response of onshore and offshore environments during the Pliocene-Pleistocene cooling. Arguably one of the best locations to capture this evolution would be in a polar setting where ice-free Miocene and Pliocene landscapes evolve to glacial environments earlier and more intensely, owing to the feedback-controlled amplification of temperature and other climate changes at high latitudes (Ballantyne et al. 2010, Csank et al. 2011). The westward-thickening clastic wedge along the western Canadian Arctic Archipelago (CAA) in the Beaufort Sea and Canada Basin (Figure 3.1A) is a highly suitable location, however, the offshore component has been understudied. This is mainly owing to sea-ice obstacles to offshore drilling and seismic acoustic imaging (no offshore wells exist in the Banks–Beaufort Basin).

The Banks–Beaufort Basin (referred to as such by Dixon et al. 1992), offshore Banks Island, may have captured the late Neogene climate change independent of tectonic uplift that appears to have contributed to variation in sediment flux to the contemporaneous basins to the southwest, in particular the Beaufort–Mackenzie Basin (Figure 3.1A; Dixon et al. 1992). High-quality marine multichannel 2D seismic reflection data for the shelf and slope area of the Banks–Beaufort Basin, acquired in 2006-2008 by ION (Figure 3.1B), was recently made available as multi-client data for interpretation by the Geological Survey of Canada. It enables the first opportunity to resolve sub-sequence stratigraphy in the >3 km thick Neogene and Quaternary deposits previously interpreted to be equivalent to the Iperk Sequence (IpS) in the Beaufort–Mackenzie Basin to the

southwest (Dixon et al. 1992). It also permits a seismostratigraphic correlation between the relatively incomplete record of the onshore braided stream sediments of the Beaufort Formation (BFm) (Miall 1979, Fyles 1990, Devaney 1991, Fyles et al. 1994) and a portion of the offshore clastic wedge, both pinned by a prominent basin-wide unconformity (approximately of Late Miocene age, McNeil et al. 1990) that is also expressed onshore (Hills et al. 1974, Fyles et al. 1994). It is now also possible to extend and adjust recent interpretations of the offshore Quaternary stratigraphy north from Amundsen Gulf (Batchelor et al. 2013b, 2013a, 2014, Batchelor and Dowdeswell 2014) and to contrast the dominantly climatogenic record of the Banks–Beaufort Basin stratigraphy with the Beaufort–Mackenzie Basin sequences.

Our results may hold direct implications towards several other Arctic investigations. The rationale by Fyles (1989) and Fyles et al. (1994) for the distinction between coeval ‘high terrace sediments’ or gravel deposits on Ellesmere Island (BFm *sensu lato*) and the BFm *sensu stricto*, which is primarily preserved in a 100 km wide belt along the western edge of the CAA islands (Figure 3.1A) is that the latter records a once contiguous coastal plain. Our interpretation places those coastal BFm deposits into the framework of a Beaufort Sea coastal plain-clastic wedge system. An interpretation of the seismostratigraphy was also required before providing an initial survey of the fault systems that cut post-Messinian stratigraphy and suggest a mechanism for the opening of the inter-island channels. Our tentative chronostratigraphy also informs ongoing and planned research aimed at paleoecological, paleoclimatological, and paleoenvironmental reconstructions for high latitude Late Neogene cooling (Robinson et al. 2008, Ballantyne et al. 2010, Csank et al. 2011, Rybczynski et al. 2013, Mitchell et al. 2016, Fletcher et al. 2019). This reconstruction work benefits from the remarkable preservation of subfossilized floral and faunal material and have the potential for Neogene bulk sediment DNA analyses (Valk et al. 2021). Additional constraints of depositional settings (glacial, interglacial, stream, lake, estuary) and a robust chronology are critical for interpreting spatial patterns among the various onshore sites throughout the CAA.

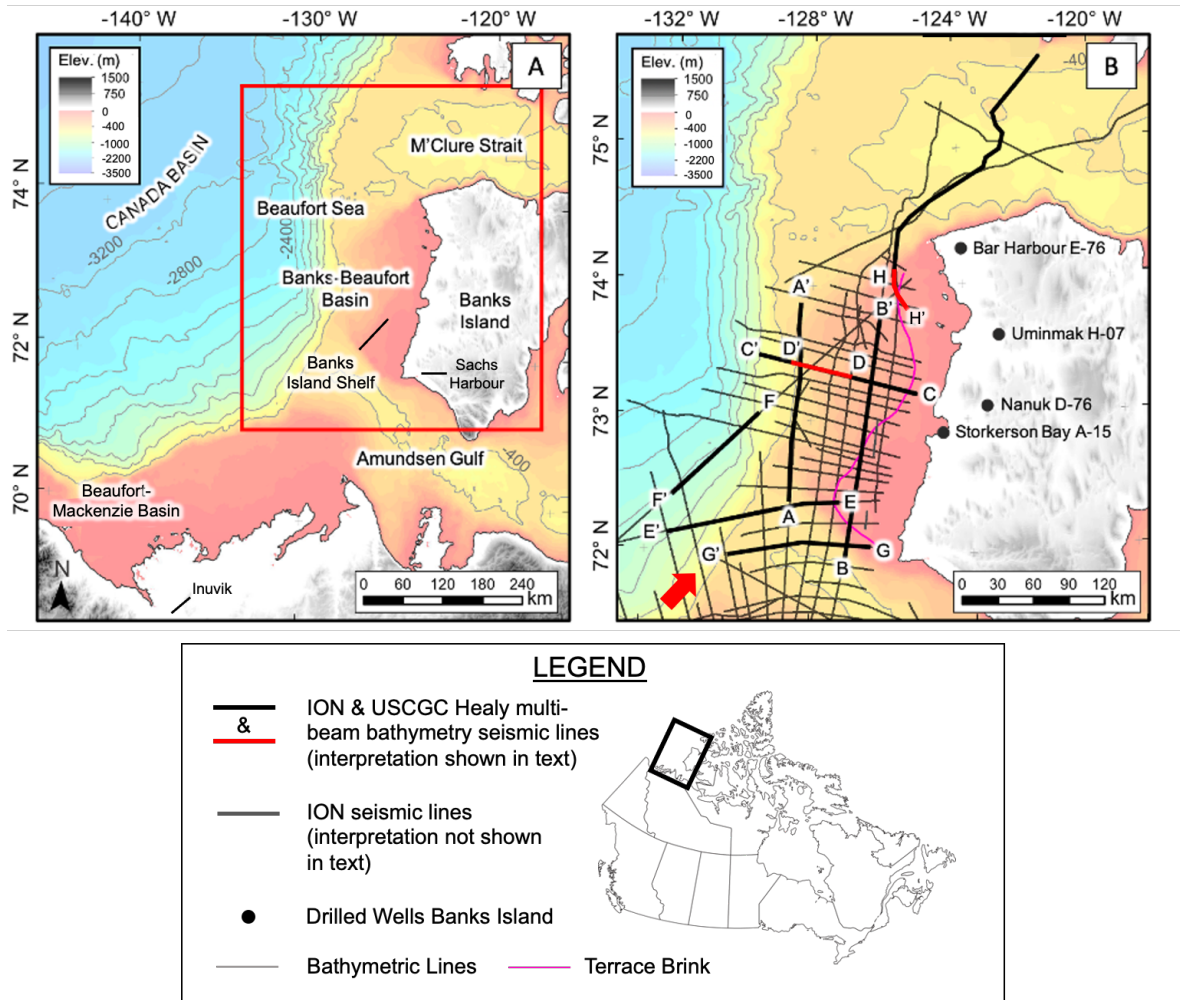


Figure 3.1: A: GEBCO sea floor bathymetry map of the Canadian Beaufort Sea and surrounding features (400 m contours) and land topography (grey topographic shading) showing locations of Amundsen Gulf, M'Clure Strait, Mackenzie Delta, Banks Island, and Beaufort Sea (GEBCO Digital Atlas published by the British Oceanographic Data Centre on behalf of IOC and IHO, 2003). B: Enlarged map with location shown by the red box. The distribution of ION seismic lines and one USCGC Healy multi-beam bathymetry line (H-H') are shown on the Banks Island shelf. The magenta line indicates the location of a late-stage inner shelf glacial terrace (see Figure 3.1). The annotated thicker black lines and the red line (D-D') indicate seismic lines discussed in text and illustrated in Figure 3.4, Figure 3.5, Figure 3.6, Figure 3.10). The red arrow (bottom left of Figure 3.1B) shows the viewpoint and direction of view of the 3D model in Figure 3.11, panel A.

3.3 Background

The Banks–Beaufort Basin extends west from Banks Island of the CAA into the eastern Beaufort Sea and Canada Basin (Figure 3.1A). It fills part of a broad embayment of the Arctic Ocean between the Alaskan North Slope and the CAA, which locally reaches up to 15 km in sediment thickness (Dixon et al. 1992). Banks Island was covered by part of a once contiguous arctic coastal plain (Figure 3.2) (Miall 1979, Fyles et al. 1994) which extended from what is now the northern Canadian mainland to Meighen Island and possibly Axel Heiberg Island. By the Late Pliocene, a theorized combination of fluvial and glacial incision had begun to form what is now Amundsen Gulf (Figure 3.1A), separating Banks Island from the mainland (Fortier and Morley 1956, Pelletier 1966, Manion 2017). A similar mechanism likely created M’Clure Strait between Banks and the CAA islands to the north. Dixon et al. (1992) first introduced the term Banks–Beaufort Basin and intended the name to include the offshore and onshore depositional basin. It comprises Late Cretaceous to Cenozoic strata and geographically includes Banks Island and the adjacent offshore parts of the Beaufort Sea (Figure 3.1A). The offshore seismostratigraphy is not constrained by well control, and thus stratigraphic interpretations have been largely extrapolated from four of the 11 onshore wells on Banks Island (Figure 3.3), outcrops (<50 m high) of Pliocene Bfm and Miocene Ballast Brook Formations (e.g., Fyles et al. 1994, Williams et al. 2008, Braschi 2015), and by interpolation, from previous interpretations of offshore stratigraphy in the Beaufort–Mackenzie Basin to the south and west (Blasco et al. 1990, Dixon et al. 1992). The four onshore wells (Figure 3.3) are very basin marginal, providing only a condensed section of Pliocene strata compared to more numerous wells offshore in the Beaufort–Mackenzie Basin (Figure 3.1A).

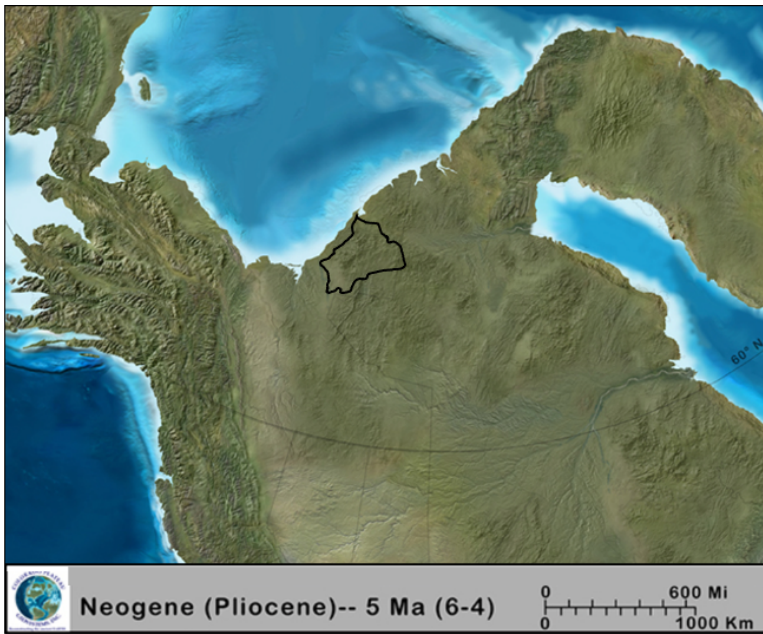


Figure 3.2. Paleoenvironmental reconstruction of Neogene Arctic Canada, indicating the inter-island channels were not formed, and the landmass was not incised during this time. Present-day Banks Island is traced in black for reference. Paleogeography map produced and permitted by R. Blakey (Blakey 2021)

The Beaufort–Mackenzie Basin extends from the Mackenzie Delta northwards into the Beaufort Sea (Figure 3.1A). It is relatively well studied, with more than 200 exploratory wells drilled in the 1970s and 1980s (see Fig. 2 in Dixon et al. 2019). By taking advantage of tolerable sea-ice conditions, numerous seismic surveys have been conducted there. Cenozoic strata of the northeastern Beaufort–Mackenzie Basin are contiguous or interbedded with the strata in the deep distal slope facies of the Banks–Beaufort Basin (Dixon et al. 1992). Prior to ION’s recent seismic acquisitions, seismic data across and seaward of Amundsen Gulf was limited and provided only a tentative correlation of strata in the Banks–Beaufort Basin.

Facies trends, the geometry of seismic architectural elements, and interpretations of paleoflow and sediment provenance in onshore records indicate that Banks Island and the Banks–Beaufort Basin received sediment from a different source than the Beaufort–Mackenzie Basin (Miall 1979, Dixon et al. 1992, Fyles et al. 1994, Braschi 2015), suggesting that its study could contribute uniquely to Arctic basin evolution. The main

difference is the lack of high relief and tectonically or isostatically uplifting ranges in the fluvial catchments that sourced the Banks–Beaufort Basin to the east during the Neogene and Quaternary (Miall 1979, Fyles et al. 1994, Braschi 2015), compared to the Beaufort–Mackenzie Basin (Dixon et al. 1992). A second difference is related to the history of glaciation of both regions. Evidence of glacial deposits within the mostly Pliocene BFm on Banks Island (Braschi 2015) and the glacial deposits interpreted in the present study have not been as widely identified in the Beaufort–Mackenzie Basin. Despite the significant differences between basins, the previous data limitations resulted in the tentative use of the Beaufort–Mackenzie Basin stratigraphy as an analogue for the shelf and upper slope stratigraphy of the Banks–Beaufort Basin (Blasco et al. 1990, Dixon et al. 1992).

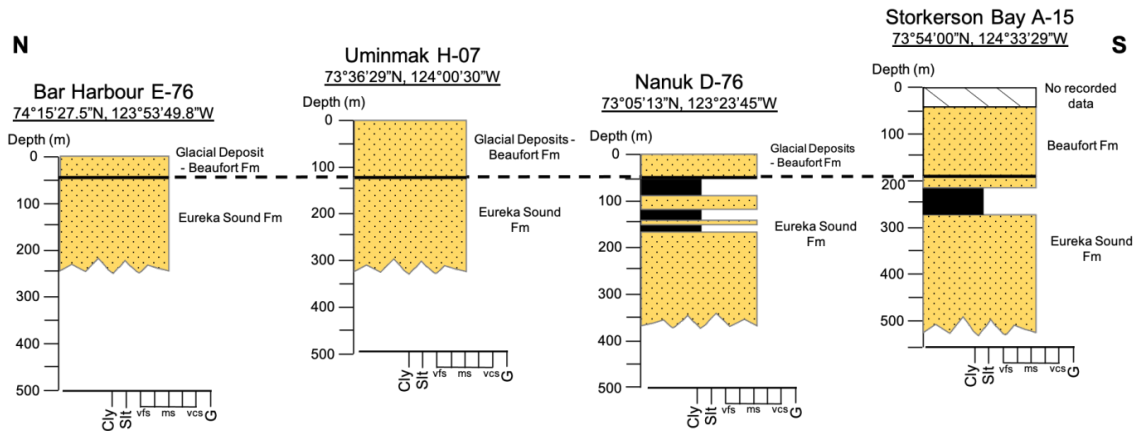


Figure 3.3. Summary of four well logs of wells onshore Banks Island (locations shown in Figure 3.1B) (Miall 1979) from north to south. Glacial deposits, if present, were not distinguished from BFm strata in the well samples. Additionally, the Ballast Brook Formation (Fyles et al. 1994, Williams et al. 2008) was not resolved within the stratigraphy or separated from the BFm or the underlying Eocene Eureka Sound Formation. The Late Miocene unconformity is marked by a solid black line and then matched across well logs.

3.3.1 Tectonic History

The Beaufort–Mackenzie and Banks–Beaufort Basins occupy the shelf and slope regions of a current passive margin setting which formed as a consequence of the opening of the Canada Basin in the Jurassic to Middle Cretaceous (Grantz et al. 1979, Lane and Dietrich 1995, Lane 2002, Dixon et al. 2008, 2019, Oakey and Saltus 2016, Piepjohn et

al. 2018). Most of the extension ceased in the Late Cretaceous and local episodes of compression, extension, and regional thermal subsidence ensued, creating the numerous northward verging reverse faults and associated parallel antiformal folds with east-west axes in the western part of the basin (*cf.* Dixon et al., 2019; their Fig. 4). Five phases of regional deformation have been delineated with respect to key unconformities throughout the basin. The last of these is the sub-Iperk unconformity of Messinian age (McNeil et al. 2001), after which the Mackenzie shelf and slope received a significant progradation (relative to earlier rates) of dominantly deltaic sediments which formed the modern shelf and slope. Pliocene and Quaternary sediments on the Beaufort–Mackenzie Basin shelf and slope exhibit little to no tectonic deformation (Pliocene compressional deformation was limited only to the central and western parts of the basin) (Lane and Dietrich 1995, Helwig et al. 2011) as thermal subsidence accommodated the sediments.

Throughout the Banks–Beaufort Basin, high-angle, listric normal faults with margin-parallel strike and basin side down splays have been observed in 2D seismic records (Fig. 4; see also Piepjohn et al. 2018), particularly along the slope. Only very few faults cut the sub-Iperk unconformity (Dixon et al. 1992). Otherwise, evidence for tectonic deformation is rare, although isolated mass wasting deposits and structures interpreted to represent fluid migration are observed throughout the Banks–Beaufort IpS (Dixon et al. 1992). Only a few normal faults continue into the marine Quaternary strata and even fewer displace the sea floor. While it is not certain if these recent scarps are gravitational, many faults show evidence of reactivation or continuation of older (Mesozoic and Paleogene) faults as revealed by an up-section decrease in offset (Dixon et al. 1992, Kumar et al. 2009). No evidence of compressional deformation has been reported in the Banks–Beaufort Basin, similar to only the eastern domain of the Beaufort–Mackenzie Basin (Dixon 1996, Dixon et al. 2019). Where seismic resolution permits, post-Miocene stratigraphy in the Banks–Beaufort Basin can be readily correlated on either side of the few faults that cut it. In the rare locations where splays or mass wasting obliterates the stratigraphy on one seismic line, adjacent lines affirm the continuity.

3.3.2 Current stratigraphic framework

Current knowledge of the Beaufort Sea Neogene and Quaternary stratigraphy is largely based on the correlation of deep 2D seismic sections with sedimentological and biostratigraphic analyses of cuttings from exploration wells drilled on the central shelf in the Beaufort–Mackenzie Basin (Jones et al. 1980, McNeil et al. 1990, Dixon et al. 1992, 2008, Kumar et al. 2009; *cf* Dixon et al., 2019 their Fig. 2). Although it has varied with author, two depositional sequences were almost ubiquitously identified within the Late Cenozoic succession of the Beaufort–Mackenzie Basin: the combined Pliocene–Pleistocene IpS and the overlying Shallow Bay Sequence (Dixon et al. 1992). The Iperk and Shallow Bay Sequences have a combined thickness of up to 4000 m in the northern-eastern portion of the Beaufort–Mackenzie Basin (Dixon et al. 1992, Kumar et al. 2009). Dietrich et al. (1985) defined the Shallow Bay Sequence to correspond only to the surficial hemipelagic marine clay and muds that form a thin veneer on top of the IpS. Dixon et al. (1992) working in the Mackenzie Trough, noted Shallow Bay Sequence strata up to 330 m thick, and commented that the internal stratigraphy of the Shallow Bay Sequence may be complex, and that with higher resolution reflection data, Pleistocene glacial and interglacial deposits may be resolvable. Elsewhere, including the Banks–Beaufort Basin, Dixon et al., (1992) indicated that the Shallow Bay Sequence could not be seismically distinguished from the IpS. Curiously, Dixon et al. (2019 their Fig. 6) represented the Shallow Bay Sequence as Holocene. Given the lack of detailed seismic facies associations, chronostratigraphy, and other correlatable lithostratigraphic characteristics in the Beaufort–Mackenzie Basin, we have chosen not to correlate the seismostratigraphy in Banks–Beaufort Basin to the Shallow Bay Sequence.

Historical reconstructions from the Beaufort–Mackenzie Basin indicate the IpS is a relatively unstructured prograding wedge of sediment interpreted to exhibit delta-related shelf, slope, and basin facies, and northwestward progradation by distances up to 120 km (Dixon et al. 1992, Dixon 1996, Kumar et al. 2009). The early phase of IpS sedimentation in the Beaufort–Mackenzie Basin included widespread lowstand deposition of base-of-slope turbidite fans. In the western part of the basin, deep-water mini-basins developed in the lower IpS, adjacent to paleo-seafloor highs above Paleogene fold structures. Intervals of pre-glacial continental shelf progradation (of uncertain age) are recorded within the

sequence and include large complex sigmoid-oblique clinoforms indicative of high-energy coarse-clastic, deltaic sedimentation (Dixon et al. 1992, McNeil et al. 2001). It was previously postulated that, unlike the underlying sequences that have depocenters unique to both basins, the IpS was deposited as a single complex that extended northeastward along the Canada Basin continental margin across both the Beaufort–Mackenzie and Banks–Beaufort Basins (Dixon et al. 1992). The IpS was envisioned mainly as coming from proto-Mackenzie sources.

While the Beaufort–Mackenzie Basin has been used as an informal analogue for the Banks–Beaufort Basin stratigraphy, this has been unsupported, owing to the absence of high resolution seismic and well data in the latter. The upper shelf sequences in both basins comprise fluvial and marine aggrading systems (Dixon 1996, Kumar et al. 2009). However, paleoflow and sediment provenance records suggest the ancestral rivers (and mountains) feeding the Beaufort–Mackenzie Basin to the south and southwest during the Messinian through Piacenzian were not the same as the much lower relief regions to the east that sourced the Banks–Beaufort Basin (Miall 1979). The Beaufort–Mackenzie Basin IpS was partly sourced from the southwest and south by the Mackenzie and Franklin Mountains following Cretaceous and Paleogene exhumation and foreland basin development of the former (Issler et al. 2005, Powell et al. 2020) and, in general, the Cordilleran Orogen (Dixon et al. 2019). However, during at least the last glaciation, sediment from a Laurentide (continental) source became more prominent (Dixon et al. 2019). On the other hand, in the Banks–Beaufort Basin, sediment provenance is relatively less well constrained for the equivalent aged sediments partly owing to the strong likelihood of reworking of the Eureka Sound Group (as evidenced by reworked Cretaceous palynomorphs in the BFm (Fyles et al. 1994) and vitrinite reflectance data on basal coal samples (Bustin 1986). Nevertheless, in the BFm, westward paleoflow directions (Miall 1979, Fyles et al. 1994, Braschi 2015) and the presence of crystalline lithologies (e.g., pink granites, Miall 1979) and cherts are consistent with sediment sources to the east (including Victoria Island, Fyles et al. 1994). There is no topographical or thermochronological reason to suspect a tectonic influence in the IpS source region for the Banks–Beaufort Basin.

3.3.3 The Beaufort Formation

Relative to the offshore, the BFm component of the clastic wedge is slightly better characterized. In this manuscript, we follow the recommendation of Fyles (1990) to restrict the name BFm as originally applied by Tozer (1956) to the unconsolidated wood-bearing quartz-rich predominantly sandy braided stream beds similar to the type locality on Prince Patrick Island. The BFm is restricted to coastal plain sediments exposed on the western edge of the CAA and is younger (initially based on biostratigraphic ages, Hills et al. 1974, Matthews 1989, Matthews and Ovenden 1990) than similar beds such as the Middle Miocene Ballast Brook Formation (Fyles et al. 1994, Williams et al. 2008). On Banks Island, the BFm is predominantly composed of cross-stratified medium-grained sand with minor units of interbedded clay and ripple-laminated fine-to medium sand (Fyles et al. 1994, Braschi 2015). The BFm also includes abundant unconsolidated pebble and gravel clasts, infrequent amounts of chert and some rare pink granite clasts likely originating from the Canadian Shield (Miall, 1979). Paleocurrent analysis, facies relationships, thermal maturity models, and provenance studies of the gravels and sand beds suggest that the BFm is largely sourced from Paleogene and Paleozoic strata to the east (Miall 1979, Bustin 1986, Fyles et al. 1994, Braschi 2015). However, the sediment provenance for the entire BFm ranges from volcanic uplands on Axel Heiberg (as observed in the BFm on Meighen Island, Fyles et al. 1991) to Victoria Island (for Banks Island, Fyles et al. 1994). Much of the mature (quartz and chert) sand may have been reworked from the Eureka Sound Group, which extended from central Ellesmere Island and westward towards Banks Island (Fyles et al. 1994). Therefore, lithology is not an adequate diagnostic characteristic without a systematic detrital thermochronology or geochemical basis. As mapped by Fyles (1990), the BFm stretches continuously along the western edge of the CAA islands, forming a narrow (100 km wide), coast-parallel 1200-km long fragmented belt geometry. This pattern is analogous to the Pleistocene Lissie and Beaumont Formations, which parallel younger incised coastal plain belts along the Texas gulf coast (Blum and Aslan 2006). This pattern suggests syn- or post-depositional lithospheric flexure may have affected the BFm (Manion, 2017). Isolated outcrops east of the mapped unit are observed on Banks and Prince Patrick Island and our mapping on

Prince Patrick Island (Chapter 2) suggests some modification of the mapped unit may be necessary.

The total thickness of the BFm is uncertain owing to the paucity of well data. The relief of the western CAA, provided mostly by post-BFm incision, rarely exposes more than 50 m of the formation. Fyles (1990) suggested that the thickness of the BFm along the coast of Prince Patrick Island (where its type-locality is defined; Tozer 1956) reaches upwards of 1000 m and averages 600 m. Wells on Banks Island (Figure 3.1B, Figure 3.3) and Prince Patrick Island reveal thicknesses ≤ 200 m for Pliocene strata (Kumar et al. 2009, Helwig et al. 2011), although the base of the BFm is not well established from those wells because much it is partly based on the distinction between degrees of coalification of the wood detritus and very limited biostratigraphic information. For instance, the Ballast Brook Formation on Banks Island contains Middle Miocene wood that has flattened cross-sections and more coalification than the BFm (Fyles et al. 1994, Williams et al. 2008). But the Ballast Brook Formation was not indicated in the well logs. At one time, the BFm and equivalent fluvial deposits were much thicker and had a greater distribution on land than present-day outcrops suggest (Miall 1979, Bustin 1982, Smith 2020). Flexural models for the western Archipelago require significant exhumation of BFm and equivalent deposits during the Pleistocene, with a minimum of 200-400 m of BFm denuded by stream and glacial erosion from the islands and at least 900 m from the inter-island channels to explain the current >500 m bathymetry in the straits (Manion 2017).

Sandy braided stream deposits have been interpreted to be equivalent to the BFm throughout the CAA, consistent with but not evidence of the notion that the CAA was a contiguous landmass until sometime in the Pliocene or Pleistocene (Braschi 2015, Manion 2017). For instance, thin and isolated deposits of wood-bearing gravel on Melville Island have been postulated to be remnants of the BFm (Hodgson et al. 1984). Subfossilized wood-bearing sands similar to the BFm have been observed as far east as Bylot Island (off Baffin Island, Csank et al. 2013). Contemporaneous beds exist on Ellesmere and Axel Heiberg Islands and are informally referred to as 'high terrace sediments' (Fyles 1989). At a facies scale, parts of the 'high terrace sediments' resemble the sandy braided stream deposits with detrital wood and peat layers of the BFm.

However, the ‘high terrace sediments’ exhibit a much greater variety of depositional environments vertically and laterally. Fluvial and distributary beds are found at the stratigraphic level as lacustrine sediments, some containing varve-like rhythmites with dropstones such as those at Fyles Leaf Beds on Ellesmere Island, which grade upward to high-amplitude distributary bars (> 1m height) and well-sorted cobble gravels (Fyles 1989, Rybczynski et al. 2013). Such rapid environment changes along with a slightly steeper fluvial bed gradient are consistent with the higher relief setting of the ‘high terrace sediments’ and distinct from the more uniform facies and shallow gradient of the coastal plain. Furthermore, outcrops of similar unconsolidated braided stream sediments exist throughout the CAA and may be contemporaneous with the BFm, but without the well-preserved wood or numerical age control they may be interpreted as more recent fluvial or glacialfluvial deposits, possibly redeposited BFm sediment. South of the CAA, similar fluvial beds have been related to the BFm, such as in the Beaufort–Mackenzie Basin, but for the reasons listed above, particularly the lack of adequate age control at either location, Fyles et al. (1994) recommended not considering them BFm. However, as cosmogenic nuclide burial dating and other geochronometers continue to provide numerical ages of these contemporaneous deposits, the definition of the BFm should be re-evaluated. The restriction of the woody braided stream deposits to only the westernmost portion of the CAA was initially based on this stratigraphic setting rather than a chrono- or lithostratigraphic rationale. The latter would likely result in a significant expansion of the lithostratigraphic unit.

Some recent reinterpretations of sediments interpreted to be older or otherwise related to the BFm on Banks Island merit special mention because the initial interpretations may create confusion. Vincent (1983), working along the southwest coast of Banks Island, defined the Worth Point Formation as a preglacial assemblage of organic-bearing fluvial, eolian, and colluvial deposits overlying BFm gravels. It was estimated to be Late Pliocene to Early Pleistocene based on biostratigraphic and paleomagnetic interpretations (Matthews 1989, Barendregt et al. 1998) and was correlated with the IpS offshore (*cf.* Dixon et al. 1992). However, the Worth Point stratigraphic sections were recently dismissed as a coherent stratigraphic unit and are now interpreted to be a complex glacetectonic melange of bedrock, BFm sediments, and

glacial sediment facies (Vaughan et al. 2014). Similarly, the Mary Sachs Gravel from the lower Duck Hawk Bluffs site on southwestern Banks Island, previously considered to be BFm (Matthews et al. 1986, Fyles 1990), or Worth Point Formation equivalents (Vincent et al. 1983, Barendregt and Vincent 1990), are now considered a complex glacitectonic assemblage of bedrock, BFm, and glacial sediments (Evans et al. 2014). Based on associated macroflora (Hills et al. 1974, Vincent et al. 1983), the basal gravel at Duck Hawk Bluffs was initially assigned to the BFm. Differences between the macroflora at the BFm type locality on Prince Patrick Island and the basal gravel at Duck Hawk Bluffs led Fyles et al. (1994) to designate these as the Mary Sachs gravel instead. Overlying this basal gravel, Vincent et al. (1983) described units of aeolian, fluvial and lacustrine sand and gravel which they correlated with the Worth Point Formation. Evans et al. (2014) indicated instead that both of these units are part of an aggradational glacialfluvial deposit, which has reworked BFm sediments from somewhere up-flow within the Amundsen Gulf catchment. They do not place an age on these but note that Barendregt and Vincent (1990) indicate magnetically reversed sediments within this unit, potentially within the Matuyama chron, >0.78 Ma.

3.3.4 Relationship between the Iperk Sequence and Beaufort Formation

The IpS has been proposed to be chronostratigraphically and in places lithostratigraphically correlative to the onshore BFm (*cf.* Hea et al. 1980, Blasco et al. 1990, McNeil et al. 2001). With the limited resolution of seismic reflection data previously available in the Banks–Beaufort Basin, everything above what was interpreted to be the prominent Late Miocene unconformity was considered to be equivalent to the IpS of the Beaufort–Mackenzie Basin (Dixon et al. 1992, 2019, McNeil et al. 2001, Kumar et al. 2009). An angular unconformity (and in places disconformity) observed onshore in the Ballast Brook valley on northwestern Banks Island separates the Ballast Brook Formation from the BFm (Matthews 1989, Fyles et al. 1994). In the Beaufort–Mackenzie Basin, a correlative angular unconformity was attributed to a period of widespread epeirogenic or isostatic uplift or eustatic lowering of sea level during the Messinian (Late Miocene) (Dixon et al. 1992, McNeil et al. 2001). Thus, considering the absence of well data, this unconformity is the only direct tie to link Messinian and younger onshore and offshore deposits in the Banks–Beaufort Basin. Prior to the current

study, fundamental correlations between the onshore and offshore units were tentative at best. The most recent chronology of the IpS based on $^{87}\text{Sr}/^{86}\text{Sr}$ measurements on benthic foraminifera collected in wells from the Beaufort–Mackenzie Basin were no older than 2.09 Ma according to McNeil et al. (2001), however, they suggested there may be inconsistencies within the Sr isotopic data that further chronology will need to address; this age may be an underestimate. Other age estimates of the unconformity range from a biostratigraphic age of Mid to Late Miocene at Ballast Brook (i.e., < 11 Ma, Matthews 1989) or during a global lowstand during the Messinian (McNeil et al. 2001). The recent eustatic sea level analysis by Miller et al. (2020) reveals several possible ages for such a widespread global lowstand. Referring to the paleomagnetic polarity chron-tuned ages, lowstands occurred at ca. 9.8, 8.5, and 4.9 Ma) (Miller et al. 2020, their Fig. 1). These suggest the possible age constraints for the sub-Iperk unconformity and the base of the IpS.

3.3.5 Post-Messinian Climate

The IpS and BfM are of particular interest because they present an opportunity to capture the basin response to the largest, most recent global climate change in the High Arctic, where that climate change was relatively amplified (Ballantyne et al. 2010). Global surface mean annual air temperature (MAT) was about 2°C warmer in the Zanclean (5.33-3.60 Ma) than pre-1950 global MAT (Lisiecki and Raymo 2005). Zanclean CO₂ concentrations of 365 to 415 ppm (Pagani et al. 2010, de la Vega et al. 2020) were comparable to modern (≥ 410 ppm). As orbitally-forced global cooling began in the Piacenzian (3.60-2.58 Ma), Arctic temperature change was amplified by climate feedbacks such as albedo from sea-ice and snow cover and the loss of vegetation (Ballantyne et al. 2010). This feedback-induced latitudinal thermal amplification explains why at a local scale, MATs in the CAA were 15 to 19°C warmer in the Zanclean than today, despite only a 2°C difference globally (Ballantyne et al. 2010, Csank et al. 2011, Feng et al. 2017, Fletcher et al. 2019). As temperatures decreased globally in the Piacenzian, the global climate system was reorganizing from a state of restricted local glaciers to one of extensive global ice sheet cycles (Haywood et al. 2009). Lithospheric flexure (Manion 2017), glacial isostasy (Raymo et al. 2011), global sea level changes (Miller et al. 2020), paleoceanography changes (temperature, sea ice, and circulation,

Matthiessen et al. 2009), loss of Pliocene forests (Csank et al. 2013), and expansion of permafrost zones (Rybczynski et al. 2013, Braschi 2015) all accompanied the climate transition in the CAA.

3.3.6 Sedimentation and erosion rates

The IpS's short depositional time span (< 10 Ma) and sizable thickness (up to 4 km) represent unusually high rates of erosion and deposition. In the Beaufort–Mackenzie Basin, there was potentially a 23-fold increase in sedimentation rates during the deposition of the IpS relative to the Early and Middle Miocene (100 m/Ma in the Mackenzie Bay Sequence to 450 m/Ma in the IpS; McNeil et al. 2001). However, these rates are only applicable to the Beaufort–Mackenzie Basin and it is difficult to draw analogies to the Banks–Beaufort Basin. Due to the lack of well control and low resolution of previous seismic data on the Banks Island shelf, the sediment flux rate to the Banks–Beaufort Basin has not been estimated. Erosion rates calculated for Banks Island (49–86 cm/ka, Braschi 2015), which only represent a small fraction of the BFm catchment area, demonstrate that the erosion rates are unusually rapid for a region of relatively low relief and tectonic quiescence. It seems likely that glacial processes contributed to this erosion efficacy in the Pliocene and Pleistocene.

3.3.7 Glacial History and Trough Formation

Global ice sheet modelling suggests the onset of Northern Hemisphere glaciation likely occurred during the Early Matuyama magnetic chron (1.78 – 2.6 Ma, Batchelor et al. 2019). The oldest date constraining the first occurrence of widespread glaciation in the Canadian Cordillera is $2.64^{+0.20}_{-0.18}$ Ma (Hidy et al. 2013), and the presence of glaciofluvial facies on Banks Island at >2.7 Ma (Braschi 2015). As global climate continued to cool, northern hemisphere glaciations became increasingly more frequent and pronounced. Banks Island was completely covered by the Laurentide Ice Sheet (LIS) at least during the Late Wisconsinan LGM (25–21 ka) (England et al. 2009, Lakeman and England 2012, 2013).

Banks Island is bounded by Amundsen Gulf to the south and M'Clure Strait to the north (Figure 3.1), two basinal depressions that served as ice stream outlets for the LIS during the Late Wisconsinan and likely earlier glaciations (Stokes et al. 2005, England et

al. 2009, Lakeman and England 2012, 2014, Batchelor et al. 2013b, 2013a, 2014, Margold et al. 2015). The uppermost shelf-ward marine stratigraphy in both troughs has been interpreted as trough mouth fans and wedges (Batchelor et al. 2013b, 2013a, Batchelor and Dowdeswell 2014). It is likely that the last ice streams followed pre-existing fluvially or glacially incised valleys. The mechanism of the original bathymetric depressions, which has been suggested to have formed during the late IpS (Fyles 1990; Manion 2017), has yet to be resolved. Several hypotheses for the creation (opening) of the inter-island channels have been proposed. Previous research suggested a fluvial dissection model followed by a subsequent glacial incision (Fortier and Morley 1956, Pelletier 1966, Fyles et al. 1991), while England (1987) suggested the channels may have been related to Cenozoic block faulting, producing a series of horsts and grabens. The fluvial and glacial incision hypothesis is supported by Manion's (2017) lithospheric flexure modeling results which demonstrate that the CAA topography and distribution of Bfm sediments can be best explained by flexural responses to marginal loading and subsequent incision of the straits and troughs during the Pleistocene. His model revealed a characteristic isostatic peripheral bulge parallel to and inland from the islands' coasts, which is reflected in the modern surface topography.

3.4 Methods

Our research is based on a detailed analysis of ION's BeaufortSPAN East, high-resolution 2D long-offset reconnaissance seismic reflection data (Figure 3.1B). While the ION airgun arrays and streamers were designed to image to the base of crust and were, therefore, less tuned to resolving the upper Late Cenozoic stratigraphy, its resolution was still much higher than any previous seismic records, and it included vast areas without any previous seismic coverage. Acquisition parameters included a streamer length of 9000 m with 360 channels, 18.4 s record intervals and a sample rate of around 2 ms. The data were acquired with a shot interval of 50 m (37.5 m in phase II of acquisition). We supplemented the ION grid data with older vintage seismic data (Pan-Arctic/Suncor) that had previously been scanned from paper records and converted to SEG-Y format (Figure 3.4, blue lines within M'Clure Strait and surrounding area).

Because there is no well-controlled chronostratigraphy, biostratigraphy or physical core data available for the Banks–Beaufort Basin IpS, we attempt to correlate with four onshore wells located on western Banks Island (Figure 3.1B). The interpretations of the two-way time seismic profiles were initially conducted with Kingdom Suite® software then finalized using custom freeware developed at the Geologic Survey of Canada based on non-lossy JPEG 2000 images from SEG-Y (Courtney 2007). A simple depth model applied in Kingdom Suite® could not be adopted to the JP2000 viewer, which applies a fixed velocity with depth. However, the depth model was incorporated where projections to land-based wells were performed.

Due to the difficulty in recognizing (or general lack of) unconformities or flooding surfaces within the marine succession, the conventional depositional sequence model suggested by Mitchum et al. (1977) and Vail et al. (1977) is unfeasible. Instead, the depositional model proposed by Frazier (1974), where hiatal surfaces (submarine unconformities) are used as bounding surfaces, was utilized, similar to the approach of Dixon et al. (1992) for the Beaufort–Mackenzie Basin. In practice, a seismic reflection or surface was chosen when it was distinct and regionally extensive across the study area. These key horizons were manually traced, exported as X,Y,Z coordinates at each shotpoint, purged for suitable display at map scale, and further purged for gridding purposes. A bin size of 100 inline by 100 crossline points (total 10,000 points) was deemed adequate for regional mapping.

Interpretation-annotated points and polylines exported to GIS-compatible shapefiles facilitated transcribing of profile interpretations to maps. Elevation and isopach maps were generated using these grids in ArcMap. Volumes were calculated by applying the cut-and-fill function, where the net gain or difference between the two grids corresponds with the volume between two surfaces. Volumes were then converted to MT using the density of wet packed sand (2.08 tonnes/m^3). This total weight was then divided by climatostratigraphic time interpretations to estimate sediment flux (MT/yr). This flux estimation does not consider sediment compaction, diagenetic or other changes in porosity, or sediment shunting beyond the studied volume, and therefore the estimation is a static model.

3.5 Results and Interpretations

3.5.1 Seismic facies

At the coarsest scale, the seismic profiles readily reveal that the IpS in the Banks–Beaufort Basin is composed of a singular, thick-seaward dipping and thickening aggradational wedge of sediment that extends far (>100 km) into the Canada Basin. This contrasts with its Beaufort–Mackenzie Basin equivalent, where multiple stacked progradational wedges are observed. The following six seismic facies (Table 3.1) are identified in the upper Banks–Beaufort Basin, based on geometry and characteristics of seismic reflections, including their amplitude and continuity (Sangree and Widmier 1979).

Discontinuous (Disc) Facies is characterized by reflections with very poor lateral continuity. The seismic amplitude is highly variable, with bursts of high amplitude reflections interspersed with medium to low amplitude reflections (Table 3.1, Figure 3.5). This facies has a paucity of internal geometric patterns at this resolution. *Interpretation:* This lithological assemblage has been interpreted as high energy discontinuous coarse clastics, with possibly some interfingering muds and organics, which would provide strong velocity contrasts and result in the variable amplitude reflections observed (Sangree and Widmier 1979). The sands may have lenses of interbedded organic, as the source (e.g., the BFm onshore) was composed of high abundances of peat and detrital material. These organics dispersed within the sands and muds could have also contributed to the observed high velocity contrasts. Preserved organics are commonly found in river-dominated delta fronts (Bhattacharya and Walker 1992). The variable high energy of fluvial and drift currents in the proximal marine realm could produce the discontinuous reflections within this facies (Sangree and Widmier 1979, Miall 1996). These sediments may have been deposited in a subaqueous distributary channel system. They could be associated with a proximal delta front environment, thin foresets may exist but are finer than the seismic resolution (< 25 m) (eg., Porębski and Steel 2003). The delta front environment is defined as the site where much of the delta's active deposition occurs, and the coarsest sediment is deposited (Bhattacharya and Walker 1992).

Continuous (Cont) Facies is acoustically well stratified and planar with continuous, slightly dipping (2-3°), medium- to high-amplitude reflections (Table 3.1, Figure 3.5). The high continuity of reflections in this facies suggests uniform depositional energy conditions across at least 10s of km, both in space and time. The high-amplitude character arises from acoustic impedance contrasts (density and velocity-dependent), but acoustic interference patterns can strongly alter reflector spacing, so relative thickness or proportions of fine versus coarser sediments are not inferred. *Interpretation:* The continuity and planar geometry suggest interbedding of mud with sands or silts. Sangree and Widmier (1979) have suggested that deposits with this facies could be associated with aggradational marine sediments, perhaps deposited in a medial to distal delta front environment. In river-dominated deltas, distal delta front facies have been reported to be well stratified (Bhattacharya and Walker 1992).

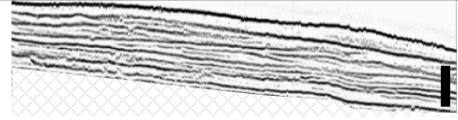

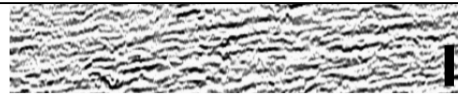

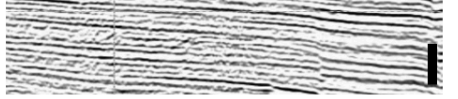

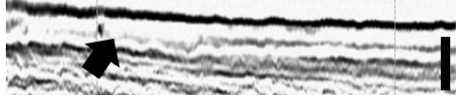

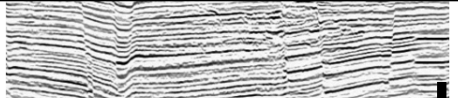

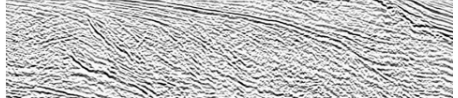

Glacial Erosion Surface (GES) Facies has a stratified seismic character with medium to high amplitude reflectors (Table 3.1, Figure 3.5). Continuous strata are recognized within this facies but are far less common than a progradational facies (e.g., *Cont* facies). The internal geometries show multiple stacked, sheet-like wedges bounded by high-amplitude reflections, often with angular unconformity (Table 3.1, Figure 3.5). *GES* is differentiated from *Cont* by its wedge geometry and medium-low amplitude dipping internal reflections, which have gradients of 0.1-1°. *Interpretation:* This facies is interpreted to be glacial (Wellner et al. 2001) and includes grounding zone wedges previously identified near the mouths of Amundsen and M'Clure glacial troughs (Batchelor et al. 2014).

Fault (Flt) Facies exhibits a similar seismic pattern as *Cont* facies, however, the presence of faults with observable displacement within *Flt* facies creates some differences (Table 3.1, Figure 3.5). Dipping reflectors and varying thicknesses across fault blocks suggest there are growth packages within this zone associated with syn-tectonic growth. Furthermore, acoustically chaotic reflections with varying amplitude are observed within some *Flt* facies elements. *Interpretation:* The chaotic zones within the fault blocks are interpreted to have resulted from sediment reorganization caused by slope instability or seismogenic processes. Lithological assemblages within *Flt* facies have been interpreted as interbedded sand and muds, similar to *Cont* facies.

Low frequency (LF) Facies is composed of diffuse low frequency seismic reflections that lack internal geometries (Table 3.1, Figure 3.5). These reflection-free zones may be attributable to near surface scattering or attenuation of the seismic signal. *Interpretation:* Because *LF* facies is only present in the shallow and proximal regions, this facies may be associated with shallow permafrost or shallow water acoustic interference (Ramachandran et al. 2011). Lithological assemblages therefore, cannot be discerned separately from within these zones.

Cliniform (Clin) Facies exhibit moderate to high amplitude continuous and dipping reflections (Table 3.1, Figure 3.5), which in some regions have complex sigmoid-oblique geometries, typically characteristic of high-energy depositional systems. The *Clin* facies sigmoid-oblique geometries are distinct from relatively shallower clinoform reflections with flat-lying planar tops observable within *GES* facies, especially around Amundsen Gulf. *Interpretation:* This pattern may be associated with clastic deltaic sediments found within prograding slope deposits in a channelized environment (Sangree and Widmier 1979, Dixon et al. 1992, McNeil et al. 2001). On the other hand, similar clinoforms observed by Rohr et al. (*submitted*) on the central Beaufort continental shelf were interpreted to be slope fan and proglacial sedimentation, providing an alternative interpretation for the origin of *Clin* facies.

Table 3.1. Illustrations of multiple seismic facies identified from 2D seismic profiles offshore Banks Island, NWT. Internal reflection geometries and frequency are described. Acronyms used in the main text and in the seismic facies maps are explained. Coloured bars under the acronym are associated with the facies maps illustrated in Figure 3.9. A summarized interpretation of the depositional environment is also reported. The black vertical bar is equal to 100m.

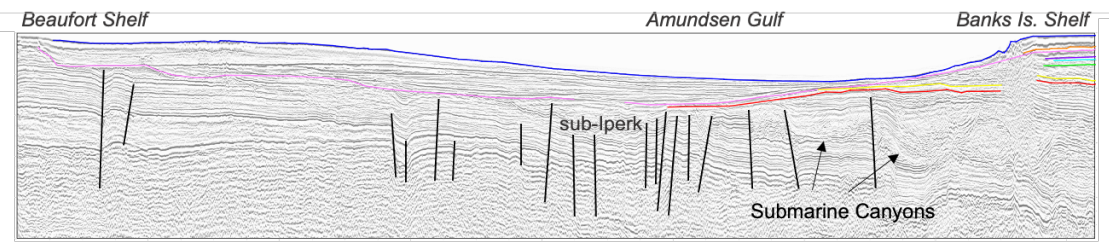
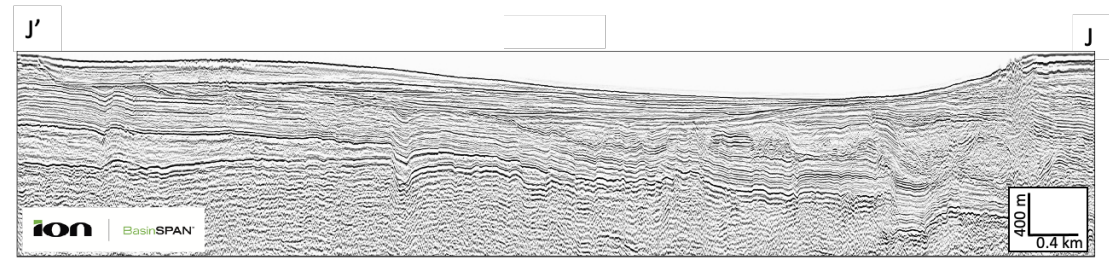
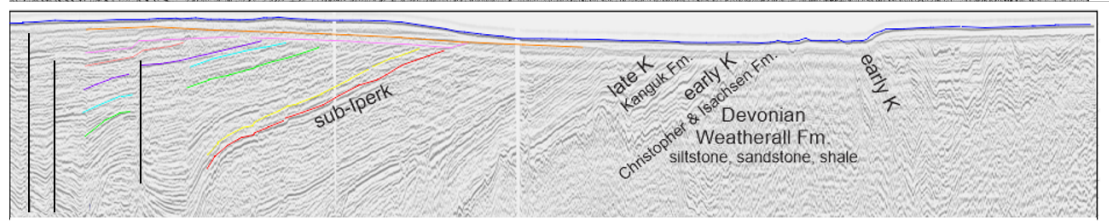
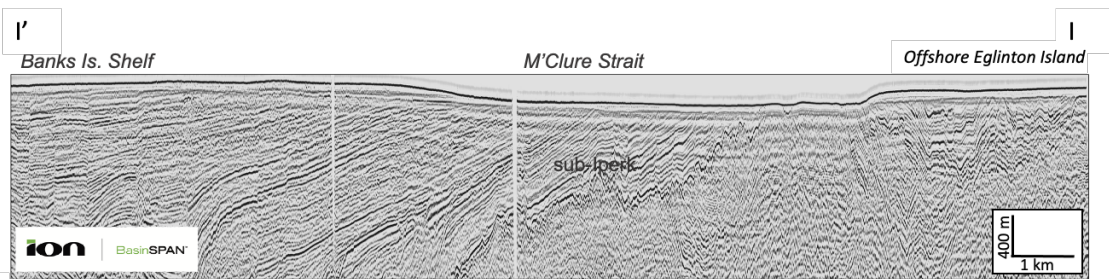
Seismic Facies	Acronym and colour in seismic facies map	Internal Reflections and amplitude	Geometries	Interpreted Depositional Environment
	GES 	Continuous, medium to high amplitude	Locally constructional, mounded, stacked wedges, basal and internal angular unconformities	Glacial Unit (erosional, tills, proglacial)
	Disc 	Discontinuous coherent, high amplitude	Irregular geometries	Proximal delta, high energy shallow marine deposits,
	Cont 	Continuous coherent, locally high amplitude, rhythmic	No internal geometries, planar	Medial to distal, delta front environment, lower energy
	LF 	Diffuse, low frequency (near surface scattering and/or attenuation)	No internal geometries	Shallow permafrost and/or suspected shallow water acoustic interference
	Flt 	Continuous, growth packages within fault zones	Fault dominated	Large listric normal growth faults
	Clin 	Continuous, dipping, moderate to high amplitude	Large clinoforms	Shelf break clinoforms, associated with large prograding slope deposits or canyon systems

3.5.2 Faulting

Consideration of any fault-related disturbances to the basinal stratigraphy must be considered while interpreting the seismostratigraphy. Faults are readily observed in the ION and vintage seismic data (*cf.* Harrison and Brent 2005, Kumar et al. 2009, Helwig et al. 2011).

Harrison and Brent (2005) mapped a series of faults paralleling the shelf break offshore Banks Island using historical seismic data. The ION data reveal many more faults, including a series of km-deep normal faults with ca. N-S orientations (Flt facies, Figure 3.9) that occur only on the mid to outer shelf, more than 100 km west of the present shoreline and increasing in frequency westward near and beyond the shelf break to the limit of our data interpretation on the upper slope. Several large listric faults are observed (e.g., Figure 3.5C-C') with single fault vertical displacements beyond 100 m and net offsets in fault systems often in the 100s of m. Most are high angle (steepness cannot be precisely calculated without time-distance and compaction models), shallowing seaward at depths of many km with synthetic and antithetic components and occasional hanging-wall basins where accommodation space is created. Some developed grabens but landward dips are far fewer. The majority of the largest faults extend several km into the brittle crust and are truncated by the Late Miocene unconformity and occasionally have displacements that increase with depth, which suggests the reactivation of older faults. Rare faults offset the entire IpS and even fewer exhibit a seabed expression, with most occurring within the listric fault zone on the Banks Island shelf. Some developed sufficient accommodation space on their down-throw side to accumulate local basins. Reverse fault systems are not recognized, and no evidence of large-scale folding is observed. These observations are consistent with a limited degree of extension by normal faulting in the Late Cenozoic due to the fault's short displacements and steepness. The highest frequency in the thickest part of the sequence near the shelf break may suggest that rapid loading caused by high sedimentation rates is an influence. This and the ubiquitous evidence of growth faults suggest these fault systems developed contemporaneously with sedimentation. Gravitational and lithospheric flexure processes may have a first-order role in the genesis and reactivation of the observed shelf edge and slope faults. Our understanding of the Late Cenozoic strain history of the Banks–Beaufort

Basin is insufficient to interpret fault kinematics, strain rates and partitioning, if any, and the cause of the faulting along the margin. A more thorough analysis that includes the entire post-rift sequence, decompacted with a precise velocity-depth model, is merited for future research. Potential fault scarp zones adjacent to the walls of the channels were explored (Figure 3.4) and no major faulting within these zones that would indicate post-Miocene graben or block-faulting formation of these inter-island channels were observed.



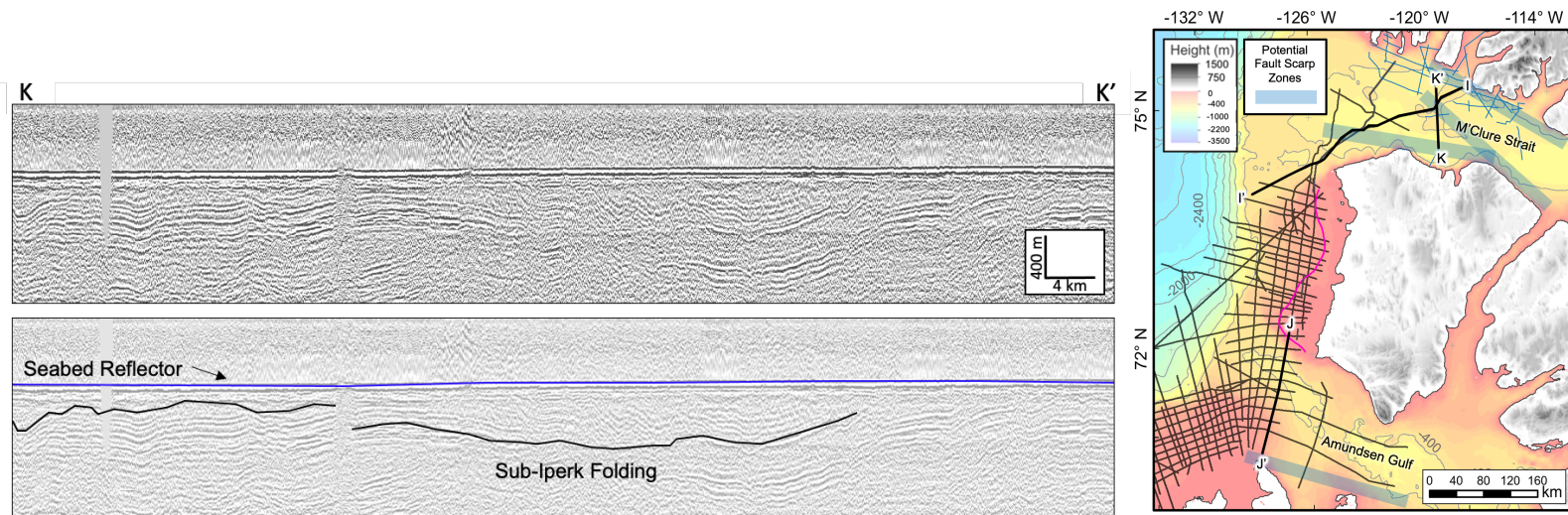
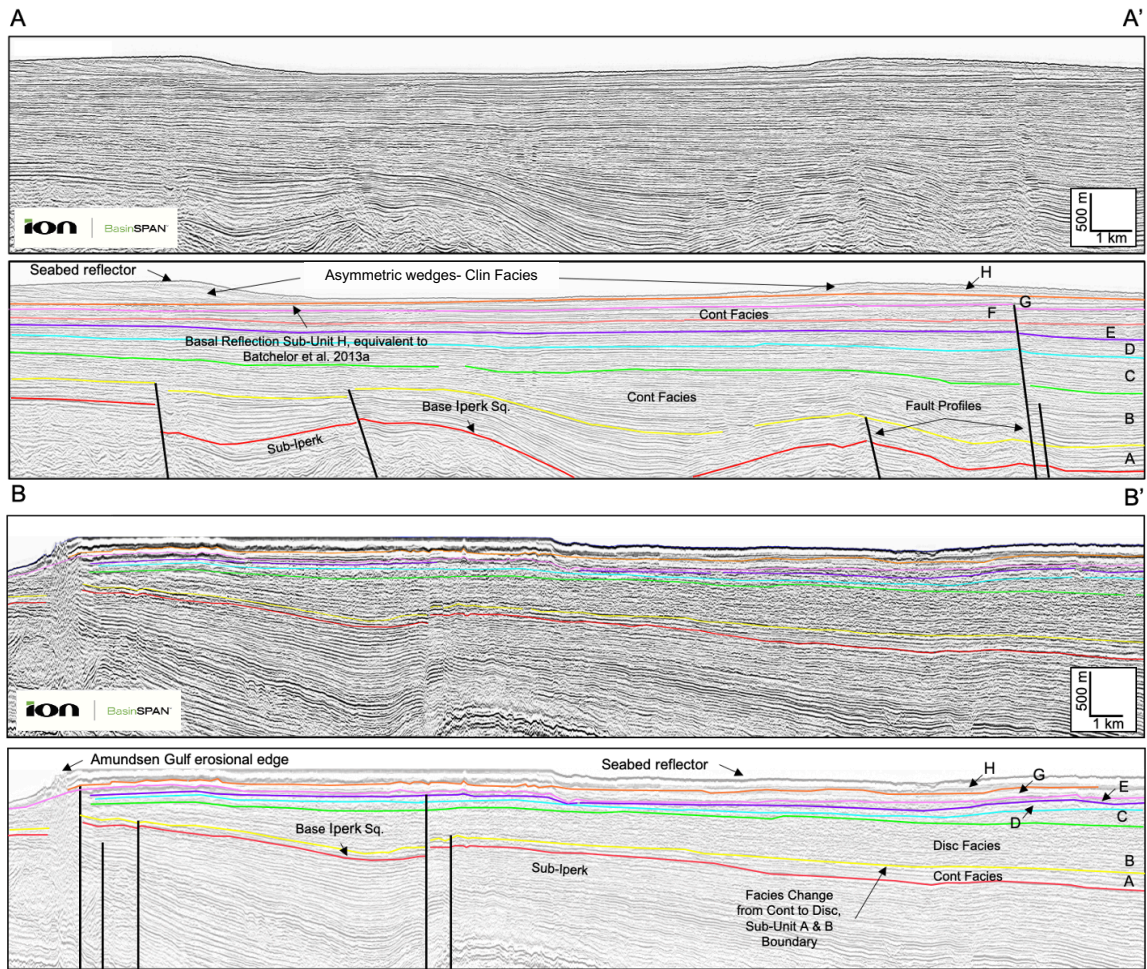


Figure 3.4. M'Clure Strait and Amundsen Gulf, with the light blue shading showing zones where potential fault scarps would occur if these channels were fault bounded. The two ION seismic lines (I-I' and J-J') and one legacy 2D seismic line (K-K') (Pan-Arctic/Suncor) show a representation of the seismic lines that cross perpendicular to the potential fault scarp zones.

3.5.3 Interpretation of Late Cenozoic seismostratigraphy

We used distinct, regionally mappable seismic reflections to define bounding unit reflectors and divide the sedimentary wedge above the sub-Iperk unconformity into eight units. These units are illustrated in four representative ION seismic profiles (Figure 3.5A-C, G). Figure 3.6D-D' is an inset of a shallow section of Figure 3.5C. The two margin-parallel profiles (Figure 3.5A, B) were shot 60 km and 150 km, respectively, from the modern Banks Island shoreline (Figure 3.1B). A margin-normal profile with westward dip (Figure 3.5C), located centrally on Banks Island shelf, is representative of a typical seaward dipping section on the Banks–Beaufort shelf. A profile (Figure 3.5G) extending from the south edge of Banks Island, across the southern shelf edge and into the flank of Amundsen Gulf, reveals key features related to glacial erosion and deposition at the trough mouths north and south of Banks Island shelf.



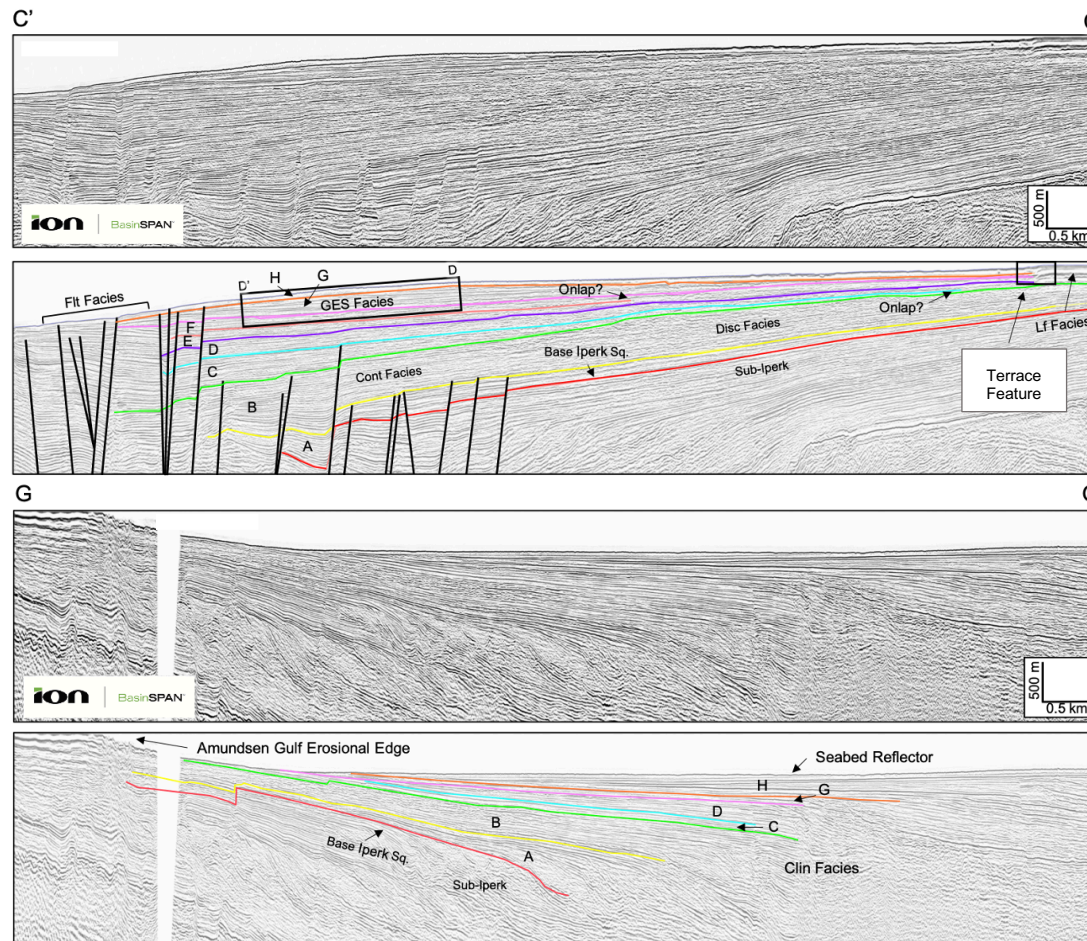


Figure 3.5. Uninterpreted and interpreted 2D seismic profile data from offshore Banks Island (courtesy of ION) (line locations shown on Figure 3.1B). The corresponding interpreted seismic sections (with coloured horizons) illustrate the distribution of eight seismic units (A-H) above the Late Miocene unconformity as well as examples of facies distributed throughout the section and other unique features present. The terrace feature indicated on C-C' is illustrated in more detail in Figure 3.11.

Sub-Iperk unconformity - Banks Island shelf (Red Coloured Line, Figure 3.5)

The upper and lower reflectors bounding this prominent pan-basin erosional contact are mostly parallel, although rare terminations confirm that it is a disconformity. This contrasts with the dominantly angular unconformities mappable throughout the Beaufort–Mackenzie Basin. From its continuous lateral extent and uniformity throughout the entire Banks–Beaufort Basin (Figure 3.7A), we infer that this disconformity should have regional significance and correlate with neighbouring basins and perhaps the coeval onshore record. We have correlated the disconformity to an unconformity noted in the well logs (Figure 3.3) of four onshore wells on Banks Island (Figure 3.1B). Furthermore, we have correlated the unconformity in the Banks–Beaufort Basin across Amundsen Gulf to a regional first-order sequence boundary in the Beaufort–Mackenzie Basin identified and termed the sub-Iperk unconformity by McNeil et al. (2001).

Unit A (Directly above sub-Iperk unconformity) (Red – Yellow Lines, Figure 3.5)

Unit A lies disconformably above the Late Miocene unconformity. Unit A has a mean thickness of 172 m, reaches a maximum thickness of 813 m (Figure 3.7), and an estimated sediment volume of $4.83 \times 10^{12} \text{ m}^3$ (Table 3.2, Figure 3.7B). This unit's thickness is mainly uniform within the Banks–Beaufort Basin, only varying in thickness within the listric fault zone (Figure 3.7B), where syn-tectonic growth likely impacted thickness. The top of this unit is delimited by a regionally strong mappable reflector and seismic facies contrast from the overlying unit.

Table 3.2. Physical attributes of the 8 offshore units interpreted within the extents of the ION seismic coverage in the Banks–Beaufort Basin, including mean thickness (m), max thickness (m), and volumes (m^3).

<i>Unit</i>	<i>Mean Thickness (m)</i>	<i>Max Thickness (m)</i>	<i>Volume (m³)</i>
	<i>m</i>	<i>m</i>	<i>m³</i>
Unit H	143	910	7.17E12
Unit G	111	966	4.68E12
Unit F	116	297	1.68E12
Unit E	94	218	1.42E12

<i>Unit</i>	<i>Mean Thickness (m)</i>	<i>Max Thickness (m)</i>	<i>Volume (m³)</i>
	<i>m</i>	<i>m</i>	<i>m³</i>
Unit D	135	366	2.93E5
Unit C	162	547	4.22E12
Unit B	397	994	1.08E13
Unit A	172	813	4.83E12

Unit A is composed of *Cont* facies in both the proximal and distal regions of Banks Island shelf and *Clin* facies along the northern flank of Amundsen Gulf (Figure 3.9A). *Cont* facies is interpreted here as interbedded sands and muds associated with a medial to distal delta front. The highly continuous reflections directly parallel the sub-Iperk unconformity (Figure 3.5C), suggestive of one or more long-lasting transgressive episodes. The *Clin* facies geometries in Amundsen Gulf, which dip towards the gulf in a northwest direction, are interpreted as high-energy prograding sand-dominant lithologies deposited on the shelf.

Unit B (Yellow – Green Lines, Figure 3.5)

Unit B has a mean thickness of 397 m and a maximum thickness of 993 m (location and character illustrated in Figure 3.7, Figure 3.8). It is the thickest unit interpreted in the basin (Table 3.2, Figure 3.7C). Thickness generally increases northeastward of the Banks–Beaufort Basin, suggesting the deepest part of the basin was in the northeast section. Seismic facies assemblages in this unit differ across the basin (Figure 3.9B, C). In Unit B’s southern and northern proximal zones, the lower half of the unit is composed of *Cont* facies (Figure 3.9B). *Cont* facies is not evident within the lower half of Unit B anywhere in the central Banks–Beaufort Basin (Figure 3.9B). Unit B’s upper half is entirely composed of *Disc* facies in the proximal shelf region (Figure 3.9C). *Disc* facies dominates until ca. 100 km beyond the modern shoreline, after which it interfingers with and transitions seaward to *Cont* facies and then *Flt* facies (see Figure 3.5, seismic section C-C’)

We have interpreted the proximal to distal transition from *Disc* facies to *Cont* facies as the transition from submarine channel sands found in the inner delta front to a lower

energy outer-delta front environment composed of sands and silts. Similar examples of this facies pattern have been described from seismic profiles in Pleistocene submarine fans in the western Gulf of Mexico (Bhattacharya and Walker 1992, Beaubouef and Friedmann 2000). In the proximal region of Banks Island shelf, inner delta front facies (*Disc* facies, Unit B) are deposited on top of distal delta front facies (*Cont* facies, Unit A) (Figure 3.9A, C). This up-section transition suggests that sea level may have regressed as these units were deposited.

Unit C (Green - Light Blue Lines, Figure 3.5), Unit D (Light Blue – Purple Lines, Figure 3.5), Unit E (Purple - Coral Red Lines, Figure 3.5), & Unit F (Coral Red – Pink Lines, Figure 3.5)

The mean thicknesses, total thicknesses, and volumes of Unit C through F are summarized in Table 3.2. These units occur as multiple stacked sheets which thicken westwards in a wedge-like geometry as they advance deeper into the basin (Figure 3.7D-F). Unit F's thickness is considered a minimum, as it is likely truncated by the overlying unconformity (base of Unit G). Each unit is separated by a distinct high amplitude regionally mappable reflector, which defines their basal surface. The uniform thickness pattern suggests that subsidence rates were similar to or less than sedimentation rates. A distinct hinge line occurs approximately 20 km from the modern-day shoreline, where all four units start to increase in thickness. The location is similar to the Inner Arctic Platform Hinge Line delimited by Dixon et al. (1992) in the Banks–Beaufort Basin.

The facies changes from Unit C to Unit F largely emulates the facies pattern within Unit B. In the proximal shelf area, these units are primarily composed of *Disc* facies, after which there is a transition to *Cont* facies deeper into the basin (Figure 3.7D-F). The transition zone from *Disc* to *Cont* facies in Units C to F occurs at a shallower depth than in the underlying Unit B. This could be due to a transgression in sea level or a subsidence rate greater than sea level change, depositing *Cont* facies (Unit C-F) on top of *Disc* facies (Unit B) at the same depth.

Unit G (Pink – Orange Lines, Figure 3.5), Unit H (Orange – Seabed (Dark Blue Lines, Figure 3.5)

Unit G has a mean thickness of 111 m, and Unit H has a mean thickness of 143 m (Table 3.2). However, Units G and H's thicknesses are non-uniform throughout the Banks–Beaufort Basin (Figure 3.7G, H). The units thicken toward Amundsen Gulf and M'Clure Strait from the shelf's interior to greater than 1000 m in some locations. Units G and H are predominantly composed of *GEF* facies and *LF* facies. The presence of the *LF* facies appears to relate to the shallow nature of these units. The low frequency may be related to the presence of permafrost or shallow water attenuation that reduced the seismic signal (Ramachandran et al. 2011, Riedel et al. 2017). Unit H can be correlated to the basal reflector of Batchelor et al. (2013a, 2013b, 2014), above which are interpreted to be glacigenic sediment, therefore supporting an interpretation that the GES facies is glacial in origin. The GES facies within Units G below Unit H suggests Unit G is an additional glacigenic unit below the basal unit identified by Batchelor et al. (2013a, 2013b, 2014). The presence of glacigenic sediments represents a significant change from the fluvio-deltaic depositional environments observed in the underlying units. This interpretation is strengthened by Units G and H's position above a high-amplitude angular unconformity on the north and south of the shelf. The unconformity truncates underlying reflections (Figure 3.5D) suggesting that ice masses eroding non-glacigenic and perhaps even previous glacigenic sediments. Similar examples of till-sheet erosion and preservation have been described from seismic profiles on the mid-Norwegian margin (Dowdeswell et al. 2007, Montelli et al. 2017).

At the mouth of Amundsen Gulf, Clin facies is present within Units G and H (Figure 3.6, Figure 3.9G, and Figure 3.9H). Its presence leads us to infer that sediment was moving through Amundsen Gulf and prograding in a seaward, northwesterly direction from the trough during some or most of the deposition of these units. Additionally, the combined thickness of Units G and H increases troughward from the shelf (Figure 3.8I), which are attributed to the presence of multiple large grounding zone wedges as proposed and described in detail by (Batchelor et al. 2013a, 2014). It is not clear whether the wedges are formed by ice marginal oscillations of ice streams during the Late Wisconsinan glaciation or represent multiple glaciations. These clinoforms systems are rare and occur in only small areas compared to the larger and more numerous clinoforms systems occurring throughout the Beaufort–Mackenzie Basin.

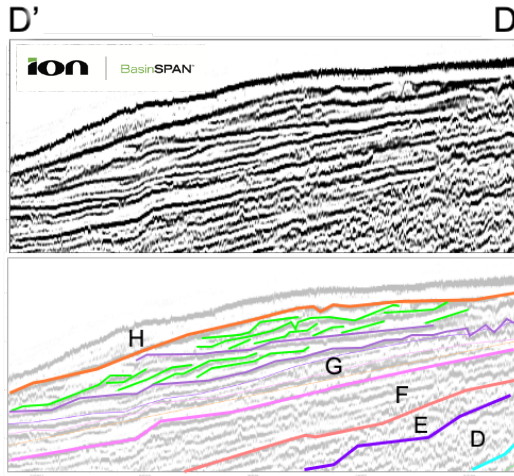


Figure 3.6. Uppermost Plio-Pleistocene Units D-H showing the internal structure of Unit G. The green lines trace coarse progradation in two sequences bounded by erosional surfaces (light pink line traces). This facies is typical of grounding zone wedges where the upper contact marks erosion by the glacier sole as it advances across sub-or pro-glacial foresets. Unit G contrasts with the constructional geometry and lack of coherent reflectors, typical of a till signature.

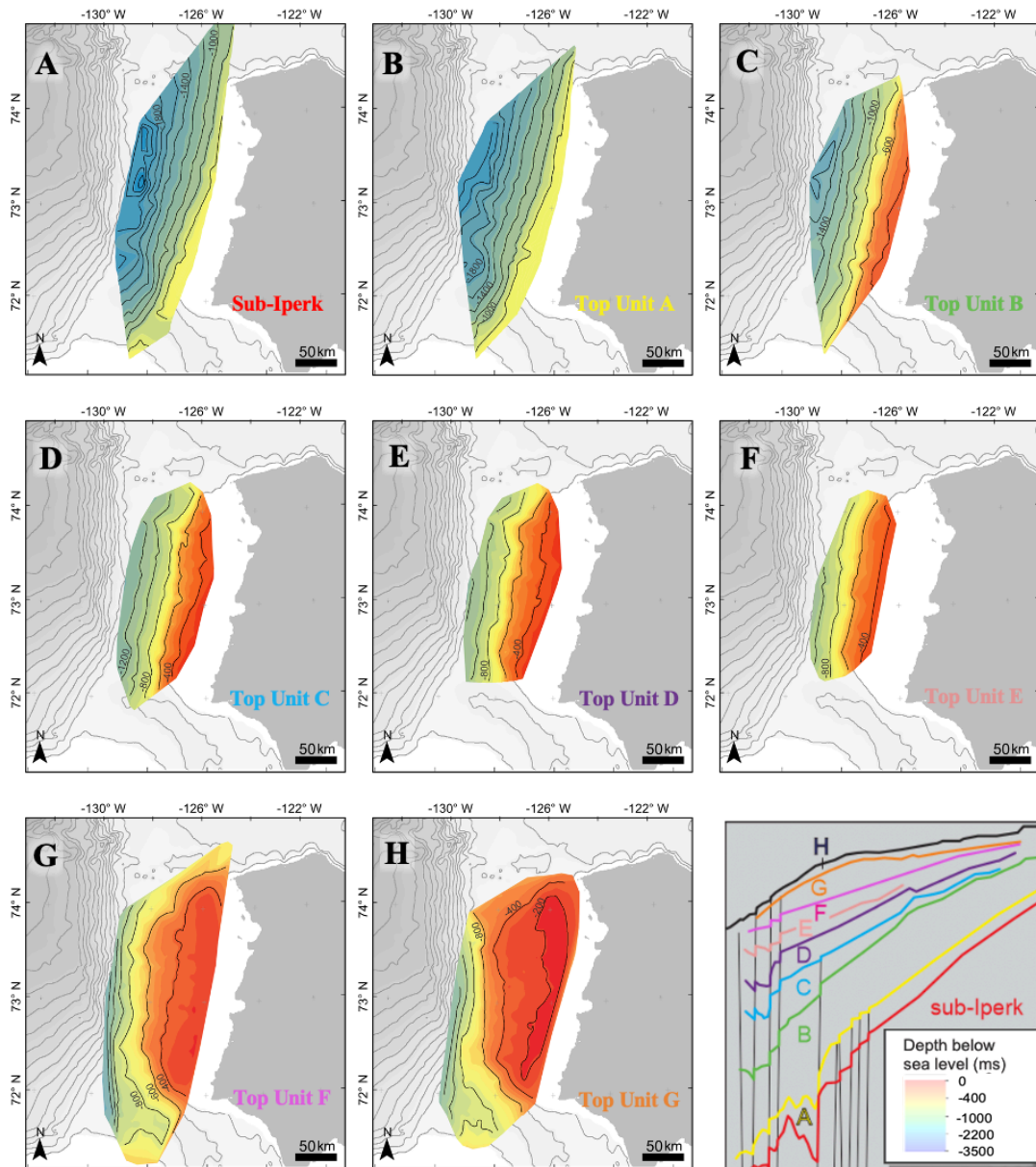


Figure 3.7 A-H. Contoured elevation maps of multiple interpreted surfaces on Banks Island shelf, overlying GEBCO sea floor bathymetry (200 m contours). All maps have the same scale bar and are contoured at 200 m. The specific interpreted surface (unit name colours correspond with surfaces from Figure 3.5) of each elevation map are as follows. Figure 3.7A: sub-Iperk unconformity. Figure 3.7B: Yellow interpreted surface, top of Unit A. Figure 3.7C: Green interpreted surface, top of Unit B. Figure 3.7D: Light Blue interpreted surface, top of Unit C. Figure 3.7E: Purple interpreted surface, top of Unit D. Figure 3.7F: Coral red interpreted surface, top of Unit E. Figure 3.7G: Pink interpreted surface, Top Unit F. Figure 3.7H: Orange interpreted surface, Top Unit G

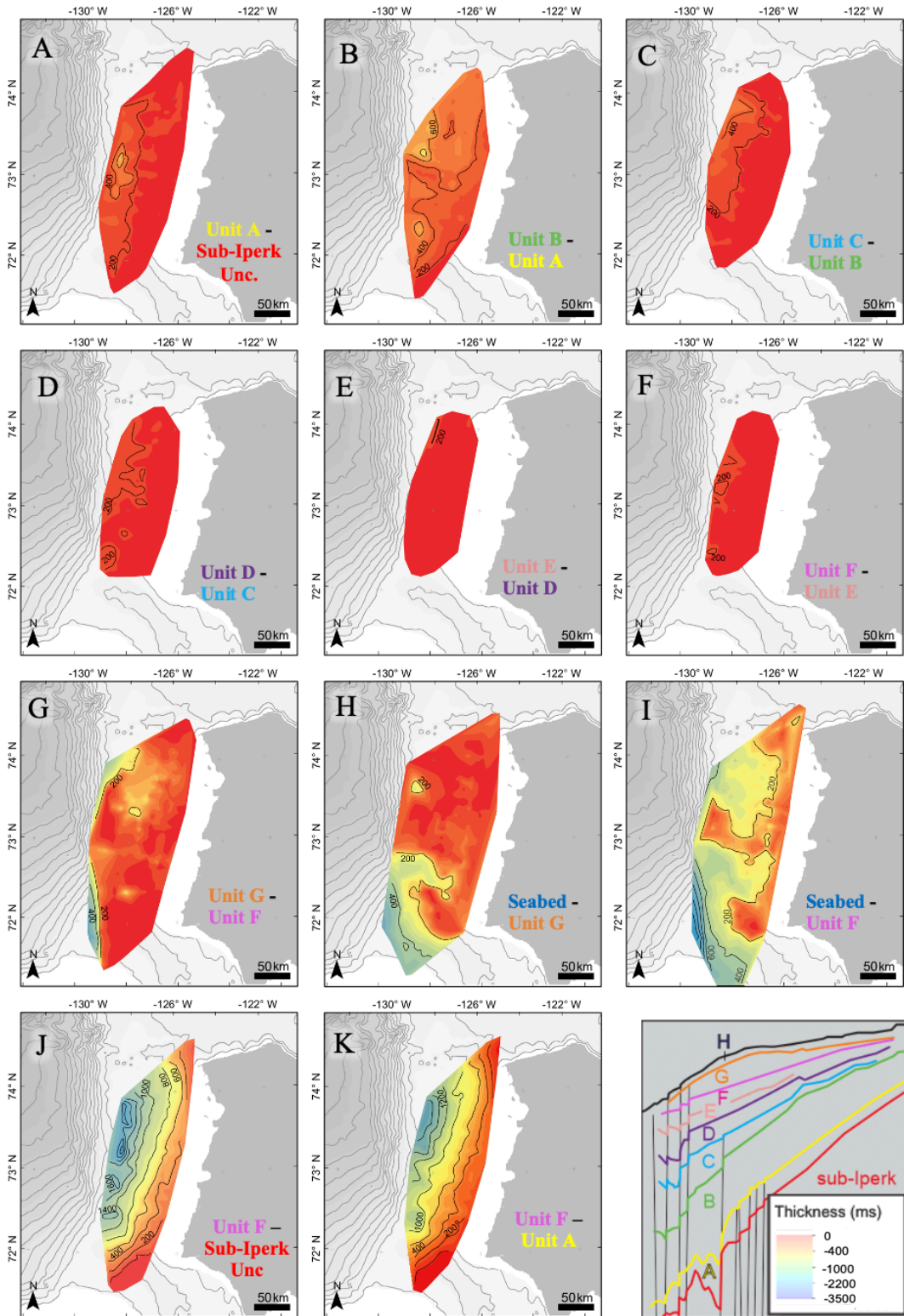


Figure 3.8 A-K: Contoured isopach maps of interpreted surfaces on Banks Island shelf, overlying GEBCO sea floor bathymetry (200 m contours). All maps have the same scale bar and are contoured at 200 ms.

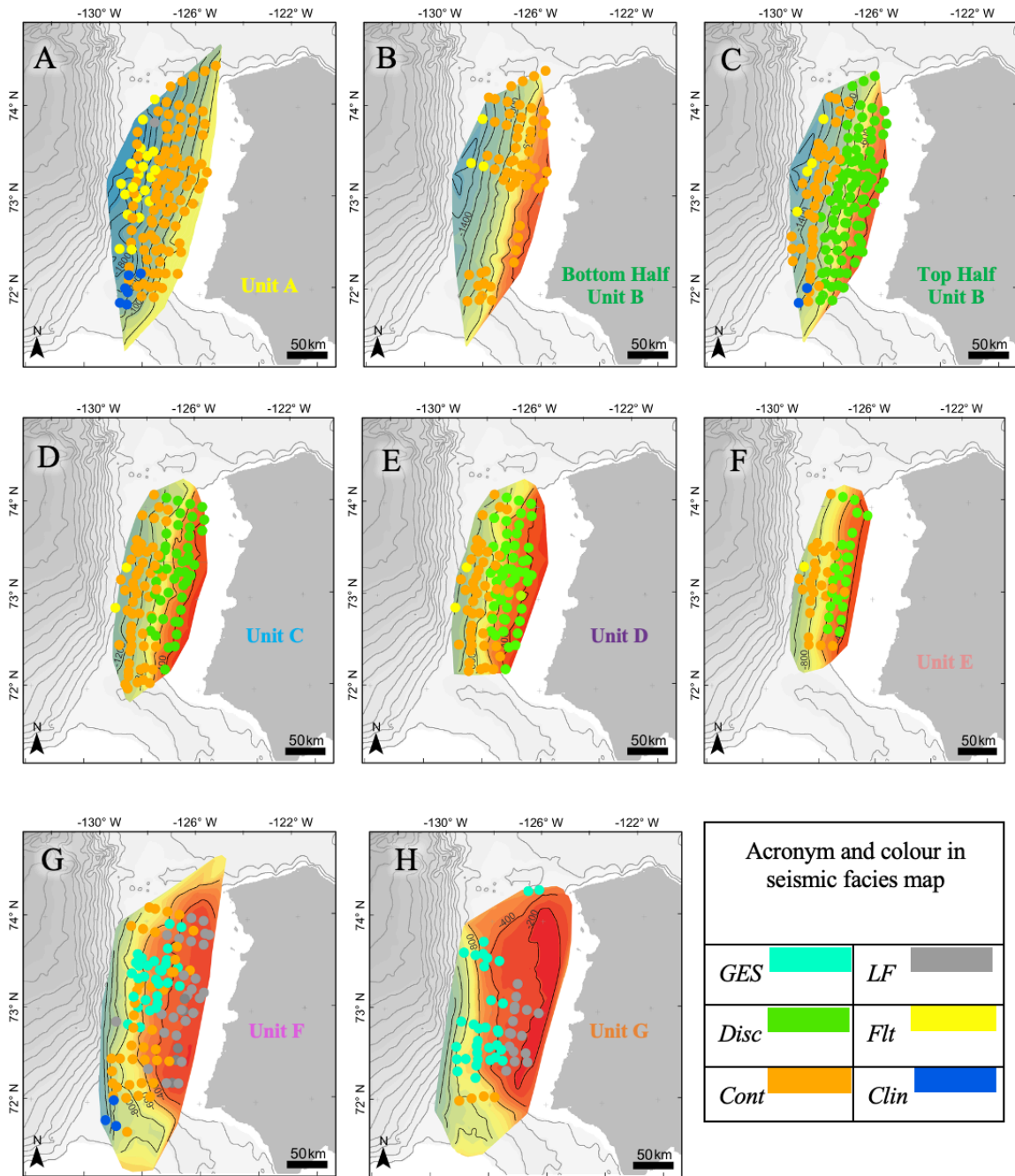


Figure 3.9. A-H: Facies maps overlain on top of contoured elevation maps, displayed in Figure 3.7 and GEBCO sea floor bathymetry (200m contours). All maps have the same scale bar. The colours of the dots represent different facies outlined in Table 3.1. Figure 3.9A: Facies of Unit A. Figure 3.9B: Facies of the lower part of Unit B. Figure 3.9C: Facies within the upper part of Unit B. Figure 3.9D: Facies within Unit C. Figure 3.9E: Facies within Unit D. Figure 3.9F: Facies within Unit E. Figure 3.9G: Facies within Unit G. Figure 3.9H: Facies within Unit H.

3.5.4 Correlations with the Slope and Canada Basin

Correlation between the deep-water stratigraphy of the Beaufort–Mackenzie Basin IpS (Dixon et al. 1992) and time equivalent units in the Banks–Beaufort Basin is established via a bridging seismic profile that connects the two slopes across the mid to outer Amundsen Gulf. Batchelor et al. (2014) first identified an Amundsen Gulf fan that extends outward from the Amundsen trough mouth (Figure 3.10). Units A-F extended onto the slope and the megasequences originally interpreted by Batchelor et al. (2014) are presented in Figure 3.10. Dixon et al. (1992) resolved multiple large hiatus-bound slope failure deposits comprising over 85% of the upper ~ 2.5 km IpS in the deep basinal region of the paleo-Mackenzie slope. These mass transport complexes extend laterally well beyond seismic coverage but originate almost entirely from the shelf edge and upper slope of the Beaufort–Mackenzie Basin margin (Mosher et al. 2012). Where they meet the distal slope and the Banks–Beaufort Basin IpS equivalents, the relationship is mainly onlap (Figure 3.10E-E’). This implies the glacial sediments from the Mackenzie Delta and Amundsen Gulf, which source the Beaufort–Mackenzie basin slope deposits, are overwhelmingly more volumetric than the equivalent Banks–Beaufort Basin sediments during a similar time period.

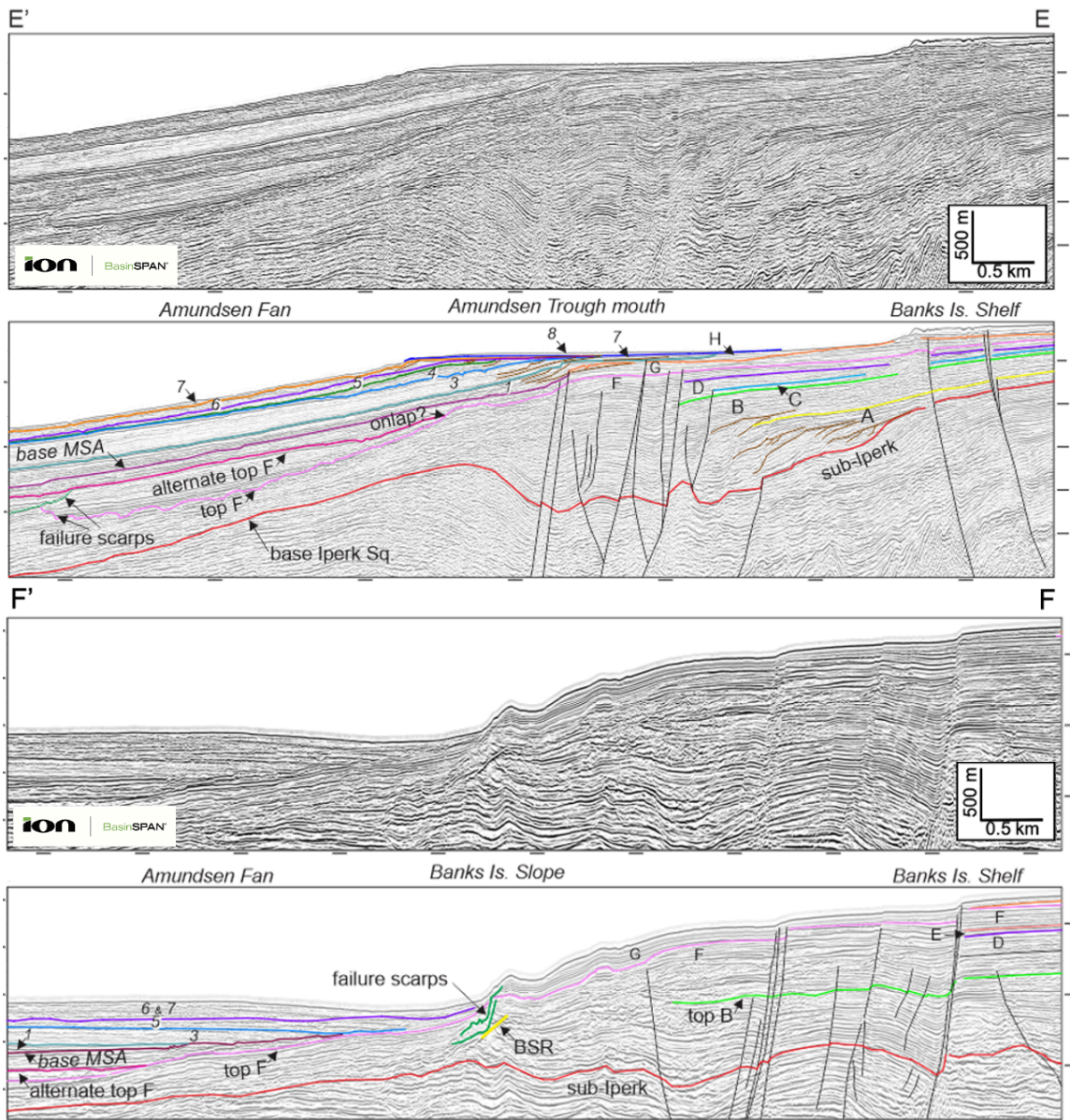


Figure 3.10 Seismic images (courtesy of ION) indicating relations of units within deep water. These include the Batchelor (2013b) sequences (numbered 1-8) and megasequence picks, the new base of Iperk picks (red), faulting that is present in the deep water offshore, and the deep water extension of Unit G (initial glaciation). Locations of seismic line are shown in Figure 3.1B.

3.5.5 A late-stage inner shelf terrace: a possible expression of paleo-coastal systems

A marked terrace at the seabed extends across the entire inner shelf offshore Banks Island. It was first identified through very limited, very high resolution (sub-meter) sub-bottom profiler transects supplemented with profiles generated from the GEBCO

bathymetric grid (1 km spacing). This terrace comprises a sharp change of slope from a seaward tilting plane (1:1000 gradient, 0.05°) to a steeper face (1:20 gradient, 2.8°) with the break in slope strongly constrained to between 35 and 41 m below present water depth (King et al. 2014). Prograding elements dominate, truncated by a distinct angular unconformity and multi-generational channel cut and fill (to 65 m below present sea level) in a sedimentary wedge ranging from 25 to 50 m thick at the slope break (Figure 3.11C and zoom boxes), all attributed to one or more low stands of sea level. No trends in the north to south flexure or warping of the terrace are recognized. No such submarine terrace equivalents are known on other shelf areas of the CAA.

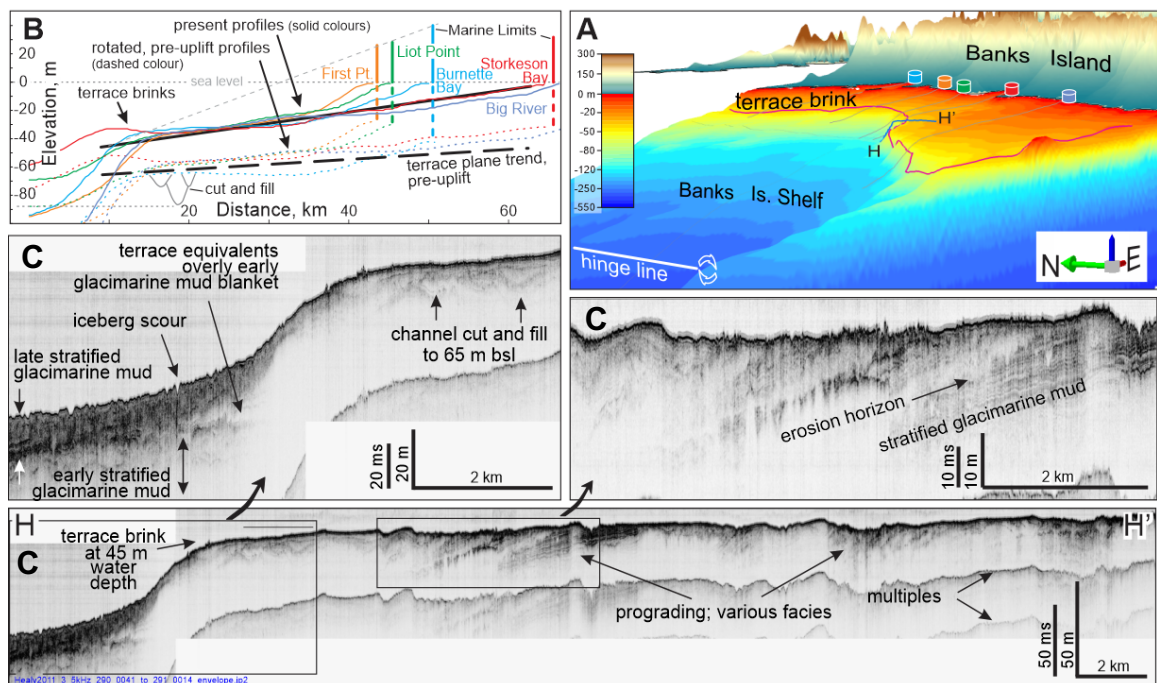


Figure 3.11. Inner Banks Island shelf and westernmost Banks Island topography and seismic imagery. Panel A (from GEBCO) is a 3-D rendered viewed from the SW with extreme vertical exaggeration showing an oblique image of the offshore terrace dipping slightly seaward (west) in orange tones (magenta line traces the brink). The green arrow points north. Panel B shows selected GEBCO-derived bathymetric profiles (solid-coloured lines) across the offshore terrace. Coloured vertical columns depict elevation at selected measured marine limit (ML) sites from Lakeman and England (2013) (site locations are near the present shoreline as depicted with coloured columns in Panel A). The modern terrace tilts uniformly seaward, interrupted by a steeper nearshore face (grey trendline). Dashed coloured lines are reconstructed versions of the corresponding solid bathymetric profiles but each is rotated to remove some component of glacio-

isostatic uplift about a hinge-line at the shelf break (140 km west) by the minimum amount to bring the coastal ML sites back to sea level. This brings the terrace to a flatter incline (thick dashed line) at a sea level lowered by at least -70 m. Panels C: a high-resolution sub-bottom profile, along H - H'. The lowest panel corresponds to the transect on Panel A, with two zoom inserts, depicting the terrace with interfingering stratified mud at its distal extent, the flat planar surface, and internal prograding of multiple facies.

Figure 3.11A shows the trace of the terrace across the shelf (also in Figure 3.1), and panel C shows the foreset face and various internal acoustic facies, including elements such as dipping stratified mud, alternating with chaotic (discontinuous) beds with erosional lower contacts. A coarse, prograding nature is seen in several similar sub-bottom profiles spanning south to north on the Banks Island shelf. The foresets are unstratified in Figure 3.11, demonstrating interfingering with an extensive blanket of stratified deposits seaward of the terrace, interpreted as (distal) glacimarine mud.

The planar-topped terrace geometry and internal prograding elements are indicators of a limited accommodation space governed by a lower sea level. Towards establishing an association with glacial low-stand(s) and age, a terrace elevation reconstruction scenario is presented (Figure 3.1, panel B). A partial compensation for post-glacial isostatic uplift is constrained by western Banks Island coastal marine limits (ML) recorded by delta and littoral features following glacial retreat identified by Lakeman and England (2013). Assuming an offshore hinge line at the shelf break, near the ocean-continental crustal transition (Figure 3.1, panel A), and using the minimal crustal depression offered by the ML elevations, the terrace plane is rotated to a flatter orientation and lower elevation. The extent and timing of the last glacial maximum were recently indicated to have lain in the marine realm in a limited but unknown distance beyond the coast (England et al., 2009; Lakeman and England 2013). The isostatic reconstruction sets the terrace brink at about -70 m paleoelevation but the coastal MLs constrain only a minimum elevation. A further assumption that the channel cut and fill near the western edge of the terrace is sea level governed (not sub-glacial) adds a further -20 m (again a minimum) to the lowstand, coming to a ca. -90 m lowstand.

Stratigraphic relations of the terrace deposit with the glacial deposits covering the mid and outer Banks Island shelf (Units G and H) are not well established for lack of resolution in the ION data. Neither is direct age assignment possible. Sands and silts below the ML yield mollusk radiocarbon ages predating the LGM (Lakeman and England 2014) and are assumed to be reworked but if they top the terrace or instead, comprise its proximal part, cannot be resolved. Nevertheless, if they correlate with portions of the offshore terrace, it may have been built up prior to the LGM. It raises the possibility that such analogues may have existed in the early and mid-Pleistocene.

Analogous lowstand features (terraces or unconformities) are not recognized within the deeper IpS. The small size of the terrace in relation to the ION seismic profiles (e.g., Figure 3.5C-C') demonstrates that it is challenging to recognize such units at the larger scale of the ION data. Similarly, that the terrace's internal features are unresolvable in the ION data serves to illustrate that there are other complexities and finer elements within the IpS that are unresolvable. Furthermore, artifact multiples and degraded primary wave signatures impede the observation of such elements in shallow water sections of the seismic profiles. This does not preclude such features in the medial to distal shelf within the deeper IpS, but should they exist, they are likely below the surficial terrace or landward of the seismic coverage.

3.6 Discussion

Using distinct, regionally mappable seismic reflections to define basal reflectors throughout the Banks–Beaufort Basin, the sedimentary wedge above the sub-Iperk unconformity was subdivided into eight units. The results indicate that while some similarities to the Beaufort–Mackenzie basin IpS exist, key differences limit the latter's use as an analogue for the Pliocene and Quaternary strata offshore Banks Island, and by morphological extension, the CAA. Benefitting from the relatively high resolution of the ION data (as compared to much of the available historical 2D seismic from the 70s and 80s), we have gained perspective on the Late Cenozoic depositional and erosional history in an area sensitive to a dramatic polar-amplified climate change and differences in the tectonic evolution of source regions.

3.6.1 Comparison of Beaufort–Mackenzie and Banks–Beaufort Basins Iperk Sequences

The IpS was considered a single contiguous wedge complex that extended well over a thousand kilometres along the Canadian Beaufort continental shelf from the Beaufort–Mackenzie Basin in the west to the Banks–Beaufort Basin (Dixon et al. 1992). Although stratigraphy underlying the IpS had distinctly separate depocentres in both basins (Dixon et al. 1992), the IpS was considered by and large to be a delta-dominated system that experienced relatively less regional tectonic influence, and instead, reflected more influence of thermal subsidence of the Beaufort-Sea and eastern Canada Basin margins (Dixon et al. 2019).

There are several tectonomorphic and stratigraphic similarities between both regions. Both basins received significant volumes of Pliocene sediment, and consequently, the upper shelf and slopes in both regions are largely defined by the IpS. The sub-Iperk unconformity is ubiquitous and recognizable across both basins, and evidence of tectonic deformation largely ceases after it. The IpS consists of both preglacial and glacial components. The preglacial component of the IpS is dominated by delta progradation. The increase in sediment flux during the Pliocene in both basins was at least partly climatogenic in the Beaufort–Mackenzie Basin but this seems to have played a significant role in the Banks–Beaufort Basin.

Differences in the Cenozoic sequences of both basins are attributable to a different influence of post-rift tectonics and different degrees of impact of glacial processes. In the Paleogene through Neogene, the Beaufort–Mackenzie Basin was significantly influenced by exhumation and drainage changes caused by uplift in mountain ranges to the south and southwest, including the Mackenzie and Richardson mountains. By contrast, the Banks–Beaufort Basin was likely sourced from much lower relief regions to the east (Miall 1979, Fyles 1990, Fyles et al. 1994, Braschi 2015), where broad fluvial systems drained off a contiguous landscape.

There are other compositional differences. In the Beaufort–Mackenzie Basin, the IpS consists of basal turbidite fills overlain by slope facies and subsequently by delta and shelf deposits composed of large distinct sigmoid-oblique clinofolds (Jones et al. 1980, Blasco et al. 1990, Dixon et al. 1992). Delta front and delta plain sediments cap the

sequence (Blasco et al. 1990). In contrast, there are no deep water basal turbidite deposits in the proximal region of the Banks–Beaufort Basin. Instead, delta front sediments lie directly above the sub-Iperk unconformity and the sequence is capped by glacial sediments (Figure 3.5, Figure 3.6). A distinct difference is the apparent lack of large-scale sigmoid-oblique clinoforms within the Banks–Beaufort Basin, even though they are very resolvable within the Beaufort–Mackenzie Basin. New evidence for ice-contact and glacial processes on the distal Banks Island shelf is another significant difference.

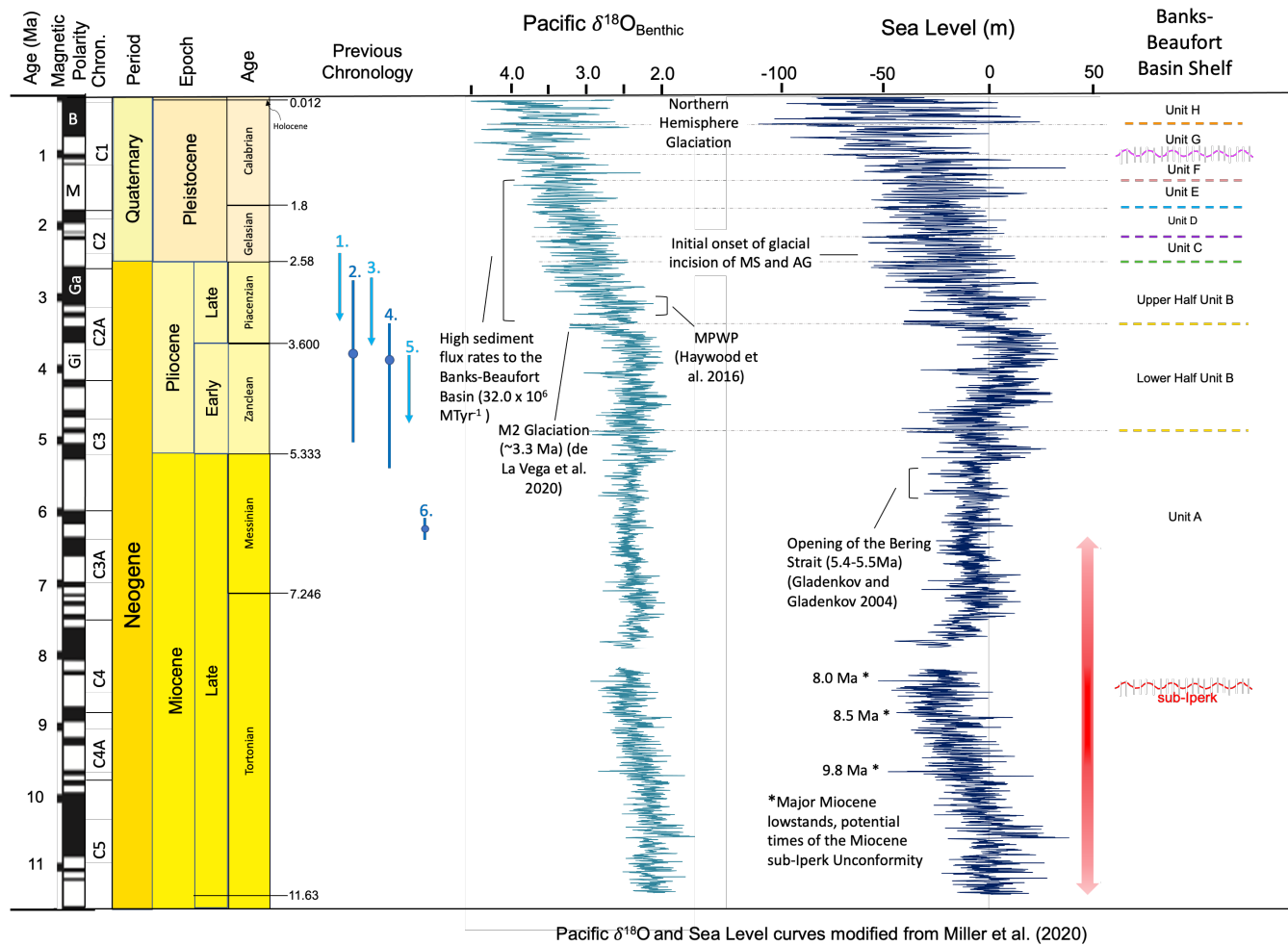
3.6.2 Late Cenozoic Chronostratigraphy in the Banks–Beaufort Basin

The units interpreted within the IpS can be crudely attributed to climate in order to form a ‘climatostratigraphy’ of the offshore sedimentation. This exercise is illustrated in Figure 3.12, where the units of the IpS are associated with major lowstands or significant changes to climate. By doing so, we can assign tentative interpretive ages to the IpS units.

In the Banks–Beaufort Basin, the base of the Late Cenozoic sedimentation starts with the sub-Iperk unconformity which appears as a high-amplitude reflection across the entire shelf. We are confident in our correlation of this unconformity across Amundsen Gulf to that previously defined in the Beaufort–Mackenzie Basin and Mackenzie Delta (McNeil et al. 2001). Several data sources (e.g., strontium isotopes, radiometric data, palynomorphs, and foraminifera) have been used to suggest that the sub-Iperk unconformity in the Mackenzie Delta was initiated during or at the end of the Messinian (~5.3 Ma; McNeil et al. 2001). However, the TCN isochron age presented in Chapter 2 ($6.20 \pm 0.20(1\sigma)$ Ma) provides a minimum-limiting age for the base of the offshore stratigraphy of the IpS. There are also three major lowstands in the Tortonian, which could be related to the Late Miocene unconformity and are older than the TCN isochron age of the BFm onshore. We have tentatively placed the base of the IpS at the lowstand at 8.0 Ma (Figure 3.12), but it could be older or as young as 6.20 Ma.

The Late Tortonian global lowstand was followed by a protracted transgression during the Messinian (Miller et al. 2020). The consequent accommodation resulted in basin aggradation to form the present-day shelf and slope throughout the Beaufort Sea. The sequence of medial to distal delta front deposits of Unit A overlying the sub-Iperk unconformity may have been deposited during this period of relative climate stability,

with low-amplitude orbital forcing (Figure 3.12). Unit A records *Cont* facies throughout the unit, which could be associated with lower energy, distal delta front environments. The landscape may have been an erosion-limited but weathering-prone environment when climate was relatively warm and stable, resulting in low sediment flux rates to the basin, which may have resulted in the lesser thickness of Unit A compared to other units above it.



Pacific $\delta^{18}O$ and Sea Level curves modified from Miller et al. (2020)

Figure 3.12. Climastratigraphy of the Iperk Sequence, built upon Figure 1.2, illustrates a geological time scale, Pacific $\delta^{18}O_{\text{Benthic}}$ through time, a proxy for temperature, and sea level (m) through time, modified from Miller et al. (2020). Sea level at 0 m is present day. Symbols for the

magnetic polarity chrons are as follows: B: Brunhes (<0.78 Ma); M: Matuyama (0.78-2.59 Ma); Ga: Gauss (2.59-3.59 Ma); and Gi: Gilbert (3.59-5.25 Ma). On the far right, the climatostratigraphic units of the IpS within the Banks–Beaufort Basin shelf are depicted. On the left column are previous chronologies of the BFm across the CAA, including the new TCN isochron burial age reported in Chapter 2 (number 6.). Previous Chronologies (at left) of the BFm across the CAA, including the new TCN isochron burial age from Prince Patrick Island reported in Chapter 2 (number 6.). Other reported ages are as follows: 1: AAR Ages (Brigham-Grette and Carter 1992); 2: Sr isotope dating (Kaufman et al. 1993) 3: TCN ‘simple’ burial age Banks Island (Braschi 2015); 4: TCN ‘simple’ burial age Beaver Pond Site (Fletcher et al. 2018) 5: TCN ‘simple’ burial age Fyles Leaf Bed (Rybczynski et al. 2013).

Global and regional cooling began at the end of the Zanclean (3.6 Ma) based on (i) $\delta^{18}\text{O}$ from benthic and planktonic foraminifera (Lisiecki and Raymo 2005); (ii) a significant gradual drop in global sea level (>50 m Miller et al. 2020) (Figure 3.12); (iii) summer insolation at High arctic latitudes (e.g., Rybczynski et al., 2013); and (iv) the onset of Northern Hemisphere glaciation (Bartoli et al. 2005). The effects of global climate deterioration were likely amplified in the polar regions (Ballantyne et al. 2010, Csank et al. 2011), causing degradation of arctic forests, initiation, or thickening of permafrost (ice wedge casts are observed in the upper White Channel Gravel of Yukon and in the equivalent-age terrace gravels in central Ellesmere Island (Rybczynski et al. 2013), and a higher sediment flux from a deeply-weathered arctic landscape. The short-lived M2 glaciation occurred during this time period at ca. 3.3 Ma (Figure 3.12) and may have contributed additional sediment flux. The Banks–Beaufort Basin may have captured this climatogenic evolution with the basin. In a 40 m thick BFm section on northwestern Banks Island, Braschi (2015) reports observing a 1m thick pebble gravel, at least 10 m below the eroded top of the formation. No evidence for the passage of grounded ice is recorded (depositional or erosional), thus distinguishing these gravels from later Pleistocene glaciations. The gravel sorting, colour, and the occurrence of faceted and striated clasts make it distinct from the BFm above and below it. Braschi (2015) reports a tentative age of >2.8 Ma for the BFm for this section based on $^{26}\text{Al}/^{10}\text{Be}$ burial dating of ten sand samples collected throughout the riverbank sections above and below the striated clasts. From this, Braschi (2015) inferred that the glacial gravels may be proximal glaciofluvial outwash corresponding to the M2 glaciation (3.3 Ma). Further, a single 0.5 m diameter quartzite boulder surrounded by detrital organics was observed in situ by Fyles et al. (1994), stratigraphically above Braschi's (2015) pebble gravel bed. It was suggested that this boulder had slumped onto aufeis and then was rafted into place. Regardless, the proximal advance of glacial ice (from a later glaciation than that identified by Braschi (2015) would be the only way to transport such a large clast into this region. Proximal glaciations would similarly be required to account for Canadian Shield granite clasts within BFm sediments, sourced from outcrops >900 km to the east or south (Miall 1979, Devaney 1991).

Offshore, Units B through F, which are interpreted as intervals of proximal delta front environments, could be the accretion of significant amounts of glaciofluvial sediments due to the first occurrence and advance of glaciations in the region (Figure 3.12). Unit B in particular, which has a larger thickness relative to other units (Table 3.2) and is composed of the first observed occurrence of *Disc* Facies in the upper portion of the unit, could reflect an initial purge of unconsolidated sediment from the large regional catchment during the onset of glaciation(s). The significant differences between the facies of underlying Unit A and the upper portion of Unit B above suggest that a change to sedimentation must have occurred in the basin. The onset of glaciation is a possibility that could explain this change.

Units C-F were likely deposited as climate continued to cool and glacial periods occurred with more frequency. No major erosional boundaries are observed within these units, therefore, correlation with specific glacial periods remains challenging. Additionally, it is challenging to correlate which portion of Unit C-F is coeval with the onshore portion of the Bfm. These units likely illustrate a more complete section than what remains of the Bfm onshore. Recognizing these limitations, we have tentatively assigned Units C-F to major lowstands throughout the Late Pliocene and Pleistocene (Figure 3.12), which may have formed the boundaries between these units.

Major continental glaciations were restricted to the last 1- 0.8 Ma or less, with Marine Isotope Stage 22 (870-880 ka) coinciding with the first major worldwide glacial events and large ice volumes (Ehlers and Gibbard 2007). Based on this record, the base of Unit G could be correlative with the onset of these large northern hemisphere glaciations around 1 Ma. At Duck Hawk Bluffs on southwestern Banks Island, the oldest glacial deposits are glaciofluvial outwash gravels which are paleomagnetically reversed (>0.78 Ma, possibly Matuyama Chron, Evans et al. 2014). This was capped by additional glacial sedimentation including till, that has a magnetically normal signature (<0.78 Ma, possibly Late Wisconsinan). These lower magnetically reversed glacial deposits could be related to Units G or H.

While the extent of Late Pleistocene glaciers and their dynamics in the western CAA remains largely unconstrained, there is general agreement that the Laurentide Ice Sheet

covered Banks Island during the Late Wisconsinan LGM (25–21 ka)(England et al. 2009, Lakeman and England 2014). Its extent across the shelf remains uncertain. Numerous authors place ice streams in Amundsen Gulf and M’Clure Strait at this time (e.g. Stokes et al. 2005, Batchelor et al. 2013a, Jakobsson et al. 2014, Lakeman et al. 2018). In addition to grounding zone wedges near the mouths of these troughs, evidence of multiple glaciations, subglacial erosion, and glaciofluvial incision and deposition is observed on the shelf and upper slope. Unit H is relatively thin on the Banks Island shelf, with the exception of two lateral moraines (identified by Batchelor et al. 2014), and thickens extensively out of Amundsen Gulf (Batchelor et al. 2013a, 2014, Jakobsson et al. 2014). Unit H may have been deposited <0.78 Ma or earlier during the last glacial maximum when the LIS covered Banks Island.

Unit H, which is composed of glacial sediment, was previously identified by Batchelor et al. (2013b, 2013a, 2014). They interpreted glacial ice advancing northwesterly through Amundsen Gulf to the shelf break in the Beaufort Sea at least eight times during the Quaternary, although it is unknown how many of these advances were oscillations of the same ice front. Our observation of glacial sedimentation below Unit H (Unit G) suggests additional proximal glacial sedimentation may have been preserved on the Banks Island shelf beyond what was previously documented. Our interpretation of additional glacial sedimentation below Batchelor’s units (Unit F and above) suggests a need to re-visit the conceptual and numerical models of ice cover in Arctic Canada.

Dixon et al. (1992) defined the Shallow Bay Sequence as the youngest identifiable seismic unit within the Beaufort–Mackenzie Basin – a less than 50 m thick veneer of sediment that extends across the shelf area and thickens in the slope and deep-water environments. They also stated it might include many Pleistocene glacial and interglacial deposits. Within the Banks–Beaufort Basin, the Shallow Bay Sequence cannot be discerned from the IpS below. We, therefore, argue that the Shallow Bay Sequence should either be discarded or limited to the Beaufort–Mackenzie Basin. Within the Banks–Beaufort Basin, the IpS should be used to describe sediments extending from the Late Miocene unconformity, through to the modern, post-glacial sedimentation (latest Pleistocene to Holocene) and include both distal glaciofluvial input (early portion of the

last glaciation) and later, grounded ice extending onto the shelf. Figure 3.13 illustrates a tentative chronostratigraphic framework for the IpS in the Banks–Beaufort Basin, based largely on climatostratigraphic interpretations. The stratigraphy for onshore Banks Island is provided from field reports (Miall 1979, Vincent 1983, Fyles et al. 1994, Vaughan et al. 2014, Braschi 2015) and drilled wells (Figure 3.1A, Figure 3.3). The Banks–Beaufort Basin and Amundsen Gulf stratigraphy is based on the interpretations presented here, while the Beaufort–Mackenzie Basin stratigraphy is based on an initial stratigraphic table presented by Dixon et al. (1992, their Fig. 14) and an alternative interpretation of Amundsen Gulf by Batchelor et al. (2013) is also presented as a contrast.

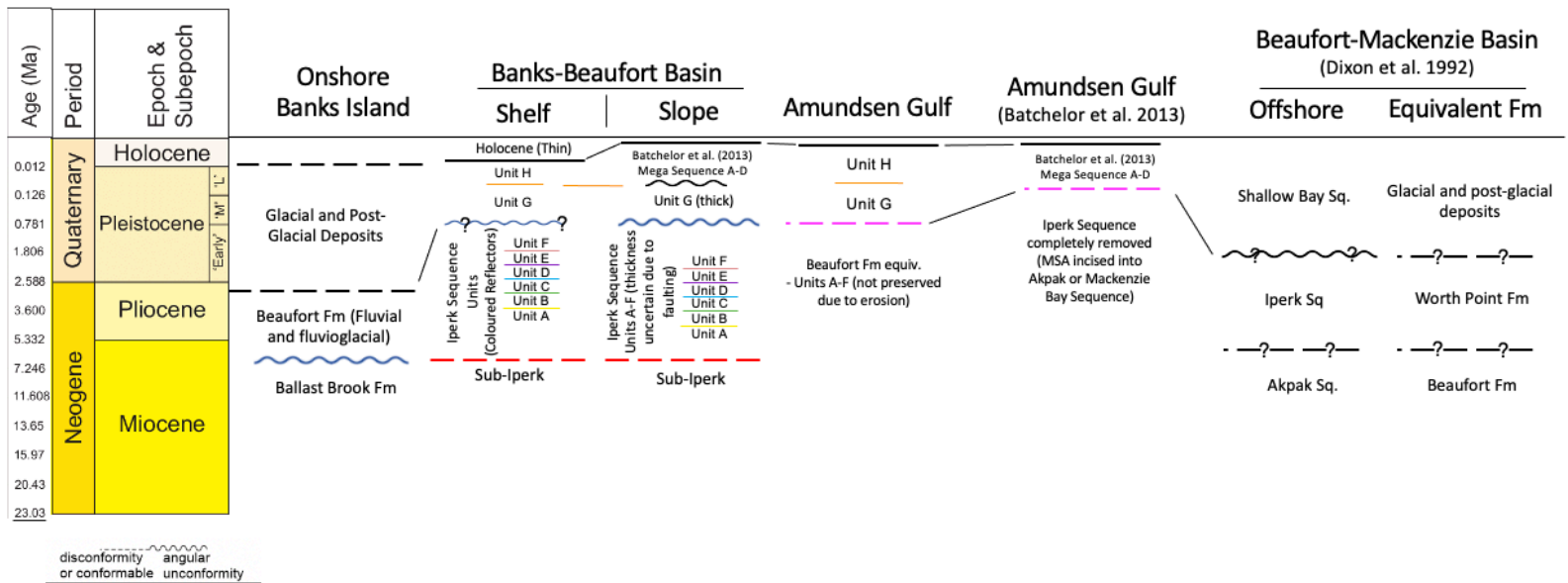


Figure 3.13: Lithostratigraphic and sequence nomenclature of Late Cenozoic strata on Banks Island and within the Banks–Beaufort Basin, and within Amundsen Gulf. This is compared to nomenclature used by Dixon et al (1992) for the Beaufort- Mackenzie Basin. Question marks are used to show uncertainty in age delineations. The colours of the stratigraphy within the Banks–Beaufort Basin correspond with colours used in the interpreted units within this paper (Figure 3.5).

3.6.3 Sedimentation rate estimates

We have interpreted seismic facies (Table 3.1) to characterize the depositional environments and used climatostratigraphy to infer an age of these strata (Figure 3.12). Here we provide a first attempt at quantifying Pliocene and Pleistocene sedimentation rates (MTyr^{-1}) in the Banks–Beaufort Basin (Table 3.3). These rates are a minimum because our interpretation is limited by the area covered by the seismic data and there are probable interglacial hiatuses within the time frame that cannot be quantified. Owing to the imprecision of the chronology and lack of wells to better constrain the velocity–depth relationship, we present rates based on two reasonable climatostratigraphic scenarios. A better chronology is needed in future in order to decrease the uncertainty and level of assumptions in the sediment flux rate calculations.

During the deposition of Unit A in the Late Miocene and Early Pliocene, erosion rates were moderate, at $3.5 \times 10^6 \text{ MTyr}^{-1}$ in Scenario 1¹ or $5.0 \times 10^6 \text{ MTyr}^{-1}$ in Scenario 2. Scenario 1 is based strictly on the traditional lower Pliocene pick (5.33 Ma), while Scenario 2 is based on the isochron burial ages of the BFm on Prince Patrick Island (Chapter 2) which yielded an age of $6.2 \pm 0.2 \text{ Ma}$. Climate was still relatively warm in comparison to the Late Pliocene and Pleistocene, and sediment was likely erosion-limited (but strongly weathered), resulting in slower erosion rates and sediment flux to the basin. The presence of glaciofluvial facies in Units B–F suggests climate was cooling and glaciations started occurring with more frequency. Sediment flux to the basin increased to $21.0 \times 10^6 \text{ MTyr}^{-1}$. Erosion could have tapped into some of the easily accessible, deeply weathered, and weakly lithified sands of the Eocene Eureka Sound Group and other more distal sources like the Paleozoic platform carbonates of the southern CAA, and even far-travelled Canadian Shield granites to provide such a large quantity of sediment. The onset of glacial erosion within the Banks–Beaufort Basin catchment could have provided the energy required to mobilize and deposit these large volumes of sediment to the Banks–Beaufort Basin. This process and comparable increases in sediment flux are well documented in the White Channel Gravel deposits in Yukon, which were rapidly deposited from deeply weathered albite Klondike schist source regions between 3.8 and 2.8 Ma (Gosse et al. *in prep*). Similar increases in sedimentation rates during comparable

time periods have been recorded off the east coast of Canada (Piper and Normark 1989), the Gulf of Alaska (Lagoe et al. 1993), and the Gulf of Mexico (Galloway 2008).

Following the deposition of Unit F sometime in the late Piacenzian to Gelasian (these dates are only speculative, Figure 3.12), sediment flux rates in the Pleistocene increased further from $21.0 \times 10^6 \text{ MTyr}^{-1}$ to $24 \times 10^6 \text{ MTyr}^{-1}$. As glaciations became more pronounced and the progressive incision of inter-island channels amplified, there was a change from regional rivers crossing a contiguous arctic coastal plain to small, channelized flows and perhaps marine-based ice margins that are dominated by glacial cycles of binging and purging sediments accumulated within the channels between glaciations. Large marine-based glacial ice streams can mobilize more sediment as the glacier fronts approach and encroach upon Banks Island, which could be the cause of the observed increase in sediment flux. This sediment flux rate likely is only a minimum estimate as the localized efficient flow of the ice streams through defined channels may have even bypassed the Banks Island shelf and instead have been deposited in large glacial fans deeper in the basin; our isopach estimations may only capture a fraction of this process. Expanding interpretations deeper into the basin and the trough mouths would be necessary to better constrain these sedimentation rates beyond the shelf.

Table 3.3. Sedimentation rates calculated from the Iperk Sequence equivalent in the Banks–Beaufort Basin. Dual scenarios are presented here due to chronological uncertainty.

Unit	Interpreted Age Range of Deposition (Ma)	Total Duration of Deposition (Ma)	Sedimentation Rate (MTyr^{-1})
<i>Scenario 1</i>			
G-H	1.0 – 0	1	24E6
B-F	3.3 – 1.0	2.3	21E6
A	5.3 – 3.3	2	3.5E6
<i>Scenario 2</i>			
G-H	1.0 – 0	1	24E6
B-F	3.3 – 1.0	2.3	21E6
A	6.2 – 3.3	2.9	5.0E6

3.6.4 Pliocene Shorelines

There have historically been significant uncertainties associated with estimates of Pliocene ice sheet volumes and extents. For example, Middle Pliocene Antarctic Ice Sheet volumes range from near present-day values to more than a 33 percent reduction (Raymo et al. 2018). Additionally, models of dynamic regional topography require constraints that can be offered by the positions of relative sea level in Pliocene records (Raymo et al. 2011). By reconstructing depositional environments in the Banks–Beaufort Basin, we can constrain the location of paleoshorelines offshore Banks Island. Units A-F in the Banks–Beaufort Basin are interpreted to be proximal delta front environments (Figure 3.9). The time-equivalent Bfm sediments onshore Banks Island are mostly sandy braided stream deposits (Fyles et al. 1994). The Pliocene paleoshoreline must lie in a zone between these two depositional environments, located approximately 40-50 km offshore from the modern-day shoreline, 30-50 m below modern sea level. Unfortunately, this zone lacks ION seismic coverage, so these features are not directly observable. However, the presence of another observable lowstand feature above Unit H (Figure 3.11) and the lack of other lowstand features within Units A-G support the theory that they may exist more proximal to the modern-day shoreline. These paleoshoreline location estimates provide crucial constraints for ice sheet models and global mean sea level rise in the Pliocene and allow for better model predictions of future sea level rise.

3.6.5 Timing of Inter-Island Channels/Trough Formation

The occurrence of inter-island channels within the CAA was likely a significant influence on the regional climate and paleoceanographic circulation. The opening of the CAA could have drastically reduced the continentality of the Arctic landmass, resulting in a direct effect on vegetation and sea ice albedo. These, in addition to changes in ocean circulation through the CAA, could cause feedbacks that accelerated landscape change. It is possible that incision contributed to the termination of the boreal forest ecosystem by greatly diminishing the summer warmth of the previously contiguous landmass (England 1987). The mechanism of opening of the inter-island channels (including M’Clure Strait and Amundsen Gulf) was previously unknown. Within M’Clure Strait and Amundsen Gulf, the basal reflector of Unit G marks an erosive contact with bedrock (Lakeman et al.

2018) and the absence of Pliocene deposits. Additionally, no faults were observed parallel to the trough walls. This erosion and lack of faulting suggest these inter-island channels bordering Banks Island were predominantly formed by post-Pliocene incision. Large-scale incisions formed by ice streams extending through the troughs (Stokes et al. 2005, Margold et al. 2015) and are likely responsible for the scale of erosion observed. This is consistent with our sedimentation rate calculations (Table 3.3) which suggest an increase in sediment flux to the shelf occurred concurrently with the presence of grounded ice on the shelf. This supports Manion's (2017) approach for flexure during glacial incision and nullifies England's (1987) hypothesis that the straits were evidence of block-faulting and graben formation. The post-Pliocene timing of formation of these troughs is supported by the lack of stream paleoflow deflection toward the straits during the deposition of the Pliocene BFM and by available cosmogenic nuclide burial age chronology of the BFM (6.2 to 2.7 Ma) (McNeil et al. 1990, Kaufman et al. 1993, Braschi 2015) which suggests abandonment around the beginning of the Pleistocene. Observations of the *Clin* facies (Figure 3.9) within Amundsen Gulf prior to the onset of glaciogenic sedimentation (Units F and G) could suggest that Amundsen Gulf and M'Clure Strait were major conduits of fluvial sedimentation in the Pleistocene. It is probable that the ice streams are located where they are because they took advantage of this large pre-existing incised fluvial valley system. The opening of these troughs may have been an important control on Quaternary landscape evolution (Manion, 2017). Therefore, by constraining the timing of incision, we may provide context to better understand the effects it may have had on the evolution of the arctic landscape.

3.7 Conclusions

We provide new interpretations for the IpS, a relatively complete section of Late Miocene through Pleistocene strata constituting a clastic wedge along the western Canadian Arctic Archipelago in the Beaufort Sea and Canada Basin, based on seismic data from ION. We reveal significant differences in the IpS in the Banks–Beaufort Basin compared to the Beaufort–Mackenzie Basin and argue future interpretations of the Canadian Arctic Archipelago margin are probably better guided by a Banks–Beaufort

Basin model, reflecting similarities in tectonic setting, sediment provenance, and glacial influence.

We use six ubiquitous seismic facies to distinguish eight seaward thickening seismostratigraphic units bound by planar, conformable horizons in the IpS on Banks shelf and slope. The lowermost unit overlies a probable Late Miocene aged basin-wide unconformity observed throughout the Beaufort Sea. Two additional uppermost units (Units G and H) are erosion bound and attributed to glacial origin and attest to shelf-crossing Pleistocene glaciations on Banks Island shelf. Unit G is a newly observed glacial unit below previously identified glacial sedimentation, providing evidence for a previously unidentified older shelf crossing glaciation on the Banks Island shelf.

It appears that the Banks–Beaufort Basin contains a greater proportion of laterally continuous parallel beds and a relatively greater component of glacial sediment than its Beaufort–Mackenzie Basin counterpart. The facies transitions are generally gradual and represented in all but the lower and upper units. The transition from Unit A to Units B-F is interpreted to represent the transition from lower energy distal deltaic systems to high-energy shallow water systems, which together are interpreted to represent the climatic cooling and increase in glaciofluvial sedimentation. Inferences from these paleoenvironmental models suggest that Pliocene paleoshorelines existed ~50 km seaward from the modern-day shoreline.

Shelf-edge parallel deep-seated growth faulting is prevalent near the Banks Island shelf break, becoming more frequent, younger, and of higher magnitude seaward. Some cut even the latest glacial deposits. Future analysis should focus on assessing the nature and timing of faulting (the climatostratigraphic units provide a framework of timing of these events). Additionally, a preliminary fault analyses of the inter-island channels shows that the walls of the inter-island channels (such as M'Clure Strait) are not fault bound. This suggests that these waterways were formed by fluvial and then glacial incision into the BFM and underlying units, not grabens resulting from north-south Cenozoic extension. The seismostratigraphy provides an estimate of the maximum stratigraphic age of incision of these channels. However, given that paleoflow directions observed in the BFM outcrops adjacent to the straits do not appear to deflect toward the

straits but flow instead perpendicular toward Canada Basin, it seems most logical that the incision of M'Clure Strait occurred sometime in the Late Pliocene or Pleistocene. Without well control, it is not yet possible to resolve the woody sandy braided stream Bfm equivalent units within the IpS. Therefore, the current model requires that as deposition of the Bfm ceased, aggradation of the IpS continued offshore.

3.8 Acknowledgements

The multichannel BeaufortSPAN East seismic data was made available through an agreement between ION and the Geological Survey of Canada (and its collaborators). E.A. Atkinson, J. Jassim, and H. King of GSC-Calgary are thanked for significant assistance during the initial seismic interpretation. We thank Tom Brent for facilitating institutional access, R. Courtney and J. Evangelatos for assistance formatting the data, and D. O'Connor for initial interpretation insights. The Arctic Net Seabed Mapping program (<https://arcticnet.ulaval.ca/project/arctic-seafloor-mapping-data-processing-and-dissemination>) provided support for a sub-bottom profiling survey of the terrace and two sediment cores, supplemented by publicly available USCGS Healy profiles. This research was supported under Natural Resources Canada's Geo-Mapping for Energy and Minerals Program (LMS contribution # XXXX) and principally by JCG's NSERC-Discovery Grant XXXX.

Chapter 4. Implications and Conclusions

The first objective of this thesis was to utilize the sedimentology, paleoflow measurements and apply the isochron/simple burial dating methods to a 35.7 m thick BFm section near the type locality on Prince Patrick Island to refine the BFm chronology. Results of this objective include a cobble isochron burial ages of 6.20 ± 0.20 Ma. Simple burial dating of sand samples from the same section yielded minimum ages of 3.43 Ma ($^{+0.477}/_{-0.300}$) and 5.63 Ma ($^{+0.467}/_{-0.303}$). This is the first numerical dating approach applied to the BFm on Prince Patrick Island near the type locality and confirms that the BFm is as old as the Messinian. This age is up to 1 Ma older than many previous BFm studies, although it is consistent with published estimates based on biostratigraphic microfossil remains (plant macro- and microfossils, arthropods, pollen). These results indicate that the often-cited Pliocene age of the BFm may not be entirely correct and fails to capture an earlier initiation. Assessments of the stratigraphy and sedimentology of the BFm sections inspected on Prince Patrick Island confirm its braided stream paleoenvironmental interpretation (Fyles 1990, Devaney 1991). While the 6.2 ± 0.02 Ma age establishes a numerical constraint of the BFm and extends the range of time during which the BFm was deposited, the exposed sections from which it was derived are likely only a small remnant of what had originally been deposited. Estimates of 200-400 m of BFm deposits have been eroded from onshore Prince Patrick Island (Manion, 2017). This isochron age defines a minimum age of deposition of the BFm as there is no evidence to suggest section D8 from which this age was measured was at the base or top of the BFm section.

A second objective of this study was to measure and assess paleoflow directions within sections of the BFm on Prince Patrick Island. The dominant flow directions were towards the WSW. If a significant depression where M'Clure Strait is today existed at the time these sediments were being deposited, even if above contemporaneous sea level, the paleoflow in the BFm in the southern part of Prince Patrick Island likely would have been deflected northward, as per today's drainage pattern. Instead, it appears paleoflow during the deposition of the BFm was oriented toward the Canada Basin. This paleoflow concurs with approximately contemporaneous paleoflow towards the Canada Basin, as indicated

by large channels within the BFM located within 15 kilometres of M'Clure Strait on northwestern Banks Island (Braschi 2015). The interpretation that the majority of the incision of M'Clure Strait must post-date the BFM on both Banks and Prince Patrick Island is supported by a fault analysis within the inter-island channels, which affirms that there is no evidence of faulting indicative of a graben structure along the walls of the straits parallel to the coastline. This observation contributes towards the falsification of the hypothesis that M'Clure Strait was formed as a Cenozoic graben (England 1987). The paleoflow measurements combined with the isochron age of the BFM on Prince Patrick Island (6.20 ± 0.20 Ma) suggest the incision of M'Clure Strait and the other inter-island channels comprising the Parry Channel Northwest Passage occurred after this period of deposition. The progressive dissection of the landscape may have been an important erosional event in the High Arctic, depositing a significant sediment volume to the shelf and slope. Additionally, the subsequent opening of these channels may have been an important ocean circulation change that could have influenced the Arctic climate.

The third objective of this thesis was to interpret the recently released 2D marine seismic reflection data from ION to define units within the IpS, considered to be the offshore marine extension of the BFM, and investigate how the offshore stratigraphy and geo-features might support paleoflow analyses, channel evolution, and onshore-offshore correlation with respect to better understanding the BFM.

In the Banks–Beaufort Basin, the Ips was subdivided into eight units ranging in age from the Late Miocene to Pleistocene. By rationalizing this seismic stratigraphy to climate events and lowstands during this period, a climatostratigraphy could be established. With this climatostratigraphy, an estimate of the volume of sediment deposited into the Banks–Beaufort Basin can be measured through time. The per-unit volume changes are evaluated and compared with significant climate events occurring in the Late Miocene–Pleistocene. Several depositional environments, including a transition from high-energy shallow marine systems to lower energy distal delta front systems, have been identified using seismic facies attributes. Using this depositional environment model of the stratigraphy, our results indicate that Pliocene shorelines are likely to lie between 40 to 50 km offshore, but are either outside the extents of seismic coverage, or can only be resolved with higher resolution seismic imaging. A preliminary investigation for the

presence of faulting was conducted on the Banks shelf, slope, within M'Clure Strait north of Banks Island, and south of Prince Patrick Island, and the mouth of Amundsen Gulf.

4.2 Implications and Future Work

The new onshore and offshore stratigraphy and basin evolution in the Banks–Beaufort Basin has a number of implications for the study of Late Miocene to Pleistocene basin evolution in the CAA. First, cosmogenic isotope measurements will allow us to evaluate the synchronicity, duration, erosion rates, and timing of the deposition of the BFM, a crucial step towards understanding the preconditions and triggers involved in the deposition of the BFM, a significantly large sediment package. Hypotheses regarding the nature of the disparities in paleoclimate among potentially contemporaneous sites and the total volume of sediment eroded since the Pliocene can be evaluated.

The IpS within the Banks–Beaufort Basin has been divided and interpreted for the first time, increasing our understanding of the offshore record that encompasses stratigraphy from the Late Miocene through the Pleistocene, much of which is interpreted to be the marine extension of the BFM. Reconstructions of climatostratigraphic units, volumes of sediment, and associated depositional environments through time broaden our knowledge of how the Arctic basin evolved during this time period and anchors future studies on how these sedimentary records relate to the rapidly growing number of paleoclimatic and paleoenvironmental reconstructions.

By isolating glacial facies and units from the underlying fluvial units, the history of glaciation offshore Banks Island can be evaluated, extending previous work by Batchelor et al. (2013a, 2013b, 2014). This also provides a constraint of the timing of incision of the inter-island channels in the western CAA. This work contributes to understanding the evolution of the inter-island channels in the western parts of the CAA, by constraining the age of the cross-shelf troughs on the Beaufort Sea shelf (i.e., Amundsen Gulf and M'Clure Strait), which eroded into IpS strata. These conclusions may contribute to refining the history of Pliocene -Pleistocene marine connectivity between the North Atlantic and Arctic Oceans.

Shorelines or other lowstand features cannot be resolved within the ION data. However, the higher resolution GEBCO data suggest shoreline features of unknown age (but possibly Pliocene) exist in the IpS approximately 50 km west of the modern Banks Island shoreline. These observations contribute towards a database of worldwide Pliocene shorelines and much needed constraints on Pliocene sea level and ice volume. Expanding Pliocene shoreline data coverage is essential to constraining ice sheet models, paleodynamic topography models, and global mean sea level reconstructions in the Pliocene (Raymo et al. 2011, Pollard et al. 2018) and allow for more accurate model predictions of the implications of future sea level rise.

The final and overall objective of this thesis was to improve our understanding of the distribution and evolution of the BFm and Iperk Sequence. Figure 4.1 depicts a conceptualized block diagram of the BFm, equivalent sites, and the submarine Iperk Sequence. It illustrates a snapshot of the High Arctic landscape and some of the depositional environments present during the deposition of the BFm. This thesis specifically contributes to our knowledge of the braid plain component of the BFm (as observed on Prince Patrick Island) and the offshore IpS stratigraphy which encompasses a near complete section of Late Miocene to Pleistocene stratigraphy. Conclusions from this thesis have improved our understanding of the basin evolution and the onshore and offshore components of the BFm and Iperk Sequence.

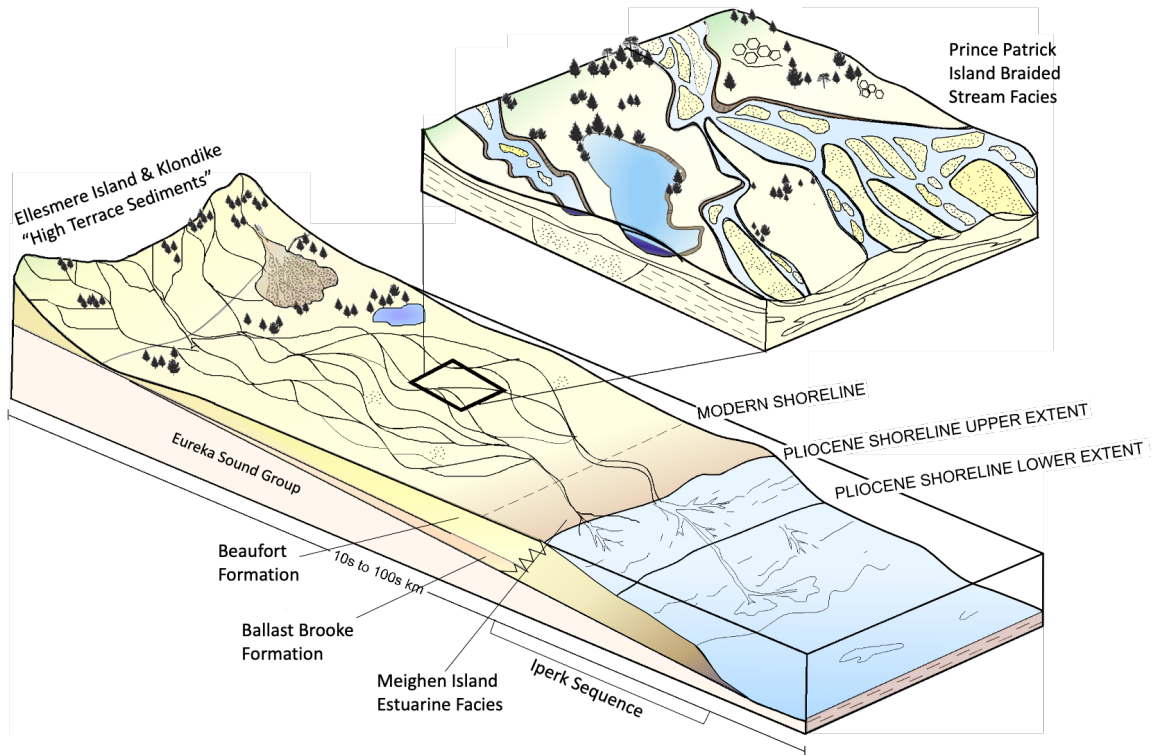


Figure 4.1. Block diagram illustrating an interpretation of the depositional environment of the BFm during the Late Miocene and Pliocene. This diagram encompasses observations from multiple island sites in order to characterize a snapshot of what the system looked like during the deposition of the BFm. Chapter 2 of this thesis has informed the Prince Patrick Island portion of this diagram. The miniature stratigraphic column represents the sections observed on Prince Patrick Island. Chapter 3 of this thesis informed the offshore Iperk Sequence portion of the diagram.

Future work should involve using the newly measured ^{10}Be concentrations to calculate paleo-erosion rates, which can then be used to evaluate sediment flux rates and sediment availability of the BFm. These will help verify and correlate sediment volumes within the IpS offshore and analyze the isostatic consequences of deposition of the BFm clastic wedge. Additional testing of the chronology is recommended and would include re-running the ^{26}Al samples and testing in situ ^{14}C to investigate if the y-intercept of the isochron age reported is the result of post-burial production or simply an artifact of the best fit through the data. Discrepancies with the simple burial age should also be investigated further. Despite this, the cobble isochron method has been proven as a tool that can be used in the High Arctic to calculate an age of the BFm, it is still too imprecise

to determine if a section has been deposited within an inter-glacial or glacial period. The isochron method can be used to indicate that post-burial production occurred within one's samples (the isochron would go through the y-intercept instead of the origin), which is valuable in comparison to the 'simple' burial ages. However, the isochron age did not significantly reduce the uncertainty in comparison to the simple burial age method. Future work to constrain the age of the BFM should focus on reducing uncertainty in the TCN methodologies.

In the future, if wells are drilled within the Banks–Beaufort Basin, analyses such as numerical dating efforts and sedimentological descriptions should be conducted and used to ground truth the initial IpS seismostratigraphy and climatostratigraphy.

Further studies should focus on identifying, inspecting, and deriving further chronological constraints of additional BFM sites, to improve data-model comparisons for warm period climate modelling and establish the extent of the BFM across the entire CAA. Enriching the faunal, floral, and paleoenvironmental proxy interpretations with a continuously improving chronostratigraphy will continue to allow investigations into archipelago-scale changes and basin evolution during the Late Miocene and Pliocene–Pleistocene transition.

References

- Balco, G., Briner, J., Finkel, R.C., Rayburn, J.A., Ridge, J.C., and Schaefer, J.M. 2009. Regional beryllium-10 production rate calibration for late-glacial northeastern North America. *Quaternary Geochronology*, **4**: 93–107. Elsevier Ltd. doi:10.1016/j.quageo.2008.09.001.
- Balco, G., and Rovey, C.W. 2008. An isochron method for cosmogenic-nuclide dating of buried soils and sediments. *American Journal of Science*, **308**: 1083–1114. doi:10.2475/10.2008.02.
- Ballantyne, A.P., Greenwood, D.R., Sinninghe Damsté, J.S., Csank, A.Z., Eberle, J.J., and Rybczynski, N. 2010. Significantly warmer Arctic surface temperatures during the Pliocene indicated by multiple independent proxies. *Geology*, **38**: 603–606. doi:10.1130/G30815.1.
- Barendregt, R., Matthews Jr., J. V., Fyles, J.G., Maricovich, L., Behan-Pelletier, V., Brigham-Grette, J., Ovensen, L.E., and Brouwers, E. (n.d.). *Biostratigraphy, Age and the Paleoenvironment of the Pliocene Beaufort Formation on Meighen Island, Canadian Arctic Archipelago*.
- Barendregt, R.W., and Vincent, J.-S. 1990. Late Cenozoic paleomagnetic record of Duck Hawk Bluffs, Banks Island, Canadian Arctic Archipelago. *Canadian Journal of Earth Sciences*, **27**: 124–130. doi:10.1139/e90-010.
- Barendregt, R.W., Vincent, J.S., Irving, E., and Baker, J. 1998. Magnetostratigraphy of Quaternary and late Tertiary sediments on Banks Island, Canadian Arctic Archipelago. *Canadian Journal of Earth Sciences*, **35**: 147–161. doi:10.1139/e97-094.
- Bartoli, G., Sarnthein, M., Weinelt, M., Erlenkeuser, H., Garbe-Schönberg, D., and Lea, D.W. 2005. Final closure of Panama and the onset of northern hemisphere glaciation. *Earth and Planetary Science Letters*, **237**: 33–44. doi:10.1016/j.epsl.2005.06.020.
- Batchelor, C.L., and Dowdeswell, J.A. 2014. The physiography of High Arctic cross-shelf troughs. *Quaternary Science Reviews*, **92**: 68–96. Elsevier Ltd. doi:10.1016/j.quascirev.2013.05.025.
- Batchelor, C.L., Dowdeswell, J.A., and Pietras, J.T. 2013a. Seismic stratigraphy, sedimentary architecture and palaeo-glaciology of the Mackenzie Trough: Evidence for two Quaternary ice advances and limited fan development on the western Canadian Beaufort Sea margin. *Quaternary Science Reviews*, **65**: 73–87. Elsevier Ltd. doi:10.1016/j.quascirev.2013.01.021.

- Batchelor, C.L., Dowdeswell, J.A., and Pietras, J.T. 2013b. Variable history of Quaternary ice-sheet advance across the Beaufort Sea Margin, Arctic Ocean. *Geology*, **41**: 131–134. doi:10.1130/G33669.1.
- Batchelor, C.L., Dowdeswell, J.A., and Pietras, J.T. 2014. Evidence for multiple quaternary ice advances and fan development from the amundsen gulf cross-shelf trough and slope, canadian beaufort sea margin. *Marine and Petroleum Geology*, **52**: 125–143. Elsevier Ltd. doi:10.1016/j.marpetgeo.2013.11.005.
- Batchelor, C.L., Margold, M., Krapp, M., Murton, D.K., Dalton, A.S., Gibbard, P.L., Stokes, C.R., Murton, J.B., and Manica, A. 2019. The configuration of Northern Hemisphere ice sheets through the Quaternary. *Nature Communications*, **10**: 1–10. Springer US. doi:10.1038/s41467-019-11601-2.
- Beaubouef, R.T., and Friedmann, S.J. 2000. High resolution seismic/sequence stratigraphic framework for the evolution of Pleistocene intra slope basins, western Gulf of Mexico: depositional models and reservoir analogs. *In Deep-water reservoirs of the world: Gulf Coast Section SEPM 20th Annual Research Conference*. pp. 40–60.
- Berger, A. 1988. Milankovitch Theory and Climate. *Reviews of Geophysics*, **26**: 624–657. doi:10.1029/RG026i004p00624.
- Bhattacharya, J.P., and Walker, R.G. 1992. Deltas. *In In: Facies Models: response to sea level changes. Edited by R.G. Walker and N.P. James. Citeseer*. pp. 157–177.
- Blakey, R. 2021. Paleotectonic and Paleogeographic History of the Arctic Region. *Atlantic Geology*, **57**: 7–39. doi:10.4138/atlgeol.202.
- Blasco, S.M., Fortin, G., Hill, P.R., O'Connor, M.J., and Brigham-Grette, J. 1990. The Arctic Ocean Region. *In The Arctic Ocean Region. Edited By A. Grantz, L. Johnson, and J.F. Sweeney. Geological Society of America, United States*. doi:10.1130/DNAG-GNA-L.
- Blum, M.D., and Aslan, A. 2006. Signatures of climate vs. sea level change within incised valley-fill successions: Quaternary examples from the Texas Gulf Coast. *Sedimentary Geology*, **190**: 177–211. doi:10.1016/j.sedgeo.2006.05.024.
- Braschi, L.C. 2015. Chronostratigraphy of the Beaufort Formation , western Canadian Arctic Archipelago. Dalhousie University.
- Brigham-Grette, J., and Carter, L.D. 1992. Pliocene marine transgressions of northern Alaska: circumarctic correlations and paleoclimatic interpretations. *Arctic*, **45**: 74–89. doi:10.14430/arctic1375.
- Bustin, R.M. 1982. Beaufort Formation, eastern Axel Heiberg Island, Canadian Arctic Archipelago. *Bulletin of Canadian Petroleum Geology*, **30**: 140–149. doi:https://doi.org/10.35767/gscpgbull.30.2.140.

- Bustin, R.M. 1986. Organic Maturity of Late Cretaceous and Tertiary Coal Measures, Canadian Arctic Archipelago. *International Journal of Coal Geology*, **6**: 71–106.
- Corbett, L.B., Bierman, P.R., Rood, D.H., Caffee, M.W., Lifton, N.A., and Woodruff, T.E. 2017. Cosmogenic $^{26}\text{Al}/^{10}\text{Be}$ surface production ratio in Greenland. *Geophysical Research Letters*, **44**: 1350–1359. doi:10.1002/2016GL071276.
- Courtney, R. 2007. Storage and Dissemination of SEG Y Data in JPEG2000 Format. *AGU Fall Meeting Abstracts*, **1**: 402.
- Csank, A.Z., Fortier, D., and Leavitt, S.W. 2013. Annually resolved temperature reconstructions from a late Pliocene-early Pleistocene polar forest on Bylot Island, Canada. *Palaeogeography, Palaeoclimatology, Palaeoecology*, **369**: 313–322. Elsevier B.V. doi:10.1016/j.palaeo.2012.10.040.
- Csank, A.Z., Tripathi, A.K., Patterson, W.P., Eagle, R.A., Rybczynski, N., Ballantyne, A.P., and Eiler, J.M. 2011. Estimates of Arctic land surface temperatures during the early Pliocene from two novel proxies. *Earth and Planetary Science Letters*, **304**: 291–299. Elsevier B.V. doi:10.1016/j.epsl.2011.02.030.
- Davies, N.S., Gosse, J.C., and Rybczynski, N. 2014. Cross-bedded woody debris from a pliocene forested river system in the high arctic: Beaufort formation, Meighen Island, Canada. *Journal of Sedimentary Research*, **84**: 19–25. doi:10.2110/jsr.2014.5.
- Devaney, J.R. 1991. Clastic sedimentology of the Beaufort Formation, Prince Patrick Island, Canadian Arctic Islands: late Tertiary sandy braided river deposits with woody detritus beds. *Arctic*, **44**: 206–216. doi:10.14430/arctic1540.
- Dietrich, J.R., Dixon, J., and McNeil, D.H. 1985. Sequence analysis and nomenclature of upper cretaceous to holocene strata in the Beaufort-Mackenzie Basin. *In Geological Survey of Canada Current Research*. doi:10.4095/120169.
- Dixon, J. 1996. Geological Atlas of the Beaufort-Mackenzie Area. *In Geologic Survey of Canada, Miscellaneous Report*. doi:10.4095/207658.
- Dixon, J., Dietrich, J.R., Lane, L.S., and McNeil, D.H. 2008. Chapter 16 Geology of the Late Cretaceous to Cenozoic Beaufort-Mackenzie Basin, Canada. *In Sedimentary Basins of the World*. Elsevier. pp. 551–572. doi:10.1016/S1874-5997(08)00016-6.
- Dixon, J., Dietrich, J.R., and McNeil, D.H. 1992. Upper Cretaceous to Pleistocene Sequence Stratigraphy of the Beaufort-Mackenzie and Banks Island Areas, Northwest Canada. *In Geologic Survey of Canada Bulletin*. doi:10.1038/075149c0.
- Dixon, J., Lane, L.S., Dietrich, J.R., McNeil, D.H., and Chen, Z. 2019. Geological History of the Late Cretaceous to Cenozoic beaufort-mackenzie basin, arctic canada. *The Sedimentary Basins of the United States and Canada*,: 695–717. doi:10.1016/B978-0-444-63895-3.00017-6.

- Dowdeswell, J.A., Ottesen, D., Rise, L., and Craig, J. 2007. Identification and preservation of landforms diagnostic of past ice-sheet activity on continental shelves from three-dimensional seismic evidence. *Geology*, **35**: 359–362. doi:10.1130/G23200A.1.
- Dowsett, H., Robinson, M., Haywood, A., Salzmann, U., Hill, D., Sohl, L., Chandler, M., Williams, M., Foley, K., and Stoll, D. 2010. The PRISM3D paleoenvironmental reconstruction. *Stratigraphy*, **7**: 123–139.
- Ehlers, J., and Gibbard, P.L. 2007. The extent and chronology of Cenozoic Global Glaciation. *Quaternary International*, **164–165**: 6–20. doi:10.1016/j.quaint.2006.10.008.
- Elias, S.A., and Matthews, J. V. 2002. Arctic North American seasonal temperatures from the latest Miocene to the early Pleistocene, based on mutual climatic range analysis of fossil beetle assemblages. *Canadian Journal of Earth Sciences*, **39**: 911–920. doi:10.1139/e01-096.
- England, J.H. 1987. Glaciation and the evolution of the Canadian high arctic landscape. *Geology*, **15**: 419–424.
- England, J.H., Furze, M.F.A., and Doupé, J.P. 2009. Revision of the NW Laurentide Ice Sheet: implications for paleoclimate, the northeast extremity of Beringia, and Arctic Ocean sedimentation. *Quaternary Science Reviews*, **28**: 1573–1596. Elsevier Ltd. doi:10.1016/j.quascirev.2009.04.006.
- Evans, D.J.A., England, J.H., La Farge, C., Coulthard, R.D., Lakeman, T.R., and Vaughan, J.M. 2014. Quaternary geology of the Duck Hawk Bluffs, southwest Banks Island, Arctic Canada: A re-investigation of a critical terrestrial type locality for glacial and interglacial events bordering the Arctic Ocean. *Quaternary Science Reviews*, **91**: 82–123. Elsevier Ltd. doi:10.1016/j.quascirev.2014.03.011.
- Feng, R., Otto-Bliesner, B.L., Fletcher, T.L., Tabor, C.R., Ballantyne, A.P., and Brady, E.C. 2017. Amplified Late Pliocene terrestrial warmth in northern high latitudes from greater radiative forcing and closed Arctic Ocean gateways. *Earth and Planetary Science Letters*, **466**: 129–138. Elsevier B.V. doi:10.1016/j.epsl.2017.03.006.
- Fletcher, T., Feng, R., Telka, A.M., Matthews, J. V., and Ballantyne, A. 2017. Floral Dissimilarity and the Influence of Climate in the Pliocene High Arctic: Biotic and Abiotic Influences on Five Sites on the Canadian Arctic Archipelago. *Frontiers in Ecology and Evolution*, **5**: 1–13. doi:10.3389/fevo.2017.00019.
- Fletcher, T., Warden, L., Sinninghe Damsté, J.S., Brown, K.J., Rybczynski, N., Gosse, J., and Ballantyne, A.P. 2018. The role of elevated atmospheric CO₂ and increased fire in Arctic amplification of temperature during the Early to mid-Pliocene. *Climate of the Past Discussions*,: 1–41. doi:https://doi.org/10.5194/cp-2018-60.

- Fletcher, T.L., Warden, L., Damsté, J.S.S., Brown, K.J., Rybczynski, N., Gosse, J.C., and Ballantyne, A.P. 2019. Evidence for fire in the Pliocene Arctic in response to amplified temperature. *Climate of the Past*, **15**: 1063–1081. doi:10.5194/cp-15-1063-2019.
- Fortier, Y., and Morley, L. 1956. Geological unity of the Arctic Islands. *Royal Society of Canada Transactions*, **50**: 3–12.
- Frazier, D.E. 1974. Depositional episodes: their relationship to the Quaternary stratigraphic framework in the northwestern portion of the Gulf Basin. University of Texas at Austin, Bureau of Economic Geology, Geological Circular, **74**: 28.
- Fyles, J.G. 1989. High Terrace Sediments, Probably of Neogene Age, West-Central Ellesmere Island, Northwest Territories. *In Current Research, Part D, Interior Plains and Arctic Canada*, Geological Survey of Canada. doi:10.4095/126702.
- Fyles, J.G. 1990. Beaufort Formation (late Tertiary) as seen from Prince Patrick Island, Arctic Canada. *Arctic*, **43**: 393–403. doi:10.14430/arctic1632.
- Fyles, J.G., Hills, L.V., Matthews, J.V., Barendregt, R., Baker, J., Irving, E., and Jetté, H. 1994. Ballast Brook and Beaufort Formations (late Tertiary) on Northern Banks Island, Arctic Canada. *Quaternary International*, **22–23**: 141–171. doi:10.1016/1040-6182(94)90010-8.
- Fyles, J.G., Marincovich, L., and Matthews, J. V. 1991. Unique Mollusc Find in the Beaufort Formation [Pliocene] On Meighen Island, Arctic Canada. *In Current Research, Part B, Interior Plains and Arctic Canada*, Geological Survey of Canada. doi:10.4095/132552.
- Galloway, W.E. 2008. Chapter 15 Depositional Evolution of the Gulf of Mexico Sedimentary Basin. *In Sedimentary Basins of the World*. Elsevier. doi:10.1016/S1874-5997(08)00015-4.
- Gladenkov, A.Y., and Gladenkov, Y.B. 2004. Onset of connections between the Pacific and Arctic Oceans through the Bering Strait in the Neogene. *Stratigraphy and Geological Correlation*, **12**: 175–187.
- Gladenkov, A.Y., Oleinik, A.E., Marincovich, L., and Barinov, K.B. 2002. A refined age for the earliest opening of Bering Strait. *Palaeogeography, Palaeoclimatology, Palaeoecology*, **183**: 321–328. doi:10.1016/S0031-0182(02)00249-3.
- Gosse, J.C., Ballantyne, A.P., Barker, J.D., Csank, A.Z., Fletcher, T.L., Grant, G.W., Greenwood, D.R., MacPhee, R.D.E., and Rybczynski, N. 2017. PoLAR-FIT: Pliocene Landscapes and Arctic Remains—Frozen in Time. *Geoscience Canada*, **44**: 47. doi:10.12789/geocanj.2017.44.116.

- Gosse, J.C., and Phillips, F.M. 2001. Terrestrial in situ cosmogenic nuclides: theory and application. *Quaternary Science Reviews*, **20**: 1475–1560. doi:10.1016/S0277-3791(00)00171-2.
- Granger, D.E., Lifton, N.A., and Willenbring, J.K. 2013. A cosmic trip: 25 years of cosmogenic nuclides in geology. *Bulletin of the Geological Society of America*, **125**: 1379–1402. doi:10.1130/B30774.1.
- Granger, D.E., and Muzikar, P.F. 2001. Dating sediment burial with in situ-produced cosmogenic nuclides: theory, techniques, and limitations. *Earth and Planetary Science Letters*, **188**: 269–281. doi:10.1016/S0012-821X(01)00309-0.
- Grantz, A., Eittreim, S., and Dinter, D.A. 1979. Geology and tectonic development of the continental margin north of Alaska. *Tectonophysics*, **15**: 263–291. doi:10.1016/0040-1951(79)90050-7.
- Harrison, J.C., and Brent, T.A. 2005. Basins and fold belts of Prince Patrick Island and adjacent area, Canadian Arctic Islands. *In Geological Survey of Canada Bulletin*. doi:10.4095/220345.
- Harrison, J.C., Embry, A.F., and Poulton, T.P. 1988. Field observations on the structural and depositional history of Prince Patrick Island and adjacent areas, Canadian Arctic Islands. *In Current Research, Part D, Interior Plains and Arctic Canada, Geological Survey of Canada*. doi:10.4095/122657.
- Haywood, A.M., Dowsett, H.J., Valdes, P.J., Lunt, D.J., Francis, J.E., and Sellwood, B.W. 2009. Introduction. Pliocene climate, processes and problems. *Philosophical Transactions of the Royal Society A: Mathematical, Physical and Engineering Sciences*, **367**: 3–17. doi:10.1098/rsta.2008.0205.
- Hea, J.P., Arcuri, J., Campbell, G.R., Fraser, I., Fuglem, M.O., O’Bertos, J.J., Smith, D.R., and Zayat, M. 1980. Post-Ellesmerian Basins of Arctic Canada: Their Depocentres, Rates of Sedimentation and Petroleum Potential. *Facts and Principles of World Petroleum Occurrence, Memoir 6*: 447–488.
- Heer, O. 1868. *Flora Fossilis Arctica: Die in Nordgronland, Auf Der Melville-Insel, Im Banksland, Am MacKenzie, in Island Und in Spitzbergen Entdeckten Fossilen Pflanzen. Flora Fossilis Arctica*, **1**.
- Helwig, J., Kumar, N., Emmet, P., and Dinkelman, M.G. 2011. Chapter 35: Regional seismic interpretation of crustal framework, Canadian Arctic passive margin, Beaufort Sea, with comments on petroleum potential. *Geological Society Memoir*, **35**: 527–543. doi:10.1144/M35.35.
- Hidy, A.J., Gosse, J.C., Froese, D.G., Bond, J.D., and Rood, D.H. 2013. A latest Pliocene age for the earliest and most extensive Cordilleran Ice Sheet in northwestern Canada. *Quaternary Science Reviews*, **61**: 77–84. Elsevier Ltd. doi:10.1016/j.quascirev.2012.11.009.

- Hidy, A.J., Gosse, J.C., Pederson, J.L., Mattern, J.P., and Finkel, R.C. 2010. A geologically constrained Monte Carlo approach to modeling exposure ages from profiles of cosmogenic nuclides: An example from Lees Ferry, Arizona. *Geochemistry, Geophysics, Geosystems*, **11**. doi:10.1029/2010GC003084.
- Hidy, A.J., Gosse, J.C., Sanborn, P., and Froese, D.G. 2018. Age-erosion constraints on an Early Pleistocene paleosol in Yukon, Canada, with profiles of ^{10}Be and ^{26}Al : Evidence for a significant loess cover effect on cosmogenic nuclide production rates. *Catena*, **165**: 260–271. Elsevier. doi:10.1016/j.catena.2018.02.009.
- Hills, L. V., Klovan, J.E., and Sweet, A.R. 1974. *Juglans eocinerea* n. sp., Beaufort Formation (Tertiary), southwestern Banks Island, Arctic Canada. *Canadian Journal of Botany*, **52**: 65–90. doi:10.1139/b74-011.
- Hills, L. V., and Ogilvie, R.T. 1970. *Picea banksii* n. sp. Beaufort Formation (Tertiary), northwestern Banks Island, Arctic Canada. *Canadian Journal of Botany*, **48**: 457–464. doi:10.1139/b70-065.
- Hodgson, D.A. 1990. Were Erratics Moved By Glaciers or Icebergs To Prince Patrick Island, western Arctic Archipelago, Northwest Territories? *In* Current Research, Part D. Interior Plains and Arctic Canada, Geological Survey of Canada. doi:10.4095/131340.
- Hodgson, D.A., Taylor, R.B., and Fyles, J.G. 1994. Late Quaternary Sea Level Changes on Brock and Prince Patrick Islands, Western Canadian Arctic Archipelago. *Géographie physique et Quaternaire*, **48**: 59–84.
- Hodgson, D.A., Vincent, J.S., and Fyles, J.G. 1984. Quaternary geology of central Melville Island, Northwest Territories. *In* Geological Survey of Canada. doi:10.4095/119784.
- Issler, D.R., Grist, A.M., and Stasiuk, L.D. 2005. Post-Early Devonian thermal constraints on hydrocarbon source rock maturation in the Keele Tectonic Zone, Tulita area, NWT, Canada, from multi-kinetic apatite fission track thermochronology, vitrinite reflectance and shale compaction. *Bulletin of Canadian Petroleum Geology*, **53**: 405–431. doi:10.2113/53.4.405.
- Jakobsson, M., Andreassen, K., Bjarnadóttir, L.R., Dove, D., Dowdeswell, J.A., England, J.H., Funder, S., Hogan, K., Ingólfsson, Ó., Jennings, A., Krog Larsen, N., Kirchner, N., Landvik, J.Y., Mayer, L., Mikkelsen, N., Möller, P., Niessen, F., Nilsson, J., O'Regan, M., Polyak, L., Nørgaard-Pedersen, N., and Stein, R. 2014. Arctic Ocean glacial history. *Quaternary Science Reviews*, **92**: 40–67. Elsevier Ltd. doi:10.1016/j.quascirev.2013.07.033.
- Jones, P., Brache, J., and Lentin, K. 1980. The geology of the 1977 offshore hydrocarbon discoveries in the Beaufort-Mackenzie Basin, NWT. *Bulletin of Canadian Petroleum Geology*, **28**: 81–102.

- Kaufman, D.S., Carter, L.D., Miller, G.H., Farmer, G.L., and Budd, D.A. 1993. Strontium isotopic composition of Pliocene and Pleistocene molluscs from emerged marine deposits, North American Arctic. *Canadian Journal of Earth Sciences*, **30**: 519–534. doi:10.1139/e93-041.
- King, E., Lakeman, T.R., and Blasco, S. 2014. The shallow geologic framework of the Banks Island Shelf, eastern Beaufort Sea: Evidence for glaciation of the entire shelf and multiple shelf edge geohazards. *In Arctic Change 2014*. ArcticNet. p. 98.
- Kohl, C., and Nishiizumi, K. 1992. Chemical isolation of quartz for measurement of in-situ -produced cosmogenic nuclides. *Geochimica et Cosmochimica Acta*, **56**: 3583–3587. doi:10.1016/0016-7037(92)90401-4.
- Korschinek, G., Bergmaier, A., Faestermann, T., Gerstmann, U.C., Knie, K., Rugel, G., Wallner, A., Dillmann, I., Dollinger, G., von Gostomski, C.L., Kossert, K., Maiti, M., Poutivtsev, M., and Remmert, A. 2010. A new value for the half-life of ¹⁰Be by Heavy-Ion Elastic Recoil Detection and liquid scintillation counting. *Nuclear Instruments and Methods in Physics Research, Section B: Beam Interactions with Materials and Atoms*, **268**: 187–191. Elsevier B.V. doi:10.1016/j.nimb.2009.09.020.
- Kumar, N., Helwig, J., and Dinkelman, M.G. 2009. Preliminary Evaluation of a Potential Major Petroleum Province from BeaufortSPAN™ Seismic Data: Canadian Arctic Passive Margin, Banks Island Segment. *Banks Island Segment–CSEG Recorder*,: 27–33.
- de la Vega, E., Chalk, T.B., Wilson, P.A., Bysani, R.P., and Foster, G.L. 2020. Atmospheric CO₂ during the Mid-Piacenzian Warm Period and the M2 glaciation. *Scientific Reports*, **10**: 14–21. doi:10.1038/s41598-020-67154-8.
- Lago, M.B., Eyles, C.H., Eyles, N., and Hale, C. 1993. Timing of late Cenozoic tidewater glaciation in the far North Pacific. *Geological Society of America Bulletin*, **105**: 1542–1560. doi:10.1130/0016-7606(1993)105<1542:TOLCTG>2.3.CO;2.
- Lakeman, T.R., and England, J.H. 2012. Paleoglaciological insights from the age and morphology of the Jesse moraine belt, western Canadian Arctic. *Quaternary Science Reviews*, **47**: 82–100. Elsevier Ltd. doi:10.1016/j.quascirev.2012.04.018.
- Lakeman, T.R., and England, J.H. 2014. Late Wisconsinan glaciation and postglacial relative sea level change on western Banks Island, Canadian Arctic Archipelago. *Quaternary Research*, **80**: 99–112. University of Washington. doi:10.1016/j.yqres.2013.02.001.
- Lakeman, T.R., Pienkowski, A.J., Nixon, F.C., Furze, M.F.A., Blasco, S., Andrews, J.T., and King, E.L. 2018. Collapse of a marine-based ice stream during the early Younger Dryas chronozone, western Canadian Arctic. *Geology*, **46**: 211–214. doi:10.1130/G39665.1.

- Lal, D. 1991. Cosmic ray labeling of erosion surfaces: in situ nuclide production rates and erosion models. *Earth and Planetary Science Letters*, **104**: 424–439. doi:10.1016/0012-821X(91)90220-C.
- Lane, L.S. 2002. Tectonic Evolution of the Canadian Beaufort Sea - Mackenzie Delta region: a brief review. *Canadian Society of Exploration Geophysicists Recorder*, **27**: 49–56.
- Lane, L.S., and Dietrich, J.R. 1995. Tertiary Structural Evolution of the Beaufort Sea - Mackenzie Delta Region, Arctic Canada. *Bulletin of Canadian Petroleum Geology*, **43**: 293–314.
- Lifton, N., Sato, T., and Dunai, T.J. 2014. Scaling in situ cosmogenic nuclide production rates using analytical approximations to atmospheric cosmic-ray fluxes. *Earth and Planetary Science Letters*, **386**: 149–160. Elsevier B.V. doi:10.1016/j.epsl.2013.10.052.
- Lisiecki, L.E., and Raymo, M.E. 2005. A Pliocene-Pleistocene stack of 57 globally distributed benthic δ 18O records. *Paleoceanography*, **20**: 1–17. doi:10.1029/2004PA001071.
- Manion, P. 2017. Lithospheric flexural controls on landscape evolution during deposition and incision of the Beaufort Formation, western Canadian Arctic. Dalhousie University.
- Margold, M., Stokes, C.R., and Clark, C.D. 2015. Ice streams in the Laurentide Ice Sheet: Identification, characteristics and comparison to modern ice sheets. *Earth-Science Reviews*, **143**: 117–146. Elsevier B.V. doi:10.1016/j.earscirev.2015.01.011.
- Marincovich, L. 2000. Central American paleogeography controlled Pliocene Arctic Ocean molluscan migrations. *Geology*, **28**: 551–554. doi:10.1130/0091-7613(2000)028<0551:CAPCPA>2.3.CO;2.
- Masson-Delmotte, V., Schulz, M., Abe-Ouchi, A., Beer, J., Ganopolski, A., González Rouco, J.F., Jansen, E., Lambeck, K., Luterbacher, J., Naish, T., Osborn, T., Otto-Bliesner, B., Quinn, T., Ramesh, R., Rojas, M., Shao, X., and Timmermann, A. 2013. Information from paleoclimate archives. *In* *Climate Change 2013 the Physical Science Basis: Working Group I Contribution to the Fifth Assessment Report of the Intergovernmental Panel on Climate Change*. doi:10.1017/CBO9781107415324.013.
- Matthews, J. V., Mott, R.J., and Vincent, J.-S. 1986. Preglacial and Interglacial Environments of Banks Island : Pollen and Macrofossils from Duck Hawk Bluffs and Related Sites. *Geographie Physique et Quaternaire*, **40**: 279–298.
- Matthews, J. V., and Ovensen, L.E. 1990. Late Tertiary plant macrofossils from localities in Arctic/sub- Arctic North America: a review of the data. *Arctic*, **43**: 364–392. doi:10.14430/arctic1631.

- Matthews, J. V., Telka, A., and Kuzmina, S.A. 2019. Late Neogene Insect and other Invertebrate Fossils from Alaska and Arctic/Subarctic Canada. *Invertebrate Zoology*, **16**: 126–153. doi:10.15298/invertzool.16.2.03.
- Matthews, J. V. 1989. New Information On the Flora and Age of the Beaufort Formation, Arctic Archipelago, and Related Tertiary Deposits in Alaska. Current Research, Part D, Interior Plains and Arctic Canada, Geological Survey of Canada, **89**: 105–111. doi:10.4095/126704.
- Matthiessen, J., Knies, J., Vogt, C., and Stein, R. 2009. Pliocene palaeoceanography of the Arctic Ocean and subarctic seas. *Philosophical Transactions of the Royal Society A: Mathematical, Physical and Engineering Sciences*, **367**: 21–48. doi:10.1098/rsta.2008.0203.
- McNeil, D.H., Dietrich, J.R., and Dixon, J. 1990. Foraminiferal Biostratigraphy and Seismic Sequences: Examples from the Cenozoic of the Beaufort-Mackenzie Basin, Arctic Canada. *In* *Paleoecology, Biostratigraphy, Paleoceanography and Taxonomy of Agglutinated Foraminifera*. Springer Netherlands, Dordrecht. pp. 859–882. doi:10.1007/978-94-011-3350-0_32.
- McNeil, D.H., Duk-Rodkin, A., Dixon, J., Dietrich, J.R., White, J.M., Miller, K.G., and Issler, D.R. 2001. Sequence stratigraphy, biotic change, $^{87}\text{Sr}/^{86}\text{Sr}$ record, paleoclimatic history, and sedimentation rate change across a regional late Cenozoic unconformity in Arctic Canada. *Canadian Journal of Earth Sciences*, **38**: 309–331. doi:10.1139/cjes-38-2-309.
- Mecham, G.F. 1855. Further Papers relative to the Recent Arctic Expedition. *In* *Search of Sir John Franklin and the crews of H.M.S“ Erebus” and “Terror.”* London: H.M. Stationery Office. pp. 499–540.
- Merchel, S., Gärtner, A., Beutner, S., Bookhagen, B., and Chabilan, A. 2019. Attempts to understand potential deficiencies in chemical procedures for AMS: Cleaning and dissolving quartz for ^{10}Be and ^{26}Al analysis. *Nuclear Instruments and Methods in Physics Research, Section B: Beam Interactions with Materials and Atoms*, **455**: 293–299. Elsevier. doi:10.1016/j.nimb.2019.02.007.
- Miall, A.D. 1977. Lithofacies types and vertical profile models in braided river deposits: a summary. *Fluvial Sedimentology*, **5**: 597–600.
- Miall, A.D. 1979. Mesozoic and tertiary geology of Banks Island, Arctic Canada, the history of an unstable craton margin. *Geological Survey of Canada Memoir*,: 235. doi:10.4095/105620.
- Miall, A.D. 1992. Facies Models: response to sea level changes. *In* *Facies Models: response to sea level changes*. Edited by R.G. Walker and N.P. James. St. John's. pp. 119–142.

- Miall, A.D. 1996. Methods of Architectural-Element Analysis. *In* The Geology of Fluvial Deposits: Sedimentary Facies, Basin Analysis, and Petroleum Geology. Springer Berlin Heidelberg, Berlin, Heidelberg. pp. 75–98. doi:10.1007/978-3-662-03237-4_4.
- Miller, K.G., Browning, J. V., Schmelz, W.J., Kopp, R.E., Mountain, G.S., and Wright, J.D. 2020. Cenozoic sea level and cryospheric evolution from deep-sea geochemical and continental margin records. *Science Advances*, **6**: eaaz1346. doi:10.1126/sciadv.aaz1346.
- Mitchell, W.T., Rybczynski, N., Schröder-Adams, C., Hamilton, P.B., Smith, R., and Douglas, M. 2016. Stratigraphic and paleoenvironmental reconstruction of a mid-pliocene fossil site in the high arctic (Ellesmere Island, Nunavut): Evidence of an ancient peatland with beaver activity. *Arctic*, **69**: 185–204. doi:10.14430/arctic4567.
- Mitchum Jr, R.M., Vail, P.R., and Thompson III, S. 1977. Seismic stratigraphy and global changes of sea level: Part 2. The depositional sequence as a basic unit for stratigraphic analysis: Section 2. Application of seismic reflection configuration to stratigraphic interpretation. *In* AAPG Memoir 26: Seismic Stratigraphy-Applications to Hydrocarbon Exploration.
- Montelli, A., Dowdeswell, J.A., Ottesen, D., and Johansen, S.E. 2017. Ice-sheet dynamics through the Quaternary on the mid-Norwegian continental margin inferred from 3D seismic data. *Marine and Petroleum Geology*, **80**: 228–242. Elsevier Ltd. doi:10.1016/j.marpetgeo.2016.12.002.
- Mosher, D.C., Shimeld, J., Hutchinson, D., Chian, D., Lebedova-Ivanova, N., and Jackson, R. 2012. Canada Basin Revealed. *In* OTC Arctic Technology Conference. Offshore Technology Conference. doi:10.4043/23797-MS.
- Mudelsee, M., and Raymo, M.E. 2005. Slow dynamics of the Northern Hemisphere glaciation. *Paleoceanography*, **20**. doi:10.1029/2005PA001153.
- Nishiizumi, K. 2004. Preparation of ²⁶Al AMS standards. *Nuclear Instruments and Methods in Physics Research, Section B: Beam Interactions with Materials and Atoms*, **223–224**: 388–392. doi:10.1016/j.nimb.2004.04.075.
- Nishiizumi, K., Imamura, M., Caffee, M.W., Southon, J.R., Finkel, R.C., and McAninch, J. 2007. Absolute calibration of ¹⁰Be AMS standards. *Nuclear Instruments and Methods in Physics Research, Section B: Beam Interactions with Materials and Atoms*, **258**: 403–413. doi:10.1016/j.nimb.2007.01.297.
- Nishiizumi, K., Kohl, C.P., Shoemaker, E.M., Arnold, J.R., Klein, J., Fink, D., and Middleton, R. 1991. In situ ¹⁰Be-²⁶Al exposure ages at Meteor Crater, Arizona. *Geochimica et Cosmochimica Acta*, **55**: 2699–2703. doi:10.1016/0016-7037(91)90388-L.

- Oakey, G.N., and Saltus, R.W. 2016. Geophysical analysis of the Alpha–Mendeleev ridge complex: Characterization of the High Arctic Large Igneous Province. *Tectonophysics*, **691**: 65–84. The Authors. doi:10.1016/j.tecto.2016.08.005.
- Pagani, M., Liu, Z., Lariviere, J., and Ravelo, A.C. 2010. High Earth-system climate sensitivity determined from Pliocene carbon dioxide concentrations. *Nature Geoscience*, **3**: 27–30. Nature Publishing Group. doi:10.1038/ngeo724.
- Pelletier, B.R. 1966. Development of Submarine Physiography in the Canadian Arctic and Its Relation to Crustal Movements. *In Continental Drift. Edited by G.D. Garland.* University of Toronto Press, Toronto. pp. 77–101. doi:10.3138/9781487595678-008.
- Piepjohn, K., Atkinson, E., Dewing, K., Smith, R., and Galloway, J. 2018. Cenozoic structural evolution on northern Banks Island, N.W.T. Canada. *Arktos*, **4**: 1–19. Springer International Publishing. doi:10.1007/s41063-018-0046-y.
- Piper, D.J.W., and Normark, W.R. 1989. Late Cenozoic sea level changes and the onset of glaciation: impact on continental slope progradation off eastern Canada. *Marine and Petroleum Geology*, **6**: 336–347. doi:10.1016/0264-8172(89)90030-5.
- Pollard, D., Gomez, N., DeConto, R.M., and Han, H.K. 2018. Estimating Modern Elevations of Pliocene Shorelines Using a Coupled Ice Sheet–Earth–Sea Level Model. *Journal of Geophysical Research: Earth Surface*, **123**: 2279–2291. doi:10.1029/2018JF004745.
- Porębski, S.J., and Steel, R.J. 2003. Shelf-margin deltas: Their stratigraphic significance and relation to deepwater sands. *Earth-Science Reviews*, **62**: 283–326. doi:10.1016/S0012-8252(02)00161-7.
- Porter, C., Morin, P., Howat, I., Noh, M-J., Bates, B., Peterman, K., Keesey, S., Schlenk, M., Gardiner, J., Tomko, K., Willis, M., Kelleher, C., Cloutier, M., Husby, E. Foga, S., Nakamura, H., Platson, M., Wethington, M., Williamson, C., Bauer, G., Enos, J., Arnold, G., Kramer, W., Becker, P., Doshi, A., D’Souza, C., Cummens, P., Laurier, F., Bojesen, M. 2018. “ArcticDEM”, <https://doi.org/10.7910/DVN/OHHUKH>, Harvard Dataverse, V1, [June 2017].
- Powell, J.W., Issler, D.R., Schneider, D.A., Fallas, K.M., and Stockli, D.F. 2020. Thermal history of the Mackenzie Plain, Northwest Territories, Canada: Insights from low-temperature thermochronology of the Devonian Imperial Formation. *Bulletin of the Geological Society of America*, **132**: 767–783. doi:10.1130/B35089.1.
- Ramachandran, K., Brent, T., Bellefleur, G., Dallimore, S., and Riedel, M. 2011. Imaging permafrost velocity structure using high resolution 3D seismic tomography. 78th Society of Exploration Geophysicists International Exposition and Annual Meeting, SEG 2008, **76**: 3300–3304.

- Raymo, M.E., Kozdon, R., Evans, D., Lisiecki, L., and Ford, H.L. 2018. The accuracy of mid-Pliocene $\delta^{18}\text{O}$ -based ice volume and sea level reconstructions. *Earth-Science Reviews*, **177**: 291–302. Elsevier. doi:10.1016/j.earscirev.2017.11.022.
- Raymo, M.E., Mitrovica, J.X., O’Leary, M.J., Deconto, R.M., and Hearty, P.J. 2011. Departures from eustasy in Pliocene sea level records. *Nature Geoscience*, **4**: 328–332. Nature Publishing Group. doi:10.1038/ngeo1118.
- Riedel, M., Brent, T.A., Taylor, G., Taylor, A.E., Hong, J.K., Jin, Y.K., and Dallimore, S.R. 2017. Evidence for gas hydrate occurrences in the Canadian Arctic Beaufort Sea within permafrost-associated shelf and deep-water marine environments. *Marine and Petroleum Geology*, **81**: 66–78. Elsevier Ltd. doi:10.1016/j.marpetgeo.2016.12.027.
- Robinson, M.M., Dowsett, H.J., Dwyer, G.S., and Lawrence, K.T. 2008. Reevaluation of mid-Pliocene North Atlantic sea surface temperatures. *Paleoceanography*, **23**: 1–9. doi:10.1029/2008PA001608.
- Rohr, K.M.M., Riedel, M., Dallimore, S.R., and Côté, M.M. 2016. Slope fan and glacial sedimentation on the central Beaufort continental slope, Arctic Canada. *Marine and Petroleum Geology*, .
- Rybczynski, N., Gosse, J.C., Richard Harington, C., Wogelius, R.A., Hidy, A.J., and Buckley, M. 2013. Mid-Pliocene warm-period deposits in the High Arctic yield insight into camel evolution. *Nature Communications*, **4**: 1550–1559. Nature Publishing Group. doi:10.1038/ncomms2516.
- Sangree, J.B., and Widmier, J.M. 1979. Interpretation of depositional facies from seismic data. *Geophysics*, **44**: 131–160. doi:10.1190/1.1440957.
- Smith, I.R. 2020. Kimberlite indicator-mineral studies on Banks Island, Northwest Territories: assessing the potential for diamond-bearing kimberlite. *In Geological Survey of Canada*. doi:10.4095/326157.
- Stokes, C.R., Clark, C.D., Darby, D.A., and Hodgson, D.A. 2005. Late Pleistocene ice export events into the Arctic Ocean from the M’Clure Strait Ice Stream, Canadian Arctic Archipelago. *Global and Planetary Change*, **49**: 139–162. doi:10.1016/j.gloplacha.2005.06.001.
- Stone, J.O. 2000. Air pressure and cosmogenic isotope production. *Journal of Geophysical Research*, **105**: 753–759.
- Taylor, R.B., and Hodgson, D.A. 1991. Coastal Studies in the Canadian Arctic Archipelago, Brock, Devon, Prince Patrick and the Polynia Islands, N.W.T. *In Geological Survey of Canada*. doi:10.4095/132383.
- Tedford, R.H., and Harington, C.R. 2003. An arctic mammal fauna from the Early Pliocene of North America. *Nature*, **425**: 388–390. doi:10.1038/nature01892.

- Tozer, E.T. 1956. Geological reconnaissance Prince Patrick, Eglinton and western Melville Islands, Arctic Archipelago, Northwest Territories. Geological Survey of Canada, **55**: 32.
- Tozer, E.T., and Thorsteinsson, R. 1964. Western Queen Elizabeth Islands, Arctic Archipelago. *In* Geological Survey of Canada Memoir 332. doi:10.4095/100556.
- Vail, R., Mitchum, R.M.J., Todd, R.G., Widmier, J.M., Thompson III, S., Sangree, J.B., Bubb, N., and Hatlelid, W.G. 1977. Seismic stratigraphy and global changes of sea level. *In* Seismic Stratigraphy -- Applications to Hydrocarbon Exploration, American Association of Petroleum Geologists.
- Valk, T. Van Der, Pečnerová, P., Díez-del-molino, D., Bergström, A., Oppenheimer, J., Hartmann, S., Xenikoudakis, G., Thomas, J.A., Dehasque, M., Sağlıcan, E., Fidan, F.R., Barnes, I., Liu, S., Somel, M., Heintzman, P.D., Nikolskiy, P., Shapiro, B., Skoglund, P., Hofreiter, M., Lister, A., Götherström, A., and Dalén, L. 2021. Million-year-old DNA sheds light on the genomic history of mammoths. *Nature*, **591**: 265–269. doi:10.1038/s41586-021-03224-9.
- Vaughan, J.M., England, J.H., and Evans, D.J.A. 2014. Glaciotectonic deformation and reinterpretation of the Worth Point stratigraphic sequence: Banks Island, NT, Canada. *Quaternary Science Reviews*, **91**: 124–145. Elsevier Ltd. doi:10.1016/j.quascirev.2013.11.005.
- Vincent, J.-S. 1983. La géologie du quaternaire et la géomorphologie de l'île Banks, arctique canadien. *In* Geological Survey of Canada Memoir 405. Cambridge. doi:10.4095/119517.
- Vincent, J.S., Occhietti, S., Rutter, N., Lortie, G., Guilbault, J., and De Boutray, B. 1983. The late Tertiary- Quaternary stratigraphic record of the Duck Hawk Bluffs, Banks Island, Canadian Arctic Archipelago. *Canadian Journal of Earth Sciences*, **20**: 1694–1712. doi:10.1139/e83-160.
- Wellner, J.S., Lowe, A.L., Shipp, S.S., and Anderson, J.B. 2001. Distribution of glacial geomorphic features on the Antarctic continental shelf and correlation with substrate: Implications for ice behavior. *Journal of Glaciology*, **47**: 397–411. doi:10.3189/172756501781832043.
- Williams, C.J., Mendell, E.K., Murphy, J., Court, W.M., Johnson, A.H., and Richter, S.L. 2008. Paleoenvironmental reconstruction of a Middle Miocene forest from the western Canadian Arctic. *Palaeogeography, Palaeoclimatology, Palaeoecology*, **261**: 160–176. doi:10.1016/j.palaeo.2008.01.014.
- Wolfe, J.A. 1981. A chronologic framework for Cenozoic megafossil floras of northwestern North America and its relation to marine geochronology. *Geological Society of America Special Paper 184*,: 39–47. doi:10.1130/SPE184-p39.

Appendix A. Supplementary File to Chapter 2

A.1 Isochron Samples



Figure A.1. Sample PPI-17-103-001



Figure A.2. Sample PPI-17-103-002



Figure A.3. Sample PPI-17-103-007

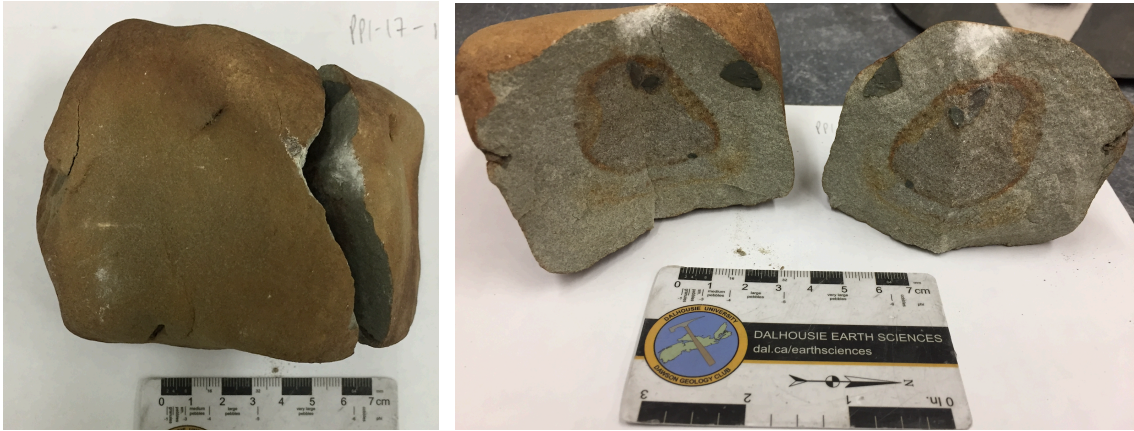


Figure A.4. Sample PPI-17-103-008



Figure A.5. Sample PPI-17-103-009

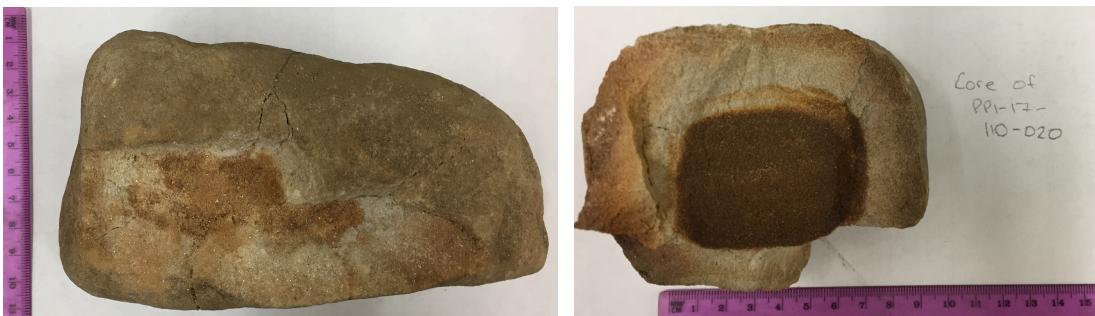
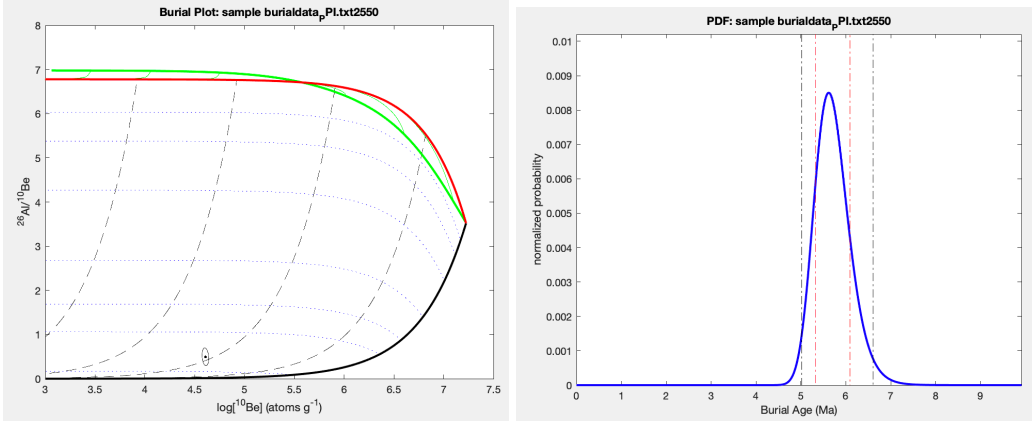


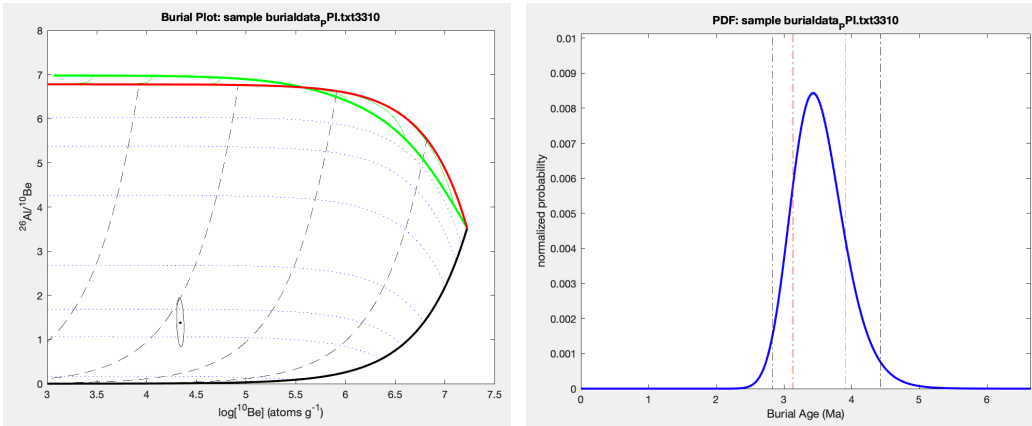
Figure A.6. Sample PPI-17-110-020

A2 Burial Age Dating Plots with Probability Distributions

Simple Burial Plot Sample PPI-17-103-006



Simple Burial Plot Sample PPI-17-105-017



Appendix B. Data Tables and Chemical Worksheets

Table B.1. Clast lithology of 97 clasts sampled within the gravel facies section above unconformity, section D8

Type of Lithology	Count
Fine grained quartzite	21
Fine grained quartzite with porous calcite holes	19
Quartz Sandstone, light grey – yellow	16
Garnetiferous fine to medium meta quartz arenite	13
Black stained fine quartz arenite	4
Beige fine quartz sandstone	4
Unlithified feldspar/garnet bearing quartz arenite	4
Light red medium quartz sandstone	4
Brown very fine – fine quartz sandstone	3
Green, grey fine quartz sandstone	3
Pink Quartz medium arenite, loosely recrystallized	2
Coarse grained quartzite	2
Granitic gneiss	1
Black chert	1

Table B.2. Average ^{27}Al current per sample during each run

Sample ID	AMS ID	Avg ^{27}Al current (microAmps) per run				
4096	AL14393	1.21	1.16	0.94	0.64	
3531	AL14394	1.11	0.91	0.67	0.72	
3533	AL14396	1.18	1.12	0.82	0.87	0.65
3536	AL14397	1.10	0.73	0.67	0.49	0.54
3537	AL14398	1.08	0.90	0.78	0.55	

Sample ID	AMS ID	Avg ²⁷ Al current (microAmps) per run					
3914	AL14399	0.78	0.61	0.58	0.52		
3538	AL14400	1.03	0.24	0.11			
3546	AL14401	0.88	0.67	0.69	0.53	0.41	
3549	AL14402	1.06	0.81	0.71	0.59		
3550	AL14403	0.84	0.79	0.56	0.68	0.53	0.48

Table B.3. Average ⁹Be current per sample during each run

Sample ID	AMS ID	Avg ⁹ Be current (microAmps) per run					
JG3985	BE49124	21.2	20.5	19.0	17.1		
JG3531	BE49125	25.1	21.3	19.6	18.8		
JG3533	BE49126	14.9	15.0	13.9	11.8	11.2	10.5
JG3536	BE49127	17.4	14.8	13.8			
JG3537	BE49128	18.3	17.5	15.8	15.1	14.5	
JG3914	BE49129	18.9	17.4	16.2	14.8	12.6	10.1
JG3538	BE49130	22.7	21.7	18.7	14.5	14.8	10.7
JG3546	BE49131	19.2	17.0	15.2	14.0		
JG3549	BE49132	19.5	17.1	16.0	14.2	9.0	8.3
JG3550	BE49133	21.6	19.7	19.7	19.3		
JG4096	BE49173	18.4	18.3	16.0			

B.1 AMS- Standard Corrected Output

Table B.4. ²⁶Al AMS data. Standard used for normalization: KNSTD 30960 (K. Nishiizumi);
26/27 ratio for standard =0.00000000003096.

Sample ID	AMS ID	run	r into r std	Int error	Ext error	²⁶ Al/ ²⁷ Al Ratio		²⁶ Al/ ²⁷ Al Ratio (Corr. For BKGD)		Error/Ratio*100
						Al ratio	Ratio err	²⁶ Al/ ²⁷ Al ratio	Error	
			x10 ⁻⁵	x10 ⁻⁵	x10 ⁻⁴	x10 ⁻¹⁵	x10 ⁻¹⁵	x10 ⁻¹⁵	x10 ⁻¹⁵	
4096	14393	1	8.01	3.58	0	2.48	1.108	2.480	1.108	47%
3531	14394	1	42.8	8.93	0	13.25	2.765	13.25	2.765	20.9%

Sample ID	AMS ID	run	r into r std	Int error	Ext error	²⁶ Al/ ²⁷ Al Ratio		²⁶ Al/ ²⁷ Al Ratio (Corr. For BKGD)		Error/Ratio*100
						Al ratio	Ratio err	²⁶ Al/ ²⁷ Al ratio	Error	
			x10 ⁻⁵	x10 ⁻⁵	x10 ⁻⁴	x10 ⁻¹⁵	x10 ⁻¹⁵	x10 ⁻¹⁵	x10 ⁻¹⁵	
3533	14396	1	35.34	6.93	0	10.94	2.146	10.94	2.146	19.6%
3536	14397	1	64.39	10.74	0	19.94	3.325	19.94	3.325	16.7%
3537	14398	1	17.11	5.7	0	5.297	1.765	5.297	1.765	33.3%
3914	14399	1	32.96	9.14	0	10.20	2.830	10.20	2.830	27.7%
3538	14400	1	9.73	6.88	0	3.012	2.130	3.012	2.130	70.7%
3546	14401	1	73.48	12.09	0	22.75	3.743	22.75	3.743	16.5%
3549	14402	1	28.01	7.49	0	8.672	2.319	8.672	2.319	26.7%
3550	14403	6	528.2	29.24	1.679	163.5	0.053	163.5	9.053	5.5%

Table B.5. ¹⁰Be AMS results. Standard used for normalization: 07KNSTD3110 (K. Nishiizumi); 10/9 ratio for standard = 2.85x10⁻¹². Boron correction factor = (0.8±0.1)x10⁻⁴

Sample ID	AMS ID	runs	r into r std	Int error	Ext error	¹⁰ Be/ ⁹ Be Ratio		¹⁰ Be/ ⁹ Be Ratio (Corr. For BKGD)		(Error/Ratio)*100
						Be ratio	Ratio err	¹⁰ Be/ ⁹ Be Ratio	Error	
			x10 ⁻⁴	x10 ⁻⁴	x10 ⁻⁴	x10 ⁻¹⁵	x10 ⁻¹⁵	x10 ⁻¹⁵	x10 ⁻¹⁵	
3985	49124	4	7.867	0.774	1.425	2.242	4.061	2.242	40.6	18.1%
3531	49125	4	214.0	3.926	3.23	60.99	1.119	60.99	1.12	1.8%
3533	49126	6	65.857	2.253	3.275	18.77	0.9334	18.77	93.3	5.0%
3536	49127	3	279.575	6.088	2.837	79.68	1.735	79.68	1.74	2.2%
3537	49128	5	81.589	2.451	2.398	23.25	0.6985	23.25	69.9	3.0%
3914	49129	6	55.078	1.909	2.132	15.70	0.6076	15.70	60.8	3.9%
3538	49130	6	41.858	1.558	1.383	11.93	0.4440	11.93	44.4	3.7%

Sample ID	AMS ID	runs	r into r std	Int error	Ext error	¹⁰ Be/ ⁹ Be Ratio		¹⁰ Be/ ⁹ Be Ratio (Corr. For BKGD)		(Error/Ratio) *100
						Be ratio	Ratio err	¹⁰ Be/ ⁹ Be Ratio	Error	
			x10 ⁻⁴	x10 ⁻⁴	x10 ⁻⁴	x10 ⁻¹⁵	x10 ⁻¹⁵	x10 ⁻¹⁵	x10 ⁻¹⁵	
3546	49131	4	157.78 1	3.826	3.238	44.97	1.090	44.97	1.09	2.4%
3549	49132	6	49.981	1.924	1.781	14.24	0.5483	14.24	54.8	3.8%
3550	49133	4	5.06	10.83 9	13.707	192.0	3.906	192.0	3.91	2.0%

B.2 ICP Results and Data Reduction

Table B.6. ICP Results

Lab ID	Mass in test tube + aliquot before nitric	Aliquot mass (g)	add 2%HN O ₃ (g)	Total mass (g)	meas conc	meas conc	meas conc	meas conc	meas conc	meas conc	in the ~5ml aliquot from 100 ml	mass of soln in 100 ml vol, inc carrier if added, b/f taking aliquot	Total Al mass in volumetric	Mass of soln used for making target	Total Al mass in target
		g	g	g	µg/ml	µg/ml	µg/ml	µg/ml	µg/ml	µg	µg/g	g	µg	g	µg
3531 A	10.3676	4.9767	9.0922	14.0689	7.9742	7.9335	7.8434	0.7853	0.7847	111.4	22.38	101.1161	2263.09	96.139	2152
3533 A	10.1232	4.7334	9.2513	13.9847	9.3919	9.3466	9.3247	0.7494	0.7423	130.8	27.64	101.1042	2794.25	96.371	2663
3536 A	10.039	4.6812	9.5392	14.2204	3.9538	3.9713	3.9	0.7011	0.7039	56.1	11.97	101.2044	1211.82	96.523	--
3536 B	9.9948	4.6274	9.3442	13.9716	5.5291	5.4989	5.4784	0.7011	0.7034	76.9	16.61	96.8734	1609.33	92.246	1532

Lab ID	Mass in test tube + aliquot before nitric	Aliquot mass (g)	add 2%HN O ₃ (g)	Total mass (g)	meas conc µg/ml	meas conc µg/ml	meas conc µg/ml	meas conc µg/ml	meas conc µg/ml	meas conc µg	in the ~5ml aliquot from 100 ml µg/g	mass of soln in 100 ml vol, inc carrier if added, b/f taking aliquot g	Total Al mass in volumetric µg	Mass of soln used for making target g	Total Al mass in target µg
3537 A	10.1164	4.789	9.3316	14.1206	10.1419	10.1105	10.1159	0.7449	0.7471	142.9	29.85	101.1810	3020.00	96.392	2877
3914 A	10.348	4.9632	9.3593	14.3225	6.9715	6.9464	6.9304	0.7571	0.7627	99.5	20.05	101.0687	2026.86	96.106	1927
3538 A	10.0258	4.6505	9.7849	14.4354	3.4898	3.5095	3.413	0.5921	0.6029	50.1	10.77	101.1735	1089.99	96.523	1040
3546 A	10.3265	4.895	9.2956	14.1906	7.1966	7.1635	7.1678	0.7773	0.7854	101.8	20.80	101.1670	2104.59	96.272	2003
3549 A	10.2677	4.9167	9.1507	14.0674	11.7056	11.6653	11.6912	1.0161	1.0215	164.4	33.44	101.2069	3384.28	96.290	3220
3550 A	10.2694	4.8767	8.9968	13.8735	5.7873	5.7326	5.7923	0.7775	0.7849	80.1	16.42	101.1917	1661.25	96.315	--

Lab ID	Mass in test tube + aliquot before nitric	Aliquot mass (g)	add 2%HN O ₃ (g)	Total mass (g)	meas conc	meas conc	meas conc	meas conc	meas conc	meas conc	in the ~5ml aliquot from 100 ml	mass of soln in 100 ml vol, inc carrier if added, b/f taking aliquot	Total Al mass in volumetric	Mass of soln used for making target	Total Al mass in target
		g	g	g	µg/ml	µg/ml	µg/ml	µg/ml	µg/ml	µg	µg/g	g	µg	g	µg
3550 B	10.2231	4.7871	9.1488	13.9359	7.126	7.0679	7.126	0.759	0.7698	99.0	20.69	96.7184	2000.95	91.931	1902
4096 A	9.5374	4.6970	9.937	14.6340	0	0	0	0.7524	0.7691	0.0	0.00	101.0698	0.00	96.373	--
4096 B	10.1339	4.7753	9.357	14.1323	10.1328	10.0571	10.2196	0.712	0.7299	143.3	30.00	99.3398	2980.05	94.565	2837

Table B.7. ²⁶Al data reduction. Al carrier ID: Alfa Aesar-Al 1000 ug/ml ICPMS std. ²⁷Al measured by ICP-OES.

Lab ID	Carrier Mass in blank	²⁷ Al Carrier Conc	Al Carrier Density	Al mass in carrier added	²⁷ Al in carrier	²⁶ Al/ ²⁷ Al (not corr) blank	²⁶ Al/ ²⁷ Al (not corr) error	²⁶ Al atoms in blank	²⁶ Al atoms in blank error	blank error	²⁷ Al in total sample	²⁶ Al/ ²⁷ Al AMS (not blk corr)	²⁶ Al/ ²⁷ Al AMS (not blk corr) 1σ error	AMS error (1σ)	²⁶ Al atoms not 'processed'	²⁶ Al atoms processed
	g	g/mL	g/mL	²⁷ Al	Atoms x10 ¹⁹	²⁶ Al/ ²⁷ Al x10 ¹⁵	²⁶ Al/ ²⁷ Al x10 ¹⁵	atoms x10 ⁵	atoms x10 ⁴	frac	atoms x10 ¹⁹	²⁶ Al/ ²⁷ Al x10 ¹⁴	²⁶ Al/ ²⁷ Al x10 ¹⁵	%	atoms x10 ⁵	atoms x10 ⁵
JG3531	0	1000	1.013	0.0	0	2.480	1.108	1.626	7.27	0.4469	5.051	1.33	2.76	0.21	6.69	5.07
JG3533	0	1000	1.013	0.0	0	2.480	1.108	1.626	7.27	0.4469	6.237	1.09	2.15	0.20	6.82	5.20
JG3536	0.4538	1000	1.013	448.0	9.999	2.480	1.108	1.626	7.27	0.4469	3.592	1.99	3.33	0.17	7.16	5.54
JG3537	0	1000	1.013	0.0	0	2.480	1.108	1.626	7.27	0.4469	6.741	0.530	1.76	0.33	3.57	1.95
JG3914	0	1000	1.013	0.0	0	2.480	1.108	1.626	7.27	0.4469	4.524	1.02	2.83	0.28	4.62	2.99
JG3538	0	1000	1.013	0.0	0	2.480	1.108	1.626	7.27	0.4469	2.433	0.301	2.13	0.71	.733	-0.893
JG3546	0	1000	1.013	0.0	0	2.480	1.108	1.626	7.27	0.4469	4.697	2.27	3.74	0.16	0.0107	9.06

Lab ID	Carrier Mass in blank	²⁷ Al Carrier Conc	Al Carrier Density	Al mass in carrier added	²⁷ Al in carrier	²⁶ Al/ ²⁷ Al (not bkgd corr) blank	²⁶ Al/ ²⁷ Al (not bkgd corr) error	²⁶ Al atoms in blank	²⁶ Al atoms in blank error	blank error	²⁷ Al in total sample	²⁶ Al/ ²⁷ Al AMS (not blk corr)	²⁶ Al/ ²⁷ Al AMS (not blk corr) 1σ error	AMS error (1σ)	²⁶ Al atoms not 'process' corrected	²⁶ Al atoms process corrected
	g	g/mL	g/mL	²⁷ Al	Atoms x10 ¹⁹	²⁶ Al/ ²⁷ Al x10 ¹⁵	²⁶ Al/ ²⁷ Al x10 ¹⁵	atoms x10 ⁵	atoms x10 ⁴	frac	atoms x10 ¹⁹	²⁶ Al/ ²⁷ Al x10 ⁻¹⁴	²⁶ Al/ ²⁷ Al x10 ⁻¹⁵	%	atoms x10 ⁵	atoms x10 ⁵
JG3549	0	1000	1.013	0.0	0	2.480	1.108	1.626	7.27	0.4469	7.554	0.867	2.32	0.27	6.55	4.92
JG3550	0.4056	1000	1.013	400.4	0.8937	2.480	1.108	1.626	7.27	0.4469	4.466	16.4	9.05	0.06	0.0730	71.4
JG4096	2.975	1000	1.013	2936.8	6.555	2.480	1.11	1.626	7.27	0.4469	6.652					

Table B.8. ^{10}Be data reduction. Be carrier ID: PRIME lab carrier Bottle 5

Lab ID	Be Carrier Mass	Be Carrier conc	Be Carrier density	^9Be added through carrier	$^{10}\text{Be}/^9\text{Be}$ blank boron corr	$^{10}\text{Be}/^9\text{Be}$ blank error	^{10}Be atoms in blank	$^{10}\text{Be}/^9\text{Be}$ AMS boron corr	1σ Error	AMS 1σ Error	^{10}Be atoms	^{10}Be atoms blnk corr	^{10}Be atoms error	^{10}Be atoms error
	g	mg/mL	g/mL	atoms ^9Be $\times 10^{19}$	$^{10}\text{Be}/^9\text{Be}$ $\times 10^{-15}$	$^{10}\text{Be}/^9\text{Be}$ $\times 10^{-16}$	atoms $\times 10^4$	$^{10}\text{Be}/^9\text{Be}$ $\times 10^{-14}$	$^{10}\text{Be}/^9\text{Be}$ $\times 10^{-16}$	frac	atoms $\times 10^5$	Atoms $\times 10^5$	atoms	%
JG3985	0.2153	1046	1.013	1.486	2.242	4.061	3.331							
JG3531	0.2178	1046	1.013	1.503	2.240	4.060	3.331	6.099	11.19	1.8%	9.17	8.83	2.01E+04	2.78%
JG3533	0.2158	1046	1.013	1.489	2.240	4.060	3.331	1.877	9.334	5.0%	2.79	2.46	1.54E+04	7.10%
JG3536	0.2101	1046	1.013	1.450	2.240	4.060	3.331	7.968	17.35	2.2%	0.116	0.112	2.83E+04	3.24%
JG3537	0.2158	1046	1.013	1.489	2.240	4.060	3.331	2.325	6.985	3.0%	3.46	3.13	1.25E+04	4.36%
JG3914	0.2159	1046	1.013	1.490	2.240	4.060	3.331	1.570	6.076	3.9%	2.34	2.01	1.11E+04	5.56%
JG3538	0.2182	1046	1.013	1.506	2.240	4.060	3.331	1.193	4.440	3.7%	1.80	1.46	9.23E+03	5.36%
JG3546	0.2225	1046	1.013	1.535	2.240	4.060	3.331	4.497	10.90	2.4%	6.90	6.57	1.92E+04	3.57%
JG3549	0.2124	1046	1.013	1.466	2.240	4.060	3.331	1.424	5.483	3.8%	2.09	1.75	1.02E+04	5.54%
JG3550	0.2200	1046	1.013	1.518	2.240	4.060	3.331	19.20	39.06	2.0%	0.291	0.288	6.64E+04	3.05%
JG4096	0.2119	1046	1.013	1.462	1.44	2.16	2.11							

B.3 Chemical Worksheets for TCN Data

Step1 Carrier Addition

Chemist: **SS/GY** Date: **10-01-20**

	1	2	3	4	5	6	7	8	9	10	11
CNEF ID	3531	3533	3536	3537	3914	3538	3546	3549	3550	3985	4096
Sample ID	PPI-17-103-001	PPI-17-103-003	PPI-17-103-006	PPI-17-103-007	PPI-17-103-008	PPI-17-103-009	PPI-17-105-017	PPI-17-110-020	PPI-17-401-022	blank Be only	Blank Al+ Be
Digestion vessel ID	B1	B2	B3	B4	B5	B6	B9	B12	B27	B30	B32
Beryl Carrier ID	PRIME lab carrier bottle #5 (Aug 2020) 1046 ppm										

Verify Be carrier level mark on bottle Yes y/n
Mass Be carrier bottle with cap g before g after carrier added.

Antistatic gloves, door locked, all materials at room temperature, balance clean and connected to MS Excel
 Pour 10 ml carrier into cleaned 15 ml beaker that is rinsed with a drop of carrier

Mass vessel no cap	<input type="text"/>	<input type="text"/>	<input type="text"/>	<input type="text"/>	<input type="text"/>	<input type="text"/>	<input type="text"/>	<input type="text"/>	<input type="text"/>	<input type="text"/>	<input type="text"/>
--------------------	----------------------	----------------------	----------------------	----------------------	----------------------	----------------------	----------------------	----------------------	----------------------	----------------------	----------------------

Place vessel on paper next to balance, TARE, suck <1 ml carrier into fine transfer pipette

Mass pipette before transfer	<input type="text"/>	<input type="text"/>	<input type="text"/>	<input type="text"/>	<input type="text"/>	<input type="text"/>	<input type="text"/>	<input type="text"/>	<input type="text"/>	<input type="text"/>	<input type="text"/>
------------------------------	----------------------	----------------------	----------------------	----------------------	----------------------	----------------------	----------------------	----------------------	----------------------	----------------------	----------------------

Transfer desired volume carrier to vessel

Mass pipette after transfer	<input type="text"/>	<input type="text"/>	<input type="text"/>	<input type="text"/>	<input type="text"/>	<input type="text"/>	<input type="text"/>	<input type="text"/>	<input type="text"/>	<input type="text"/>	<input type="text"/>
Mass vessel after transfer	<input type="text"/>	<input type="text"/>	<input type="text"/>	<input type="text"/>	<input type="text"/>	<input type="text"/>	<input type="text"/>	<input type="text"/>	<input type="text"/>	<input type="text"/>	<input type="text"/>

MASS CARRIER	0.2178	0.2158	0.2101	0.2158	0.2159	0.2182	0.2225	0.2124	0.22	0.2153	0.2119
Carrier mass estimate from vessel	<input type="text"/>	<input type="text"/>	<input type="text"/>	<input type="text"/>	<input type="text"/>	<input type="text"/>	<input type="text"/>	<input type="text"/>	<input type="text"/>	<input type="text"/>	<input type="text"/>
MASS CARRIER = Carrier mass estimate? (Y/N)	#DIV/0!	#DIV/0!	#DIV/0!	#DIV/0!	#DIV/0!	#DIV/0!	#DIV/0!	#DIV/0!	#DIV/0!	#DIV/0!	#DIV/0!

TARE, add quartz

MASS QUARTZ	30.0244	30.0758	27.6375	30.0398	30.0539	25.1894	30.0802	30.02	30.042	0	0
--------------------	---------	---------	---------	---------	---------	---------	---------	-------	--------	---	---

Note: Use HClO₄ for quartz dissolution, John's method

- ₁ Add 20 ml conc. HF and 2 ml HClO₄ per 5 g of quartz
- ₂ Add 5 ml Aqua Regia
- ₃ Heat at 100-125° C until quartz dissolves, add HF if needed
- ₄ Raise to 200° C and evaporate to dryness
- ₅ Add 5 ml HClO₄ and evaporate to dryness
- ₆ Add 8 to 10 ml conc. HNO₃, swirl, and evaporate to dryness
- ₈ Take vessels off hotplate, cool.

Step 2_Splitting for Al determination

Chemist:

Date:

1

The samples are dissolved completely..Cool to room temp.

Column	1	2	3	4	5	6	7	8	9	10	11
CNEF ID	3531	3533	3536	3537	3914	3538	3546	3549	3550	3985	4096
Sample ID	PPP-17-103-001	PPP-17-103-003	PPP-17-103-006	PPP-17-103-007	PPP-17-103-008	PPP-17-103-009	PPP-17-105-017	PPP-17-110-020	PPP-17-401-022	blank Be only	Blank Al+ Be
Vessel ID	B1	B2	B3	B4	B5	B6	B9	B12	B27	B30	B32
100ml Flask	57.23	67.32	66.58	67.18	66.85	67.00	66.40	65.13	66.7024	32.7398	66.5635
100ml +sample+2% HNO3	158.35	168.43	167.79	168.36	167.92	168.17	167.57	166.34	167.8941	122.5332	167.6333
15ml tube, no lid	5.40	5.39	5.37	5.36	5.39	5.38	5.44	5.36	5.399		5.4771
5 ml before carrier added(Label as A)	4.9767	4.7334	4.6812	4.789	4.9632	4.6505	4.895	4.9167	4.8767		4.697
95 ml in mass flask	153.3726	163.6944	163.1052	163.5985	163.9538	163.5184	162.5802	161.5230	163.0164		162.9365
Zero Balance, then add Al carrier(Carrier add to 95ml mass)			0.4538						0.4056		2.975
Mass 95g and carrier			163.4576						163.4208		165.9033
test tube 2, no lid			5.3737						5.4117		5.3632
Take 5ml from solution with carrier added (labeled as B)			4.6274						4.7871		4.7753
leftover in flask	153.3726	163.6944	158.8595	163.5985	163.9538	163.5184	162.5802	161.4230	158.6332		161.1255
transfer back to Jar, and dry											

WS9_Be Sample Chemistry

This worksheet outlines the steps to prepare the BeO sample

Chemist:

Date:

Print this page

- ₁ Evaporate Be Sample from column in wiped digestion vessels at 125°C
- ₂ Add 2-5 m Conc HNO₃ to dry at 110oC ,
- ₃ Again,Add 2-5 m Conc HNO₃ to dry at 110oC .
- ₄ Dissolve sample in ~7 ml of 0.5 N HCl (optima grade)
- ₅ Transfer to 15 ml centrifuge tube
- ₆ Centrifuge and decant into clean centrifuge tube
- ₇ Heat centrifuge tubes in water bath at 60°C
- ₈ Precipitate Be(OH)₂ using Matheson ultimate grade ammonia gas
Gently bubble NH₃ with clean pipet tip on hose
for ca.15 bubbles, or ca. 8-12 sec until ptte forms
Optimum pH=9.2; 1N HCl may be added
- ₉ Centrifuge 15 min., decant (save and redo ₈ if pH of liquid is < 8)
- ₁₀ Wash with water, vortex, centrifuge for 10 min, and decant
- ₁₁ Record mass quartz vials, label, and place them in furnace holder

CNEF ID	3531	3533	3536	3537	3914	3538	3546	3549	3550	3985	4096
Vessel	B1	B2	B3	B4	B5	B6	B9	B12	B27	B30	B32
Sample ID	PI-17-103-0	PI-17-103-0	PI-17-103-0	PI-17-103-0	PI-17-103-0	PI-17-103-0	PI-17-105-0	PI-17-110-0	PI-17-401-0	Blank Be only	Blank Al+ Be
Mass Qtz Vial	1.1224	1.1654	1.2184	1.1589	1.0946	1.1907	1.0409	1.2011	1.1685	1.1685	1.1731
Mass Vial+Spl	1.123	1.1661	1.2189	1.1597	1.0952	1.1912	1.0414	1.2017	1.1690	1.169	1.1736
Mass Spl	0.0006	0.0007	0.0005	0.0008	0.0006	0.0005	0.0005	0.0006	0.0005	0.0005	0.0005

- ₁₂ Add 3 small drop of 5%HNO₃ with micropipet, slurry precipitate
- ₁₃ Transfer sample into quartz vial, cover with quartz lid
Put quartz vail into oven, dry at 120oC over night (a few hours),until dry.
- ₁₅ Burn the Be(OH)₂ gel on bunsen burner at least 2 mins, at blue/purpul flame.
- ₁₈ Convert to BeO
- ₁₉ Determine mass of vial + sample , record on the sheet.

BeO : Nb = 1:1.5 LLNL , BeO: Nb= 1:3 PRIME lab

Appendix C. Field Photos



Figure C.1. Composite photos of Section D8



Figure C.2. Cobble Sample PPI-17-103-003 in place



Figure C.3. Cobble Sample PPI-17-103-004 in place



Figure C.4. Cobble Sample PPI-17-103-005 in place

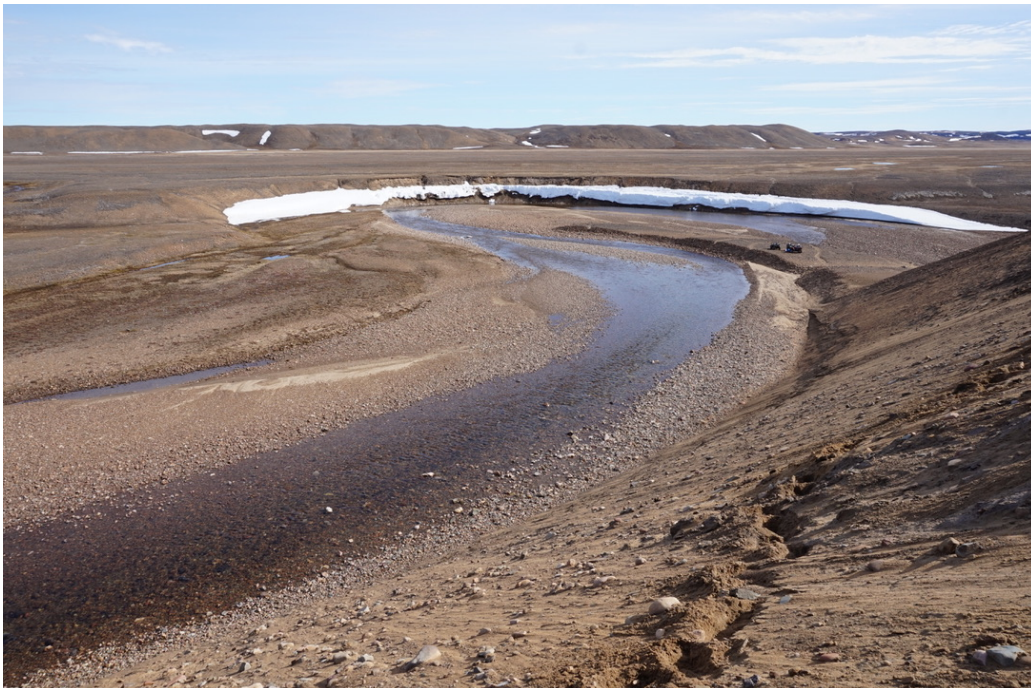


Figure C.5. Modern river incising into the bank of section D8, allowing our team to take advantage of modern erosion and access deeper sediments like the BFm



Figure C.6. Sample PPI-17-103-006, loose sand sample used for $^{26}\text{Al}/^{10}\text{Be}$ burial dating, and could be used in future for ^{14}C dating



Figure C.7. Cobble sample PPI-17-103-007 in place



Figure C.8. Cobble sample PPI-17-103-008 (left) and cobble sample PPI-17-103-009 (lower right) in place



Figure C.9. Cobble sample PPI-17-103-010 in place



Figure C.10. Expanded version of Figure 2.6, Photo D-1. Silt and peat layers within section D8, approximately 3m up section

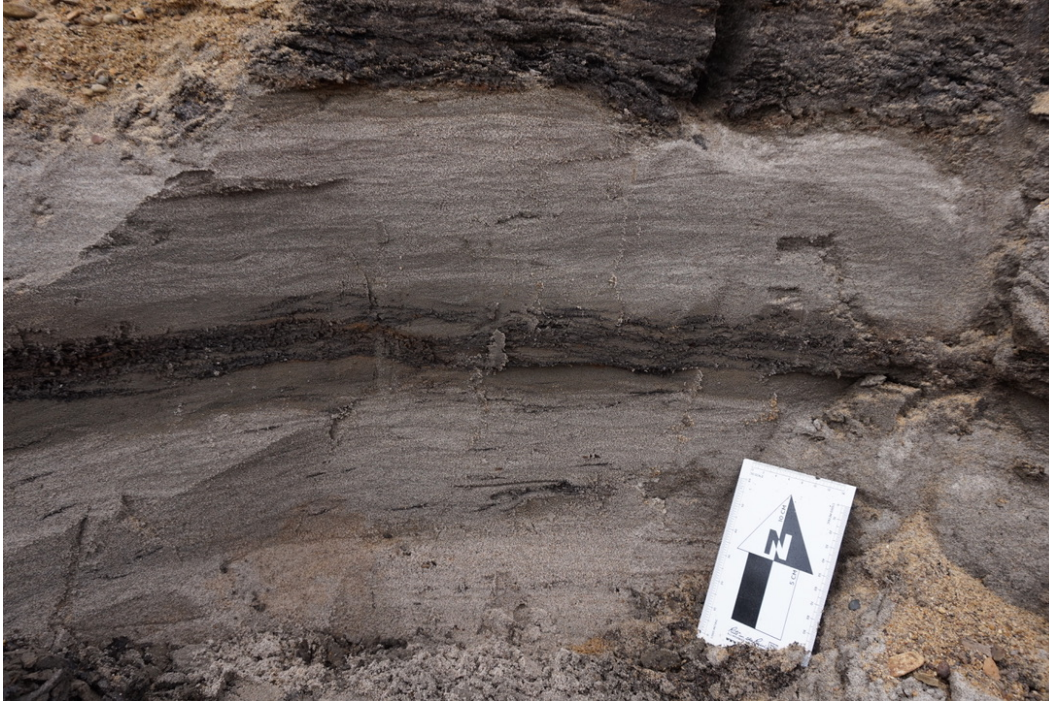


Figure C.11. Silt with minor indistinct horizontal stratification and a discernible peat layer within section D8

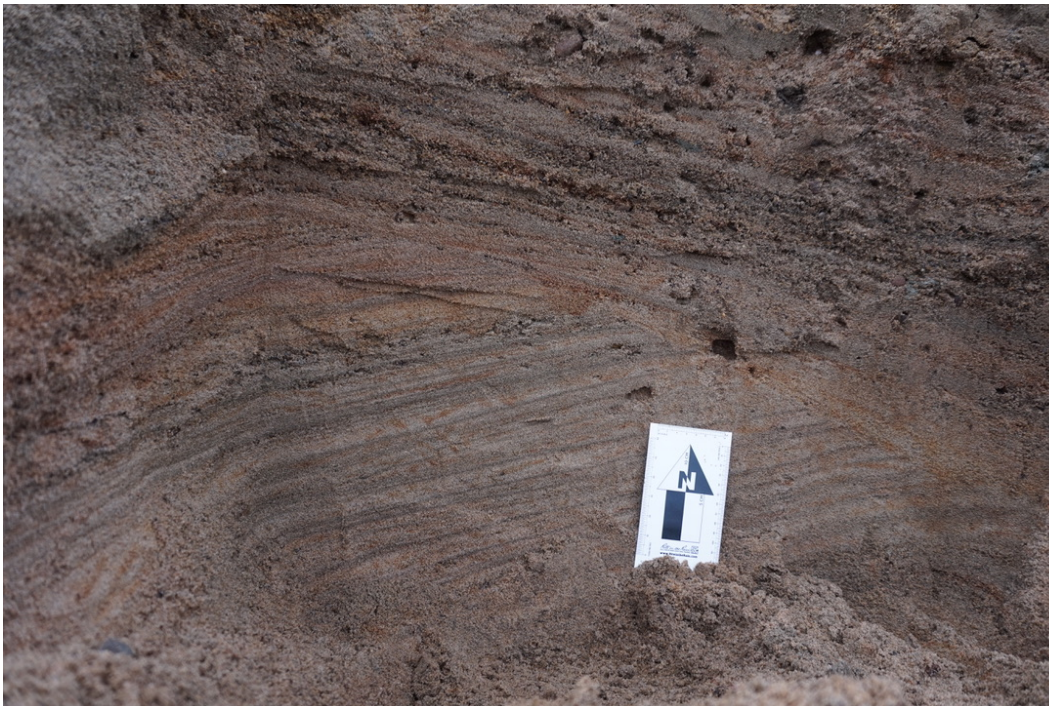


Figure C.12. Cross bedded sand facies, section D8.

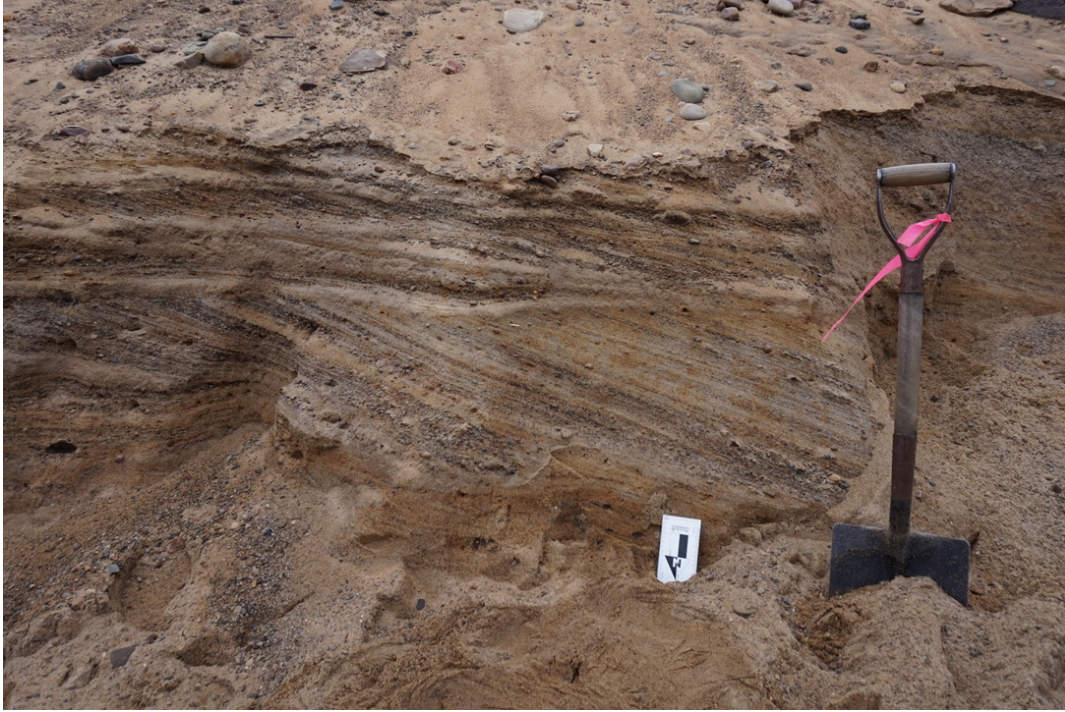


Figure C.13. Similar section to Figure 2.6 Photo D-4. Large scale cross bedded sand facies, section D8

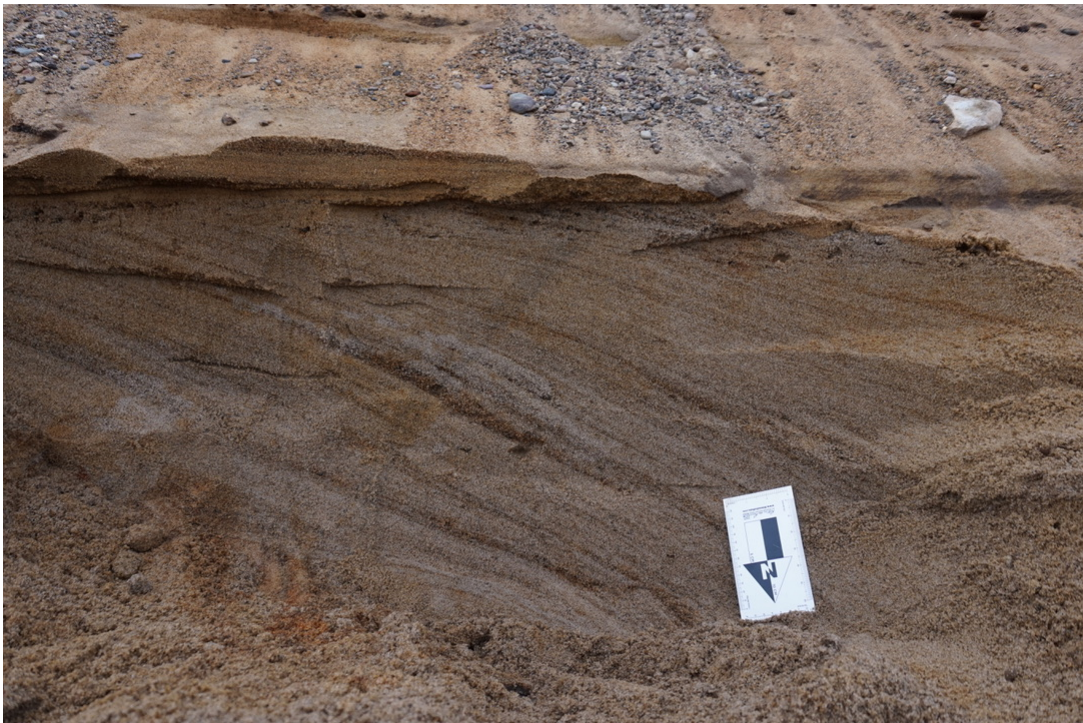


Figure C.14. Expanded photo of Figure 2.6 Photo D-5. Cross bedded sands, becoming more planar and rounded at the top.



Figure C.15. Expanded photo of Figure 2.6 Photo D-6, approximately 18 m up section of D8. Noticeable peat lens within coarse sand beds.



Figure C.16. Cobbles sampled from 18 m up section of D8 (Figure 2.6 Photo D-6). Cobble was ultimately too small for analyses.

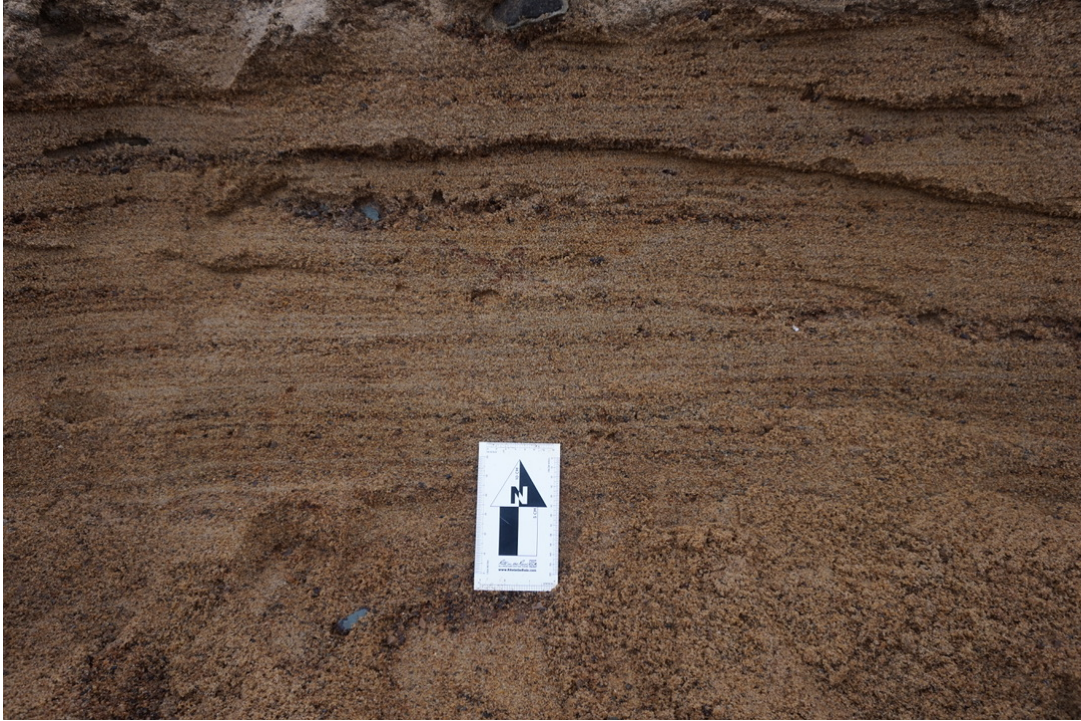


Figure C.17. Expanded photo of Figure 2.6 Photo D-3. Continuous planar bedding with coarse sandy facies, some minor lens of peat

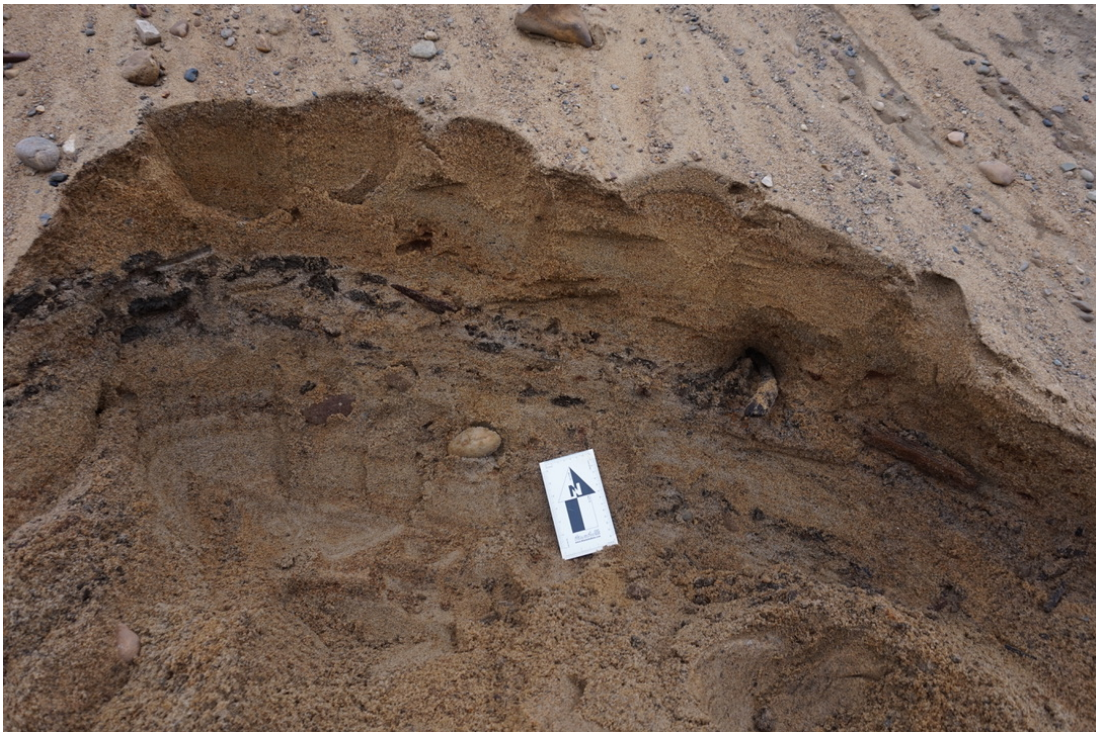


Figure C.18. Peat and fine woody detritus layer within section D8



Figure C.19. Expanded photo Figure 2.6 Photo S-3. Planar facies within bedding, section S1, approximately 11 m up section.



Figure C.20. Composite photos of section S1, a newly discovered section on Prince Patrick Island



Figure C.21. Section S1 at a distance, showing the modern stream incising into the section



Figure C.22. Large log sticking out of sediment approximately half-way up section S1



Figure C.23. Expanded photo Figure 2.6 Photo S-4. Large log sample within section S1, above planar bedding facies.

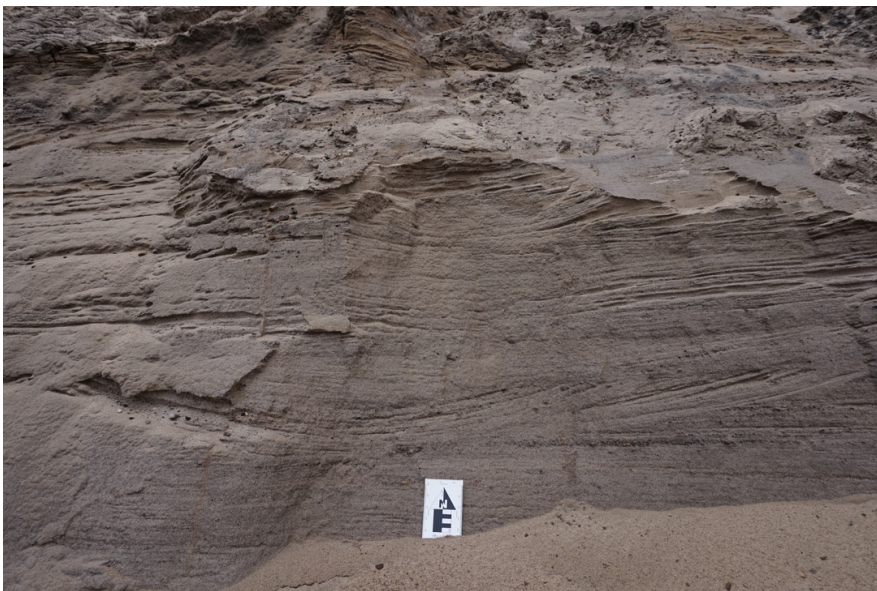
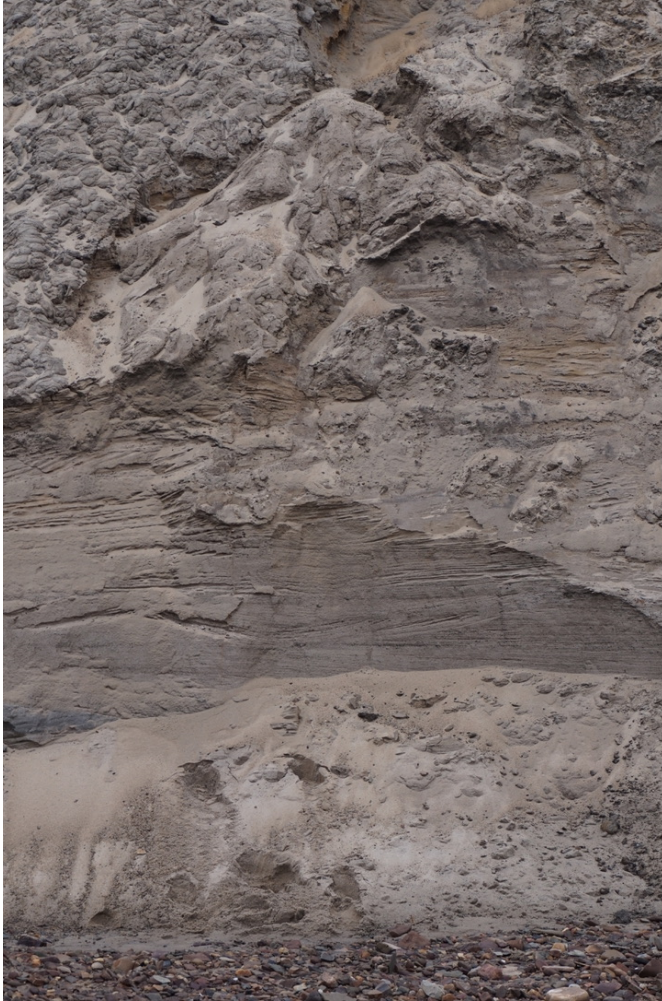


Figure C.24. Expanded photo Figure 2.6 Photo S-1. Trough cross bedding observed at base of section S1, 2 m from base of section.



Figure C.25. Expanded photo Figure 2.6 Photo S-3. Woody detritus layer sticking out of section S1 (left) and close up shot of these woody detritus layers (right).



Figure C.26. Woody detritus layer, section S1



Figure C.27. Expanded photo of Figure 2.6 Photo S-2. Coarse cross bedding sandy facies



Figure C.28. Expanded photo Figure 2.6 6B. Approximately 16 m up section, sand distinct red colour, interesting white features vertically cutting bedding



Figure C.29. Large log sample discovered at section S1



Figure C.30. Preserved tree rings within a large tree sample, likely Pliocene age



Figure C.31. Trough cross bedding facies within section S1 and erosional boundary between the bottom of the trough and the parallel bedding below



Figure C.32. Peat layer within section S1. Similar facies to Figure 2.6 Photo S-5.



Figure C.33. Expanded photo of Figure 2.6 Photo 5B. Large peat layer and silty finely bedded layer with minor ripples, section S1, approximately 14 m up section.



Figure C.34. Fine grained silty rippled bedding, section S1